Growth and complete characterizations of artificial ferroics structures based on FE and AFE materials : performances comparison in terms of CME coupling and permeability tunability

Liuyang Han

Université Polytechnique HAUTS-DE-FRANCE

Thèse de doctorat

Pour obtenir le grade de Docteur de

l'UNIVERSITÉ POLYTECHNIQUE HAUTS-DE-FRANCE

Electronique, spécialité Electronique, microélectronique, nanoélectronique et micro-ondes

Présentée et soutenue par M^me^ Liuyang HAN

Le 04/11/2019, à Valenciennes

Ecole doctorale :
Sciences Pour l'Ingénieur (ED SPI 072)

Equipe de recherche, Laboratoire :
Institut d'Electronique de Microélectronique et de Nanotechnologie - Département Opto-Acousto-Electronique (IEMN DOAE – UMR 8520)

Titre

Growth and complete characterizations of artificial ferroics structures based on FE and AFE materials: Performances comparison in terms of CME coupling and permeability tunability.

Croissance et caractérisations complètes de structures ferroics artificielles à base de matériaux Ferroélectrique et Anti ferroélectrique : comparaison des performances en termes de coefficient de couplage magnétoélectrique et de l'accordabilité de la perméabilité.

JURY

Rapporteurs
- M. Pascal AUBERT, Professeur, Univ. Orsay, Laboratoire C2N, Président de la soutenance
- M. Gilles POULLAIN, Professeur, Univ. Caen, Laboratoire CRISMAT – ENSICAEN

Examinateurs
- Mme Nathalie LEMEE, Maître de conférences-HDR, Laboratoire LPMC, Univ. de Picardie Jules Verne
- M. Tuami LASRI, Professeur, IEMN, Univ. Lille
- M. Freddy PONCHEL, Maître de conférences, IEMN- DOAE, UPHF, Co-encadrant
- M. Denis REMIENS, Professeur, IEMN- DOAE, UPHF, Directeur de thèse

Membres invités

- Wang Genshui, Professeur, Chinese Academy of Sciences (CAS), SICCAS, Shanghai.

Abstract

The magnetoelectric (ME) coupling effect, a coexistence of electrical polarization and magnetization in multiferroic materials, has been widely investigated, both from a fundamental science perspective and an application point of view. Many researchers have devoted their efforts to realize electric field (*E*) control of magnetism, instead of a magnetic field (*H*), i.e., converse magnetoelectric (CME) coupling effect. The CME effect can be realized in ferromagnetic (FM)/ferroelectric (FE) composites with an elastic strain mediation, which enables the development of novel multiferroic devices such as information storage, microwave tuning, and multi-function electronic devices.

FE materials have been intensively used in multiferroic composites to obtain a significant CME coupling effect. The FM/FE composites have achieved significant advancements because of the considerable *E*-induced strain in FE phases. The antiferroelectric (AFE) materials also undergo large deformation under the application of *E*, and large *E*-induced strain is generated. However, very few works have reported the CME coupling effect in AFE-based multiferroic composites.

In our work, a series of ME heterostructures were investigated for the fundamental understanding of AFE-based multiferroic heterostructures and the differences in the performances of AFE- and FE-based multiferroic heterostructures. The AFE ceramic and FE ceramic, (Pb, La)(Zr, Sn, Ti)O_3 (PLZST) and Pb(Mg, Nb)O_3-Pb(Zr, Ti)O_3 (PMN-PZT), were prepared as substrates to deposit FM films. Then the NiMnGa (NMG) alloys, the ferrite $Y_3Fe_5O_{12}$ (YIG) film, and uniaxial $[(TbCo_2)/(FeCo)]_{20}$ (TCFC) films were used to couple with AFE and FE materials.

The work first included a study of the strain-mediated CME coupling manipulation in NMG/PLZST/NMG heterostructure. The NMG/AFE heterostructures have been reported several times, but the E control of magnetization has never been reached. Here,

the CME coupling effect in AFE-based heterostructure has been first revealed. The magnetization of NMG film changes rapidly at the switching fields of PLZST. At 0 Oe, the magnetization change of NMG film reaches the maximum (15%).

Secondly, the ferrite YIG films deposited on PLZST and PMN-PZT ceramic substrates were studied. The CME coupling effect in YIG/PLZST and YIG/PMN-PZT was carried out, and the differences of CME performance in AFE- and FE-based ME heterostructure were revealed. The considerable *E*-induced strain in AFE substrate leads to maximum in-plane CME coefficient (α_{CME} =11.6 × 10^{-8} s/m) at 0 Oe and a maximum of in-plane relative magnetic susceptibility change ($\Delta\chi/\chi_0$ =33%) with a low magnetic field of 10 Oe in YIG/Pt/PLZST/Pt heterostructure. The maximum of in-plane α_{CME} (18.15 × 10^{-8} s/m) is observed when H = 25 Oe. The part of work demonstrated the electric-field induced strain plays a crucial role in the CME coupling effect. The different strain evolutions of substrates favors the difference in the CME coupling effect of YIG/AFE and YIG/FE.

Thirdly, we investigated the CME coupling effect of uniaxial TCFC films on PLZST and PMN-PZT substrates along different axes. A significant manipulation by *E* can be realized along the hard axis of TCFC film, and a reverse transition of *M*-*E* curves occurs. In TCFC/PLZST, the maximum of α_{CME} is at 500 Oe with a value of 12.7×10^{-8} s/m. In TCFC/PMN-PZT, the maximum of α_{CME} reaches 136.6 ×10^{-8} s/m with a bias H = 300 Oe. Along the easy axis and out-of-plane direction, the CME coupling effect has also been discussed.

Finally, the YIG/AFE and YIG/FE heterostructures have been prepared in the full thin-film form to explore the CME coupling effect. The results indicate that a FM phase with a strong magnetic response along OOP direction is needed for Magnetic Force Measurement (MFM) to evaluate the ME performance of these structures.

Keywords: ferroelectric, antiferroelectric, ferromagnetic, magnetoelectric composites, converse magnetoelectric effect, strain, magnetic anisotropy

Résumé

Le couplage magnéto-électrique (ME) a été largement étudié, tant du point de vue fondamentale que du point de vue expérimentale. Ce phénomène se manifeste dans certains matériaux multiferroïques où coexistent à la fois une polarisation électrique et une aimantation spontanée que rend possible le contrôle de la polarisation électrique à partir d'un champ magnétique extérieur (couplage ME direct ou DME); le contrôle de l'aimantation de la structure à partir d'un champ électrique (couplage ME inverse ou CME).

Le travail présenté dans ce mémoire concerne essentiellement les multiferroïques artificiels. Ces structures sont obtenues, le plus souvent, grâce à l'association d'un matériau ferroélectriques (FE) et un matériau ferromagnétique (FM). La déformation du matériau FE contraint le matériau FM à se déformer ce qui engendre une modification de son aimantation ; un coefficient CME est alors observé. Cette déformation peut également être obtenue en utilisant un matériaux anti-ferroélectriques (AFE). Cependant, très peu de travaux ont été publiés sur le sujet. Ce constat nous a conduit à envisager l'étude de l'effet du couplage CME dans les composites multiferroïques à base d'AFE. Une part du travail décrit dans cette thèse consiste ainsi à comparer les performances obtenues dans les hétérostructures FM/FE et les hétérostructures FM/AFE.

Les substrats AFE et FE utilisés dans ces hétérostructures sont respectivement les (Pb, La)(Zr, Sn, Ti)O_3 (PLZST) et les Pb(Mg, Nb)O_3-Pb(Zr, Ti)O_3 (PMN-PZT) céramiques. Les matériaux magnétiques utilisés sont quant à eux déposés par pulvérisation cathodique sur les substrats précités. Il s'agit de l'alliage NiMnGa (NMG), de la ferrite $Y_3Fe_5O_{12}$ (YIG) et du $[(TbCo_2)/(FeCo)]_{20}$ (TCFC).

En premier lieu, une étude de la manipulation de l'aimantation dans l'hétérostructure NMG/PLZST/NMG a été réalisée. Au voisinage de la transition AFE-FE du PLZT un changement abrupt de l'aimantation du film de NMG a été observé. Dans le cas présent, elle atteint un maximum d'environ 15% lorsque le champ magnétique est absent (0 Oe).

Nous nous sommes ensuite consacrés à l'étude comparative des hétérostructures FM/AFE et FM/FE.

Premièrement, le matériau ferromagnétique est le grenat de fer et d'yttrium (YIG). Des couches minces de YIG ont ainsi été déposées sur des substrats céramiques Pt/PLZST/Pt et Pt/PMN-PZT/Pt. Dans cette partie, nous nous sommes principalement focalisés sur l'aimantation en fonction du champ électrique appliqué, le coefficient CME (α_{CME}), et la susceptibilité magnétique relative ($\Delta\chi/\chi_0$). Dans le cas de l'hétérostructure YIG/Pt/PLZST/Pt (FM/AFE), le coefficient CME maximum (α_{CME} =11.6 × 10^{-8} s/m) est obtenu pour un champ magnétique nul alors que la valeur maximale de la susceptibilité magnétique relative ($\Delta\chi/\chi_0$ =33%) est observée pour un champ magnétique de 10 Oe. Concernant l'hétérostructure YIG/Pt/PMN-PZT/Pt (FM/FE), les résultats obtenus sont les suivants : α_{CME} =18.15 × 10^{-8} s/m sous un champ magnétique de 25 Oe, $\Delta\chi/\chi_0$ =65% sous un champ de 20 Oe.

Les propriétés ferromagnétiques du matériau TCFC fond de lui un candidat de choix pour les applications mémoires où de fortes variations de l'aimantation sont attendues. Dans le but de poursuivre notre progression dans l'analyse du couplage CME, les structures réalisées sont les suivantes : TCFC/PLZST/Au et TCFC/PMN-PZT/Au. Il est à noter que lorsque l'aimantation du TCFC est mesurée selon l'axe difficile, nous constatons une inversion de la courbes M-E : les minimas deviennent des maximas et inversement. Le coefficient CME peut atteindre une valeur significative de 136.6 ×10^{-8} s/m sous 300 Oe.

La dernière partie de ce travail est une tentative d'intégration de ces composants ME en technologie silicium. Deux hétérostructures (YIG/PZT et YIG/PZ) ont été synthétisés.

Mots clés: ferroélectricité, anti-ferroélectricité, ferromagnétisme, multiferroïques extrinsèques, couplage magnéto-électrique inverse, déformation, anisotropie magnétique

Acknowledgements

At the end of my work, I'd like to take this opportunity and present my gratitude to a number of people in my life. It is their trust and support that made the presented work possible.

First and foremost I would like to express my sincere appreciation to Prof. Pascal AUBERT and Prof. Gilles POULLAIN. Thanks for their patient and careful review, and their valuable comments are very important. I would also thank Madame Nathalie LEMEE for her helpful suggestion to improve our work. Her experiences in material fabrication has offered us many impressive thinking.

Then I would like to express my heartfelt gratitude to my supervisor Prof. Denis Rémiens who gave this opportunity to be part of his research group. He spent a lot of time discussing the experiment results with me, helping me to find solutions for kinds of problems. I am really grateful for his valuable time and efforts on the discussion and comments of my thesis. At mean time, he always gives me kind help in my daily life of France.

Special thanks to Prof. Freddy Ponchel who gave me lots of instructions and ideas of my work. I really enjoy the time working with him for his creative thinking in research. I cannot fulfill my thesis without the help of Freddy. I will always be benefit from the impressive discussions we have ever had.

I would also like to thank my colleagues from MAMINA group of IEMN-DOAE with whom I have worked closely over the years for providing me a fantastic experimental conditions and research environment. I would like to thank everyone in this warm big family for your memorable accompanies and firm support. I'd also like to especially thank Dr. Ahmad R. Hamieh for his support and help on my research and life in Valenciennes.

Furthermore, I am grateful to Prof. Tuami Lasri of IEMN for his invaluable inputs to my work. He gave me many important comments to my work, which has highly

improved the quality of my job. The working time with Tuami are always enjoyable. I would also like to thank Prof. Nicolas Tiercelin for the close and engaging collaboration. Prof. Nicolas Tiercelin has taught me a lot in magnetic materials and magnetic measurements. In addition, I would like to thank Yannick Dusch, Adrien Le Goff and Aurélien Mazzamurro for their kindly help and guidance in magnetic materials.

I am grateful to Prof. Genshui Wang from the Shanghai Institute of Ceramics for the valuable instructions and important support on my thesis –without his contributions this research would not have been impossible. I would like to thank colleagues from Key Laboratory of Inorganic Functional Materials and Devices of SICCAS for instructions of ceramic preparation and characterization. Their impressive knowledge of ferroelectric and antiferroelectric ceramics contributed greatly to my work.

Finally, I would like to extend my gratitude to all my friends here in the France who have made my stay here so enjoyable and memorable, I would above all like to express my deepest thanks to my wonderful family for their supporting and understanding in my PhD study period. I would not be able to achieve what I have now without their supports.

Table of Contents

List of Tables

List of Figures

1 Introduction

1.1 Motivation

Multiferroic materials, with two or more ferroic (ferroelectric, ferro/ferrimagnetic, ferroelastic) phases,[1–3] have offered greater potential and opportunity for developing novel multifunctional devices. Notably, the use of an electric field (*E*) to control the magnetic properties in multiferroic materials, known as converse magnetoelectric effect (CME),[4] has drawn intensive interest due to their essential potential in future applications such as memory devices, sensors, phase shifters, transducers, filters, oscillators, etc. [5–10]

Since single-phase magnetoelectric (ME) materials (or intrinsic multiferroic compounds, such as $BiFeO_3$ and $BiMnO_3$) are rare, and their ME effect is weak and usually far below room temperature,[11,12] most researchers have focused on ME composites to achieve strong ME coupling effect.[13–15]

The ME coupling effect in composites or heterostructures can be exploited by the strain transferring between the ferroelectric (FE) phases and ferromagnetic (FM) phases. Much advancement has recently been achieved in FM/FE composites, such as $CoFe_2O_4/BaTiO_3$, $Ni_{0.8}Zn_{0.2}Fe_2O_4/Pb(Zr, Ti)O_3$, Terfenol-D/$Pb(Mg, Nb)O_3$-$PbTiO_3$, FeBSiC/PVDF.[16–19] An application of the external electric field can lead to large magnetization and susceptibility changes in these systems. Nevertheless, investigations for a better understanding of fundamental physics and engineering potential of these materials and structures are still on the way.

Previous researchers have studied a variety of ME composites.[7,20–22] The main interest has been focused on FM/FE heterostructures and in particular the tuning of the magnetic response through the electric-field-induced strain of the FE layer applied to the FM layer. As antiferroelectric (AFE) materials enjoy a large strain during the electric-field induced AFE-FE transition, and display zero polarization and strain in a relaxed state,[23,24] there is a potential benefit for their use. Thus the advantages of large *E*-induced phase transition strain and zero remnant state in AFE materials,[25] make that AFE-based ME composites are also interesting. However, the reported works

of electric-field control of magnetism in AFE-based ME composites are scarce when compared to the work on FM/FE composites.[26,27] Thus, comprehensive research of *E*-field controlled magnetism in AFE-based ME heterostructures is necessary to understand the fundamental of ME coupling effect in FM/AFE heterostructures. At the same time, to reveal the differences of ME coupling effect in FM/AFE and FM/FE heterostructures, the comparison of *E*-field controlled magnetism in AFE- and FE-based ME heterostructures is also important.

In past decades, many different ferromagnetic or ferrimagnetic materials are used as magnetic phases to develop ME composites when targeting different applications, including oxides such as spinel ferrites, hexagonal ferrites, and lanthanum manganites, 3d-transition metals Fe, Co, and Ni, alloys such as permendur, Terfenol-D, Galfenol.[9,28–35] In strain-mediated CME heterostructures, a strong coupling between elastic and magnetic domains is required for the magnetic component.[36] The ferromagnetic materials, such as Ni-Mn-Ga (NMG) alloys and Tb, Co, Fe metals, have attracted much attention as they combine both magnetic and elastic ordering and present high magnetostriction coefficient.[35,37–39] These properties make it possible to easily manipulate their ferroelastic domains by applying a magnetic field or mechanical stress.[40] These characteristics provide opportunities to induce a substantial magnetization change by external mechanical stimulus and reach a high ME coupling coefficient, which is suitable for strain-mediated CME coupling. Ferrite yttrium iron garnet (YIG) is also considered to be a good choice as the ferrimagnetic material to develop ME composites when targeting tunable multiferroic microwave devices thanks to its outstanding advantages including small magnetocrystalline anisotropy, narrow ferromagnetic resonance linewidth, high resistivity, and low microwave losses.

Thus three magnetic materials (ferrimagnetic oxide YIG film, the ferromagnetic NMG alloys and $TbCo_2$/FeCo multilayers) are used to couple with FE and AFE materials and to compare the performance of *E*-field controlled magnetism in AFE- and FE-based ME composites. In this thesis, we focused on the CME coupling effect in both FE- and AFE-based ME composites. In order to observe the distinct coupling effect, the composites' laminated structure is designed to be FM films deposited on FE or AFE ceramic substrates. The voltage-controlled magnetization switching and magnetic susceptibility variations are studied in different heterostructures.

1.2 Scope of Work

The thesis begins with a background review in Chapter 2. The basic theory and general concepts of multiferroic and ME materials would be introduced. The research progress on AFE-based multiferroic material fabrication, mechanism studies, and practical applications are given in the past few decades, as well as the current problems needed to be solved and identified.

In Chapter 3, the main experimental techniques would be given. It includes ceramic and thin film preparation, structural analysis, electrical and magnetic characterization.

Chapter 4 introduces the FE and AFE ceramic substrates prepared for CME coupling. The microstructure and electric properties of ceramic substrates are illustrated.

Chapter 5 gives the first work of the *E*-field controlled magnetization variations in an AFE-based heterostructure. The NMG/AFE/NMG heterostructure is fabricated, and the CME coupling effect has been demonstrated.

Chapter 6 and 7 present the CME coupling effect of FM films on FE ceramic substrates and AFE ceramic substrates, respectively. The multiferroic heterostructures of YIG/PLZST, YIG/PMN-PZT, $[TbCo_2/FeCo]_{20}$/PLZST and $[TbCo_2/FeCo]_{20}$/PMN-PZT are demonstrated in these two chapters. The *E*-field controlled magnetization switching and *E*-field tuning of the susceptibility of YIG film on PLZST and PMN-PZT ceramics are revealed, and the strain-induced anisotropy transformation of YIG film is also demonstrated. The CME coupling effect along different axes is presented in $[TbCo_2/FeCo]_{20}$ films on PLZST and PMN-PZT ceramics.

In Chapter 8, the YIG/AFE and YIG/FE composites in thin-film form are fabricated, and the magnetic response of YIG films are tried to characterized.

A summary of the thesis and several propositions of future work are provided in Chapter 9.

2 Backgrounds and Literature Review

The concept of "ferroic" is referred to the properties of ferroelectricity, ferromagnetism, and ferroelasticity in a crystal, as Aizu concluded in 1970.[41] The most distinct feature of "ferroic" is the existence of domain. The order parameters (dipole moment, magnetic moment, etc.) of atoms or ions in adjacent positions of ferroic materials are arranged in the same direction in the local area due to interaction, thereby forming an ordered region, named "domain". The domains allow the order parameter of ferroic materials to change with the presence of the external field, and leads to hysteresis loops. Later, it was found that ferrotoroidicity also belongs to the family of "ferroic". [42] The spontaneous polarized or magnetized domains in ferroic materials allow the order parameter to change with the application of the external fields, and ferroic materials would present hysteresis loops and anomalies at the phase transition.

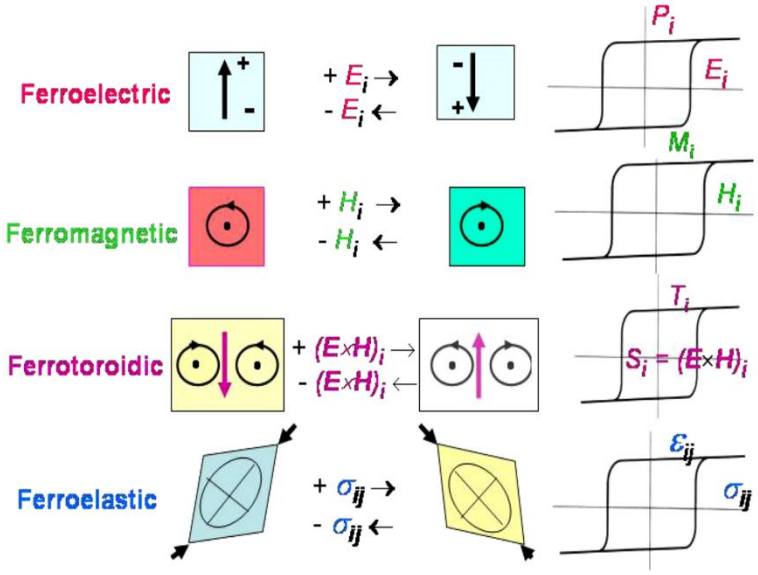

Figure 2.1 Schematic of the four primary ferroics.[42]

2.1 Theoretical Background

2.1.1 Ferroelectrics and Antiferroelectrics

The study of ferroelectric materials is generally believed to have begun in 1921, when J. Valasek firstly observed the dielectric anomalies in Rochelle salt. [43] Then,

ferroelectric materials develop quickly and become essential components in a broad spectrum of applications. The concept of antiferroelectricity was proposed in 1951 to describe a state where chains of ions in the crystal are spontaneously polarized, but with neighboring chains polarized in antiparallel directions.[44] Since then, various antiferroelectrics have been discovered over the past half century, and research on antiferroelectric materials has received increasing attention.

(1) Ferroelectrics

Ferroelectric materials are a family of materials who display spontaneous polarization in a specific range of temperature, and the polarization of FE materials is reversible with an application of the electric field. In FE materials, the adjacent dipoles in one domain share the same polarization orientation, and orientation of the dipoles can be aligned by an external DC electric field. For illustration, Figure 2.2 (a) shows the electric-field dependence of polarization (*P*–*E*) of FEs. When the external electric field turns to the opposite direction, new ferroelectric domains of FEs begin to nucleate and grow up, the domain wall moves, and finally, the polarization reverses. When an electric field is applied to ferroelectric materials, a strain accompanying the polarization reversal process would also be generated in ferroelectrics, as given in Fig. 2.2 (b). The electric-field dependence of strain (*S*-*E*) loop in a butterfly shape can be attributed to three effects: the converse piezoelectric effect, the switching, and movements of domain walls.

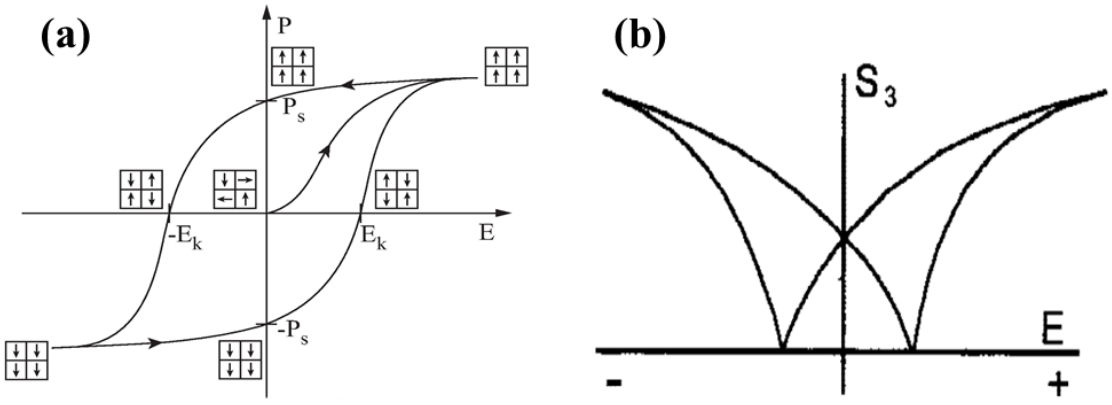

Figure 2.2 (a) Hysteresis loop, and (b) longitudinal *S*-*E* loop of FEs. [45]

The hysteresis loop of FEs indicates that the spontaneous polarization is reversible under an application of the electric field. This feature is essential for the applications of

data storage, especially non-volatile memory devices. In addition to ferroelectricity, ferroelectric materials also present dielectric, piezoelectric, pyroelectric properties, which shows great potential in the applications of semiconductor and applied physics.

(2) Antiferroelectrics

Although the precise definition of antiferroelectrics is still controversial, it is generally believed that the adjacent dipoles are aligned in opposite orientation in AFE materials. In this case, if a sufficiently high DC electric field is applied, the polarization orientation of dipoles would be aligned into one direction so as to realize an FE state. This is called the electric-field-induced phase transition.

When an electric-field induced AFE-FE phase transition happened, the corresponding structure phase transition with an apparent expansion of volume would generate big cell strain, as given in Fig. 2.3 (b). Unlike FE materials, the strain or displacement induced in AFE materials originates from the *E*-induced AFE–FE phase transition because the unit cell of the FE phase is larger than that of the AFE phase. Hence it is possible to keep the high strain level even when the materials are in thin-film form.

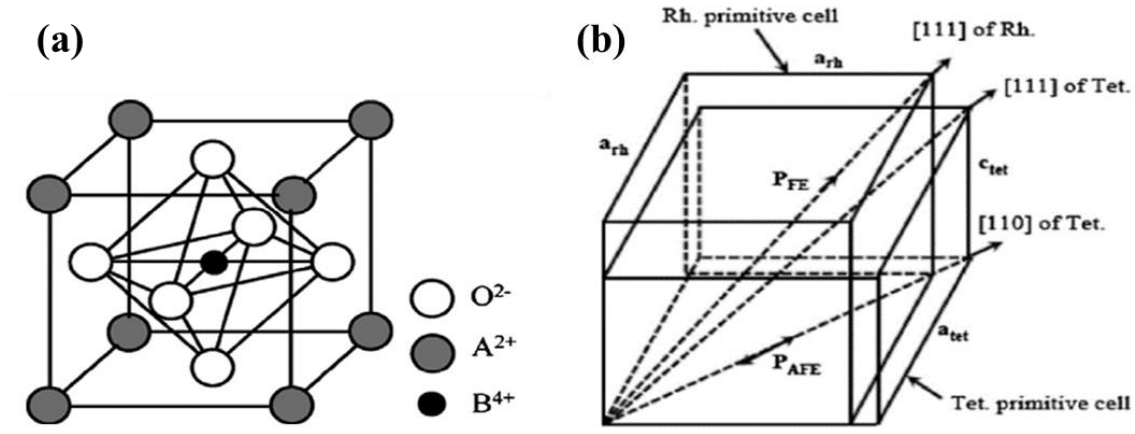

Figure 2.3 (a) A typical ABO_3 united-cell structure, and (b) Primitive cell schematic diagram of antiferroelectric (tetragonal structure) and ferroelectric (hexagonal structure).[46]

Figure 2.4 (a) shows the double *P*–*E* hysteresis loops of AFE materials.[24] When the applied electric field is lower than the phase transition field strength (abbreviated as E_F), the AFE materials exhibit the properties of a linear dielectric. When the applied

electric field is higher than E_F, the polarization jumps suddenly to a very high level and is close to saturation. The field-induced FE phase returns to the AFE phase when the electric field is removed, or the electric field is reduced to a field-induced FE phase to a critical electric field (E_A) of the AFE phase. This reversible process, accompanied by a significant strain reduction because the unit cell shrinks exhibits a sizeable electrostrictive coefficient. Therefore, the *S*-*E* hysteresis loop of AFEs is entirely different from the *S*-*E* loop of FEs, as shown in Fig. 2.4 (b).

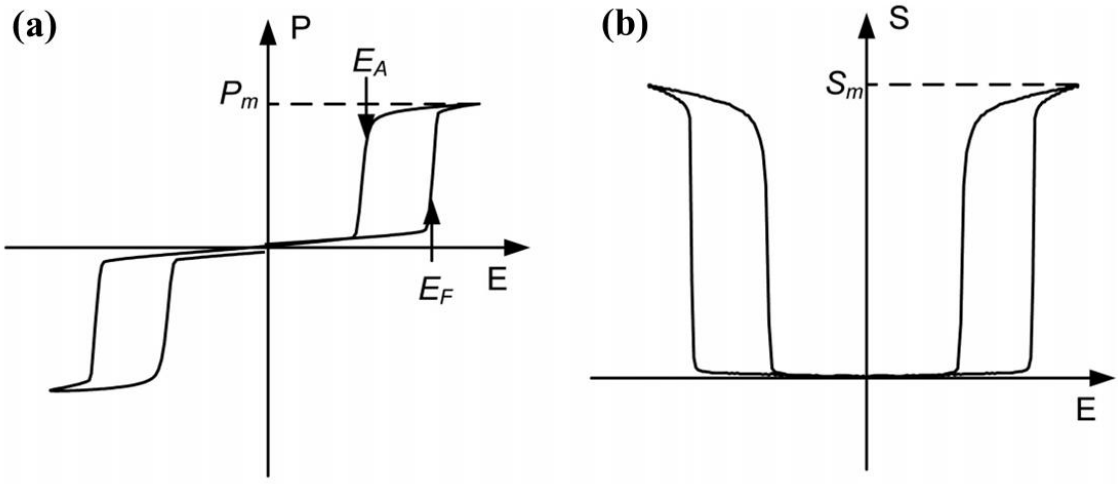

Figure 2.4 (a) Double hysteresis loop, and (b) longitudinal *S*-*E* loop of AFEs.[47]

The novel *E*-induced phase transition of AFEs has drawn tremendous interest for their engineering applications, such as high energy storage capacitors, micro-actuators, pyroelectric security sensors, cooling devices, and pulsed power generators and so on.[48–51] In recent years, some researchers turned the attention to AFE-based multiferroic composites because of their considerable electric-field induced strain.[25]

2.1.2 Magnetism and Magnetic Properties

The first deliberate use of the magnetism stems from the 11th century in forms of the magnetic compass, which has dramatically encouraged human navigation and geographic discoveries. The remarkable discovery of Hans Christian Oersted in 1821 that an electric current flowing through a wire produces a magnetic field, has opened a new page of fundamental magnetic research.[52] Since then, significant development of the electromagnets has been achieved, which made major contributions to the development of the functional materials.

(1) Magnetism

Magnetism is a quantum mechanical phenomenon originating from the fundamental properties of the atom and its electrons. There are two types of rotational motions for electrons. One is called “spin” that the electron spins around itself, another one is “orbit” that the electron moves along an orbit around the atom. The electrons orbital motion and spin themselves can create magnetic moments, respectively, and they also can be coupled, which is called spin-orbit coupling.[53] The coupling also includes orbit-orbit coupling and spin-spin coupling among electrons, which give a total atomic magnetic moment. Thus all materials experience magnetism, but in practice, not all materials can produce effects that are reasonably large.

The magnetic behavior of different materials under the influence of a magnetic field is given as

$$M = \chi H \tag{2.1}$$

where M is the magnetization, χ is the magnetic susceptibility, and H is the magnetic field strength. There are five types of magnetic materials concerning their magnetic characteristics. They are diamagnetic, paramagnetic, antiferromagnetic, ferromagnetic, and ferrimagnetic materials, as given in Fig. 2.5.

Diamagnetic, paramagnetic and antiferromagnetic materials are weak magnetic materials, while ferromagnetic and ferrimagnetic materials are of strong magnetism. Diamagnetic materials have negative and small susceptibilities ($\chi = 10^{-5}$), hence repulse magnetic fields. Paramagnetic materials exhibit positive but small susceptibilities in the range of $\chi = 10^{-5}$ - 10^{-2}. Antiferromagnetic materials magnetize weakly in the direction of an external magnetic field. In antiferromagnetic materials, the adjacent magnetic moments are aligned in opposing direction with the same magnitude, like antiferroelectrics. In ferrimagnetic materials, the adjacent magnetic moments are also aligned in opposing direction, but with different magnitudes, thus magnetic susceptibilities of ferrimagnetic materials are high. Ferromagnetic materials retain almost perfectly aligned magnetic moments even without an external magnetic field that they are the most widely utilized magnets with very high susceptibilities.

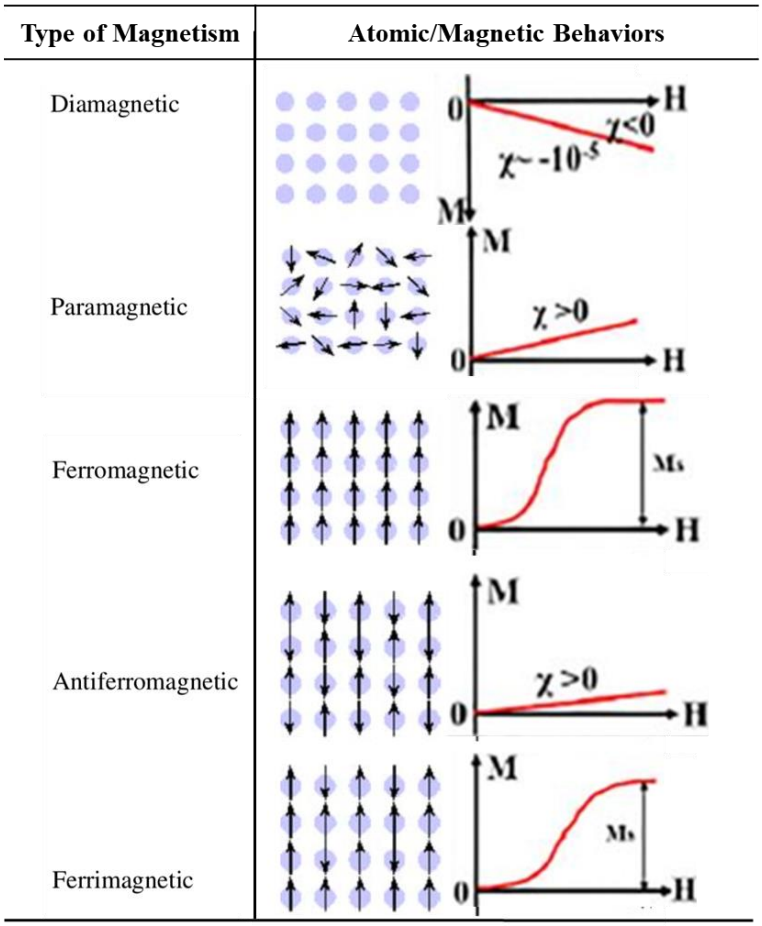

Figure 2.5 The classification of magnetic materials.

(2) Ferromagnetic and Ferrimagnetic Materials (FM Materials)

Ferromagnetic and ferrimagnetic materials present two distinct characteristics: spontaneous magnetization and magnetic domain. The strong internal interactions of ferromagnetic materials align the magnetic moments parallel to each other, which produces a spontaneous magnetization even in the absence of an external magnetic field.[54] The spontaneous magnetization orients to preferred directions because of the magnetocrystalline anisotropy. Ferromagnetic domains are small regions where all the atomic magnetic dipoles have a parallel alignment to each other.[55] The magnetization directions of different domains can be different. Likewise, ferrimagnetic materials have populations of atoms with opposing magnetic moments, as in antiferromagnetism; however, in ferrimagnetic materials, the opposing moments are unequal. Thus the spontaneous magnetization and magnetic domains remain.

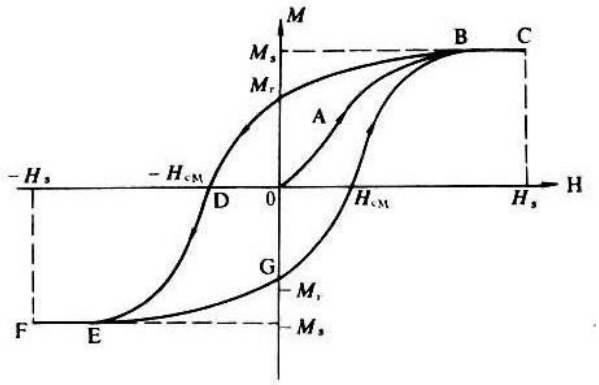

Figure 2.6 The magnetic hysteresis loop of FM materials.

With an application of the external magnetic field, the domain wall motion and domain rotation work together in ferromagnetic materials and lead to a magnetization-magnetic field (*M*-*H*) hysteresis loop, as given in Fig. 2.6. In ferromagnetic materials, all domains are randomly arranged, and the total magnetization is zero with the absence of an external magnetic field. When the external magnetic field is applied, the domain in which the spontaneous magnetization is nearest to the applied field direction starts to grow with domain wall moving. The other domains whose spontaneous magnetization is not close to the applied field direction, become smaller and smaller. Finally, all the domains align with the applied field direction; hence, the magnetization reaches saturation, as illustrated in Fig. 2.7.

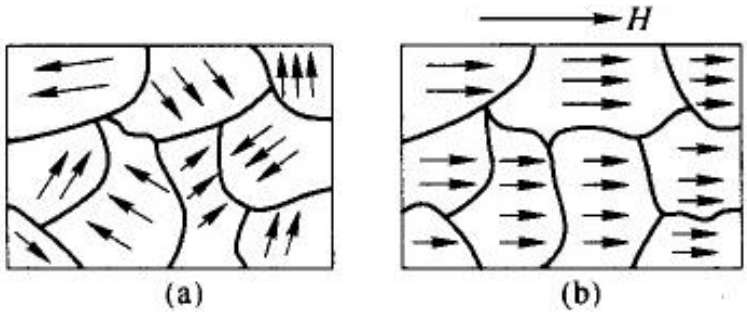

Figure 2.7 The magnetic domain of ferromagnetic materials.

These features of ferromagnetic materials provide great opportunities in a wide range of applications in modern device technologies.

2.1.3 Magnetoelectric materials

(1) Multiferroics

In the past decades, multiferroics have attracted many interests due to its significant improvement to data storage, sensors, and spintronics devices. In the definition, multiferroic materials have any two of the above ferroic orders and interactions, as shown in Fig. 2.8.

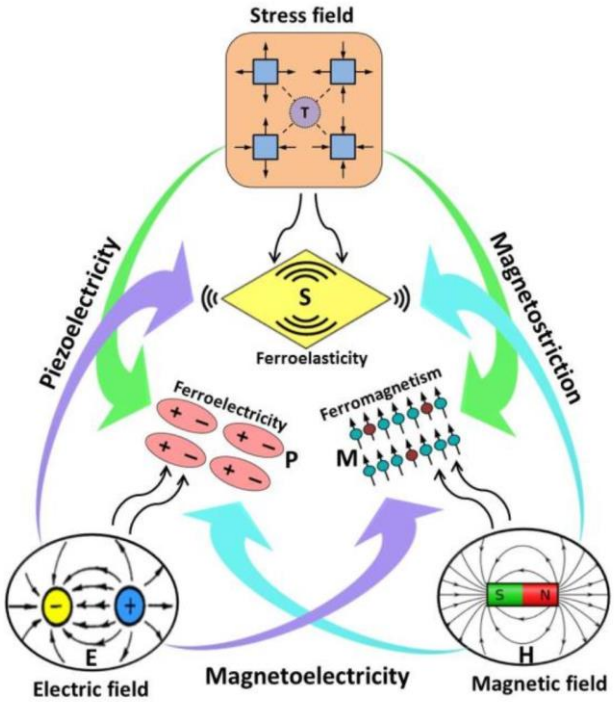

Figure 2.8 Schematic illustrating magnetic-elastic-electric couplings in multiferroic materials.[56]

Coupling between different ferroic orders has enabled the tunability of various electric and magnetic parameters—the most interesting of which is the coupling between ferroelectricity and ferromagnetism, known as the magnetoelectric (ME) coupling effect. The ME materials exhibit either induced polarization under an external magnetic field, or induced magnetization under an external electric field. The concept of the ME effect was originally proposed by P. Curie in 1894. In 1959, Dzyaloshinskii predicted the existence of single-phase ME substances that simultaneously have electric and magnetic dipole moments.

The ME response is the appearance of an electric polarization (P) upon applying a magnetic field (H) (i.e., so-called direct ME effect):

$$\Delta P = \alpha \cdot \Delta H \; or \; \Delta E = \alpha_E \cdot \Delta H \tag{2.2}$$

where E denotes electric field, and α (α_E) is the ME (ME voltage) coefficient. Thus, the electric polarization can be modified by a magnetic field, or voltage output can be produced by applying a magnetic field on the materials via the ME coupling. Sometimes, the magnetodielectric effect is used, i.e., the change in dielectric constant with the magnetic field. In addition to this direct ME effect, there is simultaneously the converse ME (CME) effect, i.e., the appearance of magnetization (M) upon applying an electric field (E),

$$\Delta M = \alpha \cdot \Delta E \tag{2.3}$$

which indicates the modulation of magnetism by an electric field. In a multiferroic material with ferroelectric and ferromagnetic orders co-existing, such strong ME effects make the multiferroic ME materials promising in applications such as multifunctional sensors, transducer, filters, oscillators, phase shifters, memory devices, and so on.

(2) Classifications of ME Materials

There are two categories of ME materials, single-phase ME materials and composites.

Single-phase ME materials exhibit ferroelectricity and ferromagnetism in one single compound. The general criteria for the appearance of ferromagnetism is exchanging interaction of electron spins, while the redistribution of charge density in the lattice for the ferroelectricity. These make it possible for the coexistence of spontaneous magnetization and polarization in one single phase ME material.[57] Single-phase ME materials are chemically homogenous compounds, and they exhibit intrinsic ME coupling by the co-existence of magnetic moments and electric dipoles simultaneously. In 1957, scientists predicted the existence of a linear ME coupling coefficient in Cr_2O_3; subsequently, the ME coupling effect was experimentally confirmed with a ME coefficient of α = 4.1 pS/m. [58,59] Since then, various single-phase ME materials ($GaFeO_3$, Ti_2O_3, $REMnO_3$, RE = Y, Ho, Er, Tm, Yb, Lu, etc.) have been gradually discovered, [4] the representative of single-phase ME materials is $BiFeO_3$ (BFO). BFO is a room-temperature single-phase multiferroic materials with the coexistence of robust ferroelectricity and antiferromagnetism (T_{FE} = 1100 K, T_N = 643K), and a weak canted magnetic moment at room temperature. It is predicted that the saturated polarization of BFO can reach 100 μC/cm^2 at room temperature.[60]

However, the ME coupling effect is restricted in BFO because of its weak ferromagnetism above room temperature.[8]

In general, the current ME coupling effect of most single-phase ME materials are still weak, which greatly hinders their applications. Therefore, the researchers turned their attention to ME composites, which consist of physically separated magnetic and electric order phases. By artificially design of ferromagnetic/ferroelectric multiphase composites, the ferroelectric phase, and ferromagnetic phase can be selected from a wide range of materials to obtain the optimized ME coupling effect, which offers a larger space to design and manipulate ME materials, and they exhibit higher ME coupling coefficient than those found in single-phase materials at room temperature. For example, it is several orders of higher magnitude than that in single-phase multiferroic materials so far available at room temperature.[61]

The concept of ME composites was first proposed in 1972,[62] then various multiferroic composites have been reported.[63–69] The phase connectivity and interfacial bonding of the FE and FM phases can greatly influence the ME coupling effect. Based on the phase connectivity of composites,[70] ME composites can be commonly prepared through three different ways: 0-3, 2-2, and 1-3 connectivity, as shown in Fig. 2.9 (a), (b) and (c). The 0-3 particle-matrix composites mainly combine ferroelectric or magnetic oxide particles into another phase matrix for sintering, thereby achieving two-phase composites. The 0-3 type is simple in preparation, and the interface between two phases is large enough for strain transfer, but the magnetic particles with good conductivity would lead to high leakage, which hinders its development. The 1-3 cylinder-matrix composites are formed by embedding magnetic fibers/rods/tubes/wires in the ferroelectric matrix. The fibers can be either randomly dispersed or periodically aligned. The 1-3 type composites can reach a large ME coupling coefficient, but the preparation process is strict, and large leakage can also be a problem. The 2-2 laminate composites are composed of alternative ferroelectric and ferromagnetic films or bulks. Such composites can be designed into different shapes, bilayer, or multilayer structures. The 2-2 laminate composites can preserve the physical characteristics of the individual phases. The preparation process of 2-2 laminates is relatively simple, and the high-resistance ferroelectric layer can effectively avoid the

influence of leakage current. These advantages of make 2-2 laminate structure to be the most promising composite structure.[56]

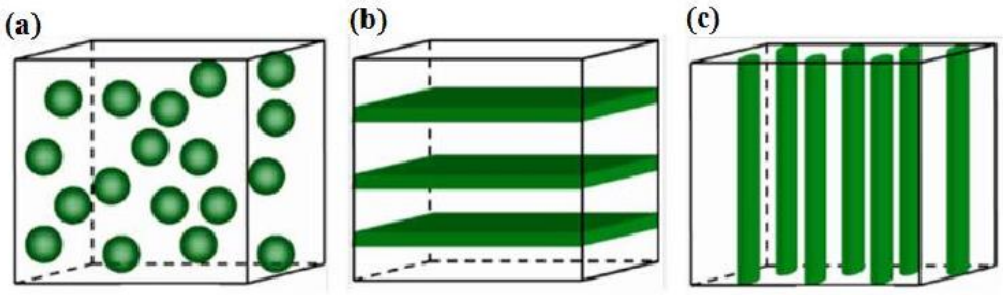

Figure 2.9 Schematic illustration of three bulk composites with the three common connectivity schemes: (a) 0–3 particulate composite, (b) 2–2 laminate composite, and (c) 1–3 fiber/rod composite.[61]

(3) The Strain Mediated ME Coupling Effect

The ME coupling effect in ME composites can be realized by three different mechanisms, i.e., charge mediated ME effect,[71–73] exchange bias mediated ME effect and strain mediated ME effect.[68,74–77] The strain mediated ME effect in composites results from the elastic coupling between the piezoelectric and magnetostrictive components.

The strain mediated mechanism is to manipulate the ferromagnetic or ferroelectric response with the electric field or magnetic field induced strain, as given in Fig. 2.10. In direct ME (DME) coupling, the applied magnetic field generates strain in the magnetic layer via the magnetostriction effect, and this strain is transferred to the piezoelectric layer resulting in an electric displacement or a dielectric polarization through the piezoelectric effect. In CME coupling, an external electric field induces strain in the ferroelectric layer due to the inverse piezoelectric effect, and the strain transferred to the magnetic layer produces a magnetization change or domain reorientation by magnetic anisotropy transformation.

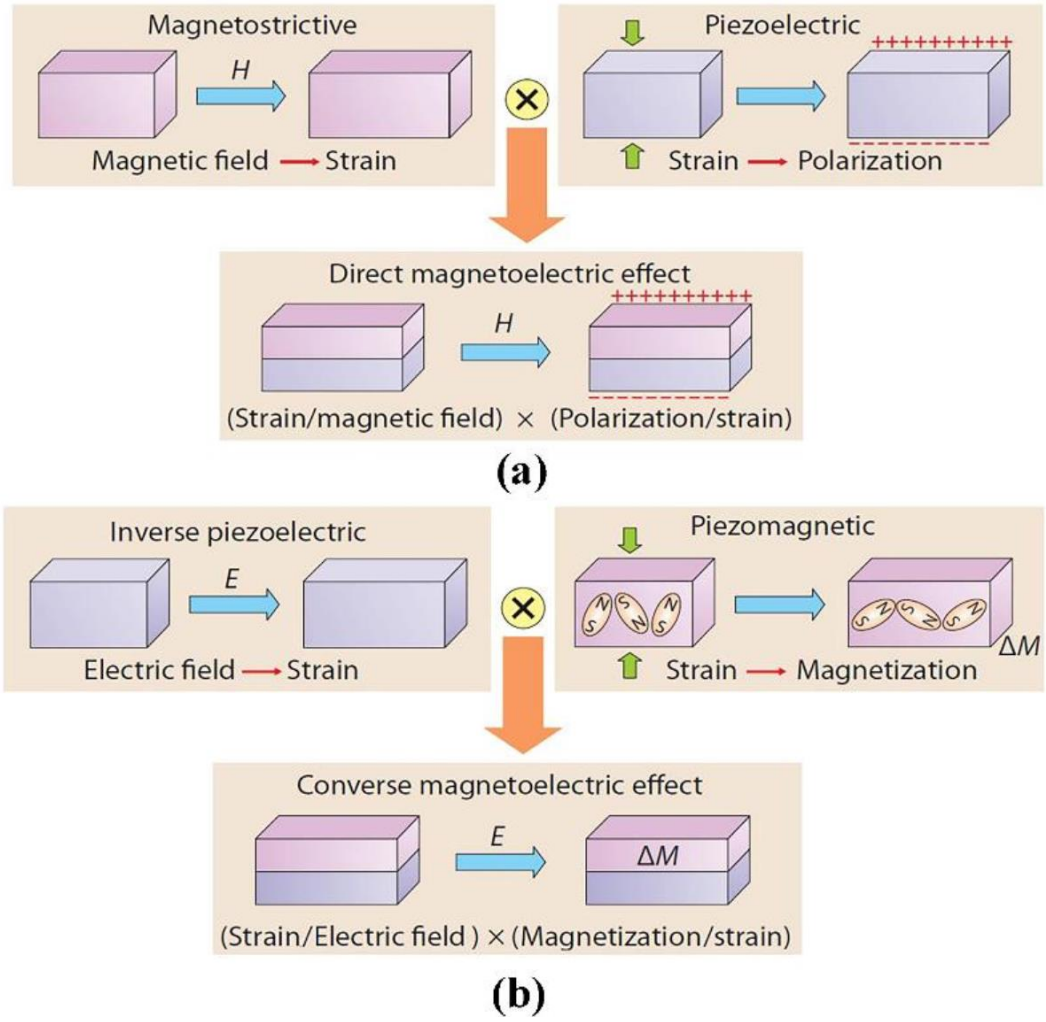

Figure 2.10 Schematic illustration of strain-mediated ME effect in a composite system consisting of a magnetic layer (purple) and ferroelectric layer (pink): (a) DME effect (b) CME effect.[78]

In a word, the strain can be transferred through the interface from one phase to another phase, thereby realizing the *H*-field control of polarization or *E*-field manipulation of magnetization. The strain mechanism is the most common and effective method to realize the ME coupling effect in the ME composites due to its simple principle and strong practicability.

In this strain-mediated ME coupling effect, the interface between FE phases and FM phases plays a crucial role in ME response.[79–82] Several researchers have demonstrated that the large thickness and low shear modulus of the interfacial bonding results in a significant drop in ME response.

(4) The Strain-Induced Magnetic Anisotropy Transformation

To reveal how the strain mediated CME coupling effect works, it is necessary to demonstrate the strain-induced magnetic anisotropy transformation in magnetic materials. The strain can induce a magnetic anisotropy in magnetic materials due to the magnetoelastic effect. For example, in polycrystalline magnetic films, there is not a preferred orientation due to the random grain arrangement. Thus the magnetocrystalline anisotropy energy is small. The effect of elastic stress on magnetization is called the inverse magnetostrictive effect. The applied elastic stress will alter the domain structure and create a new anisotropy competing with the other anisotropies. The effect of elastic stress on magnetization can be understood based on minimizing magnetoelastic energy in the magnetic system. The magnetoelastic energy (E_{me}) can be given by[52]

$$E_{me} = -\frac{3}{2}\lambda_s \sigma cos^2\theta \tag{2.4}$$

where λ_S is the saturation magnetostriction constant, σ is the external stress, and θ is the angle between the saturation magnetization (M_S) and the stress (σ).

If the magnetostriction constant λ is positive in a material, the external tensile stress ($\sigma > 0$) will lead more magnetic moments to align along the stress direction (i.e., $\theta = 0°$) to reach the minimum of magnetoelastic energy. When a magnetic field is applied along this tensile stress direction, a lower magnetic field will be required to saturate the sample, which means that tensile stress produces a preferred magnetization direction. When compressive stress is applied ($\sigma < 0$) to a magnetic material, which has a positive λ, magnetic moments tend to align perpendicular to the compressive direction (i.e., $\theta = 90°$) to reach the minimum of magnetoelastic energy.

In a word, *E* control of magnetism in multiferroic heterostructures is achieved by *E*-created magnetic anisotropy. Strain mediated ME coupling in layered ferromagnetic/ferroelectric heterostructures can provide great opportunities in realizing novel multiferroic devices.

(5) Measurements of CME

Generally, there are three ways to characterize the CME effect, i.e., the voltage induced magnetization variations, *E*-tuned ferromagnetic resonance (FMR) shift in the

resonance frequency and in situ *E*-field controlled magnetic domain change by scanning probe microscopy techniques.

According to Equation 2.3, the electrically induced ME coupling coefficient can be estimated by measuring the induced magnetization with an applied AC voltage. The CME coefficient can be determined by the slope of the linear graph of the induced magnetization versus the AC voltage amplitude.[83,84] Another commonly used CME coefficient can be deduced from the FMR shifts under an applied electric field that manifests the *E*-induced strain to be an internal magnetic field in composites. The effect is expected to be the largest when the frequency of the AC electric field/voltage matches the electro-mechanical resonance frequency of the sample.[84] The ME coupling can also be in situ characterized by scanning probe microscopy techniques, such as magnetic force microscopy (MFM), and FMR under the electric field with the use of a scanning microwave microscopy (SMM).[14,61,85]

2.2 Literature Review

Since Suchtelen first proposed the concept of the composite ME effect in 1972, the ME composites have gotten tremendous development. The appearance of the giant magnetostrictive rare-earth-iron alloy Terfenol-D has substantially simulated the upsurge of multiferroic ME composites research in the early 2000s. Since then, various multiferroic heterostructures have been intensively investigated to obtain the strong ME coupling effect.[86–92] Materials used for the ferromagnetic/ferrimagnetic phases include 3d-transition metals Fe, Co, and Ni and alloys such as ferrocobalt, Terfenol-D, Galfenol, spinel ferrites, hexagonal ferrites, and lanthanum manganites. The ferroelectric phases used in the previous studies were Pb(Zr, Ti)O_3 (PZT), $BaTiO_3$ (BTO), lead magnesium niobate-lead titanate (PMN-PT), and poly (vinylidene fluoride) (PVDF).[68,69,77,92,93] Alternatively and with great design flexibility, the significant ME coefficients are obtained, much larger than in single-phase ME materials. In particular, electric field controlled CME coupling effect has been widely studied, and devices are prepared for power-efficient voltage writing of magnetic bits, voltage tunable inductors, tunable bandpass filters, tunable phase shifters, etc.

Conventional CME composites are the combination of FM materials and FE materials, in which the magnetic properties of FM materials can be manipulated by

applying the voltage to FE materials through strain transferring. Recently, novel multiferroics composites of FM/AFE materials have attracted the researchers' attention. AFE materials, with novel properties of electric-field-induced AFE/FE phase transition, exhibit a large and sharp strain change during the phase transition for atomic rearrangements and zero polarization and strain in relaxed state. On the one hand, the significant strain of AFEs, which can reach 0.87 % in some reported AFE ceramics, make them extremely attractive for strain-mediated ME coupling.[94–96] On the other hand, the non-remnant state of AFEs results in no pre-poling process which shows excellent compatibility with various applications.[25]

To explore the physics underlying the ME effects, researchers have developed both simulation and experiment methodologies. As for the simulation, Liu *et al.* firstly performed a Monte Carlo simulation to theoretically predict ME coupling induced phase transitions in AFE–antiferromagnetic (AFE–AFM) systems in 2004, as well as a mean-field approach (MFA)-based Heisenberg model to explain the simulation results. They have revealed that weak FM and FE orders will occur below specific temperature either by the ME coupling or by applying external electrical field.[97] Sosa *et al.* have simulated the dielectric and magnetic properties of multiferroic materials in an AFE-FM system using the Monte Carlo method. It has been revealed that when the applied electric field increases, the ferromagnetic transition temperature diminishes, and the magnetic order disappears at E=30, (Fig. 2.11).[98]

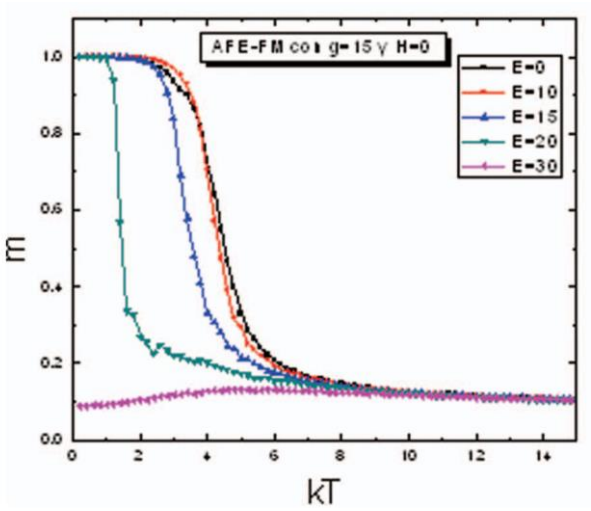

Figure 2.11 Magnetization as functions of temperature for different values of the electric (E) fields.[98]

Lepadatu *et al.* carried out an interesting model of heat-assisted multiferroic solid-state memory in an FM/AFE bilayer.[23] In this model, the strain is generated using the AFE layer by voltage-induced AFE-FE phase change, and it is transferred to the magnetic free layer by strain-mediated coupling effect. The thermally activated strain-induced magnetization switching was analyzed using a three-dimensional, temperature-dependent magnetization dynamics model, based on simultaneous evaluation of the stochastic Landau-Lifshitz-Bloch equation and heat flow equation, together with stochastic thermal fields and magnetoelastic contributions, as given in Fig. 2.12. With stress values ranging from 80 to 180 MPa and maximum temperatures normalized to the Curie temperature ranging from 0.65 to 0.99, the thermally activated strain-induced magnetization switching can be realized.

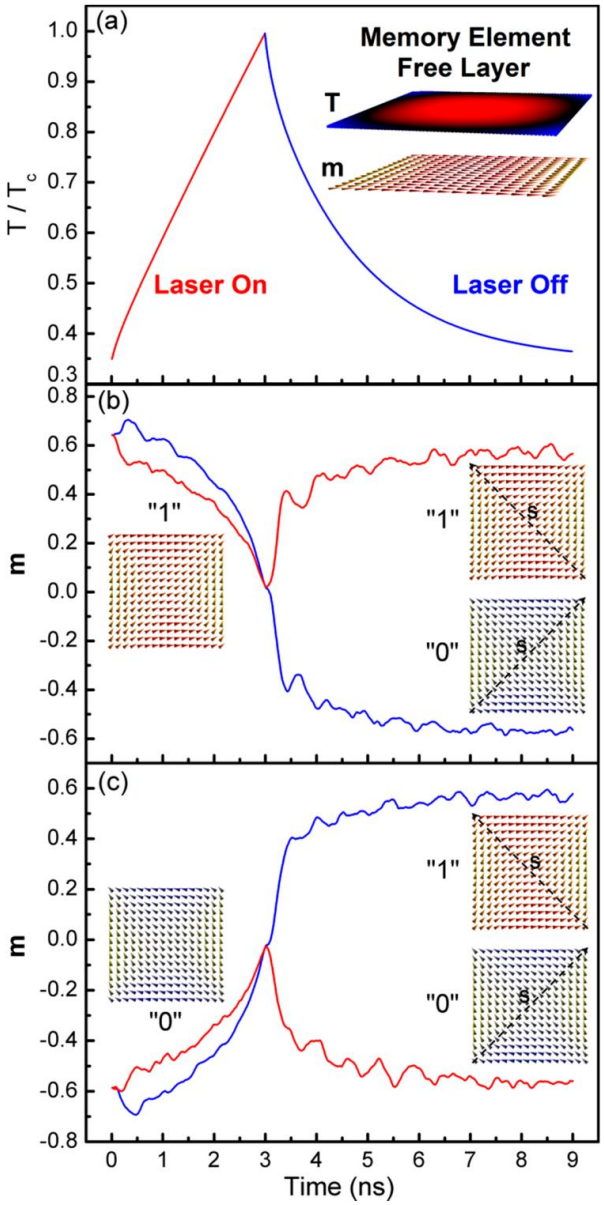

Figure 2.12 Heat-assisted strain-induced magnetization switching. (a) Heating and cooling of multiferroic layers during and after a laser pulse. The inset shows the temperature profile in the free layer; (b,c) heat-assisted magnetization switching starting from states "1" and "0" with two different stress directions.[23]

In experiments, Zhou *et al.* firstly studied the ME coupling properties in FM/AFE composites at high frequency (365 kHz).[27] The ME composite of Terfenol-D FM alloy and PLZST AFE ceramic was fabricated by bonding two components using glue with pressure and heating. They demonstrated that the magnetic field could enhance the *E*-induced strain and polarization of the composite, while the electric field can rise the magnetization at the electromechanical resonance frequency because the AFE ceramics exhibit ferroelectric behaviors under a high electric field [Fig. 2.13 (a) and (b)]. The induced magnetic moment increases with thickness ratio decreasing and shows a hysteresis loop with the bias magnetic field [Fig. 2.13 (c) and (d)]. Due to the antiferroelectric characteristics, it also shows a hysteresis loop with the bias electric field, which could be used in the magnetic switch controlled by electricity.

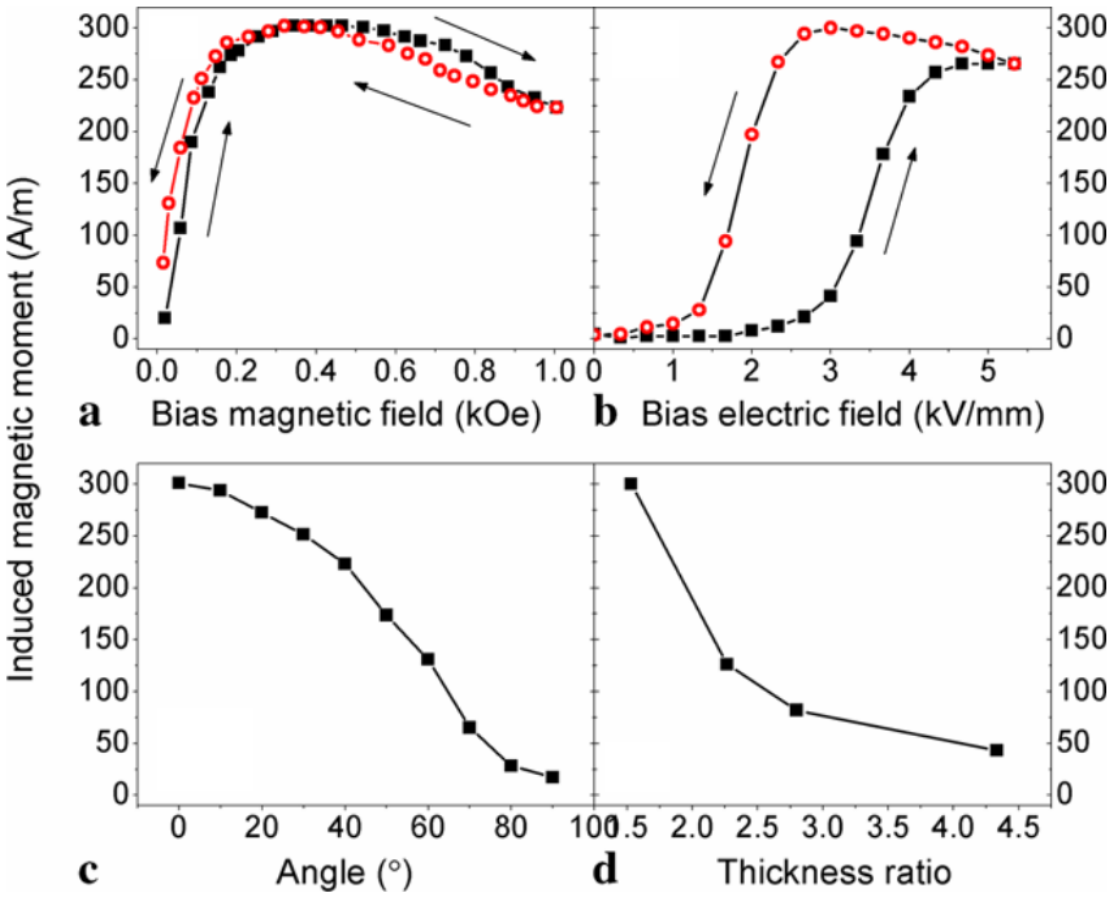

Figure 2.13 Induced magnetic moment variance with (a) the bias magnetic field, (b) the bias electric field, (c) the angle θ between the sample plane and magnetic field, and (d) the thickness ratio between Terfenol-D and PLZST at a resonance frequency of 365 kHz.[27]

Mirshekarloo *et al.* fabricated an FM/AFE multilayer through a bulk micromachining process on silicon wafers, and then the ME coupling effect was studied by the AC-mode magneto-optical Kerr effect technique.[99] They have revealed that the AFE to FE phase transformation of PLZST induced rotation of magnetization of about 0.5° in ferromagnetic Ni layer, persuaded by strain-induced anisotropy of about 0.5 kJ/m^3, as shown in Fig. 2.14.

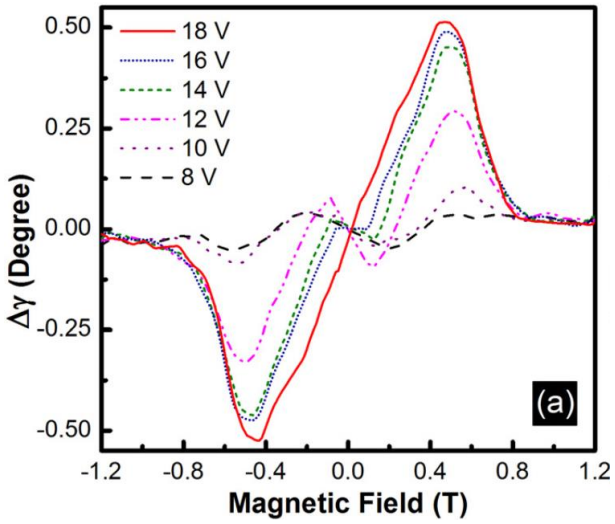

Figure 2.14 The magneto-optical Kerr effect signal converted to the oscillation amplitude of the magnetization vector ($\Delta\gamma$) measured at different AC voltages.[99]

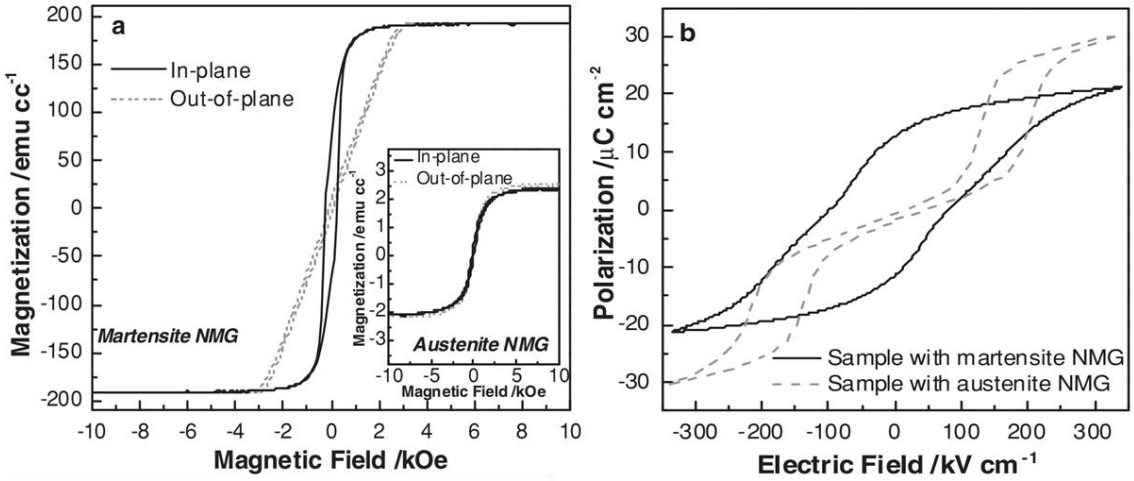

Figure 2.15 (a) *M-H* hysteresis loops of the austenite and martensite NMG thin films, (b) Out-of-plane *P-E* hysteresis loops of the PLZST films with austenite and martensite NMG film on the top, before and after annealing, respectively.[22]

Mirshekarloo *et al.* have also explored the strain-induced AFE-FE phase transformation in an FM/AFE ME composite of a PLZST layer underneath the magnetic shape memory (MSM) alloy Ni–Mn–Ga (NMG) thin film.[22] They discovered that the martensitic phase transformation of NMG film induced large strain was the origin causing the AFE–FE phase transformation regardless of the substrate clamping effect [Fig. 2.15 (b)].

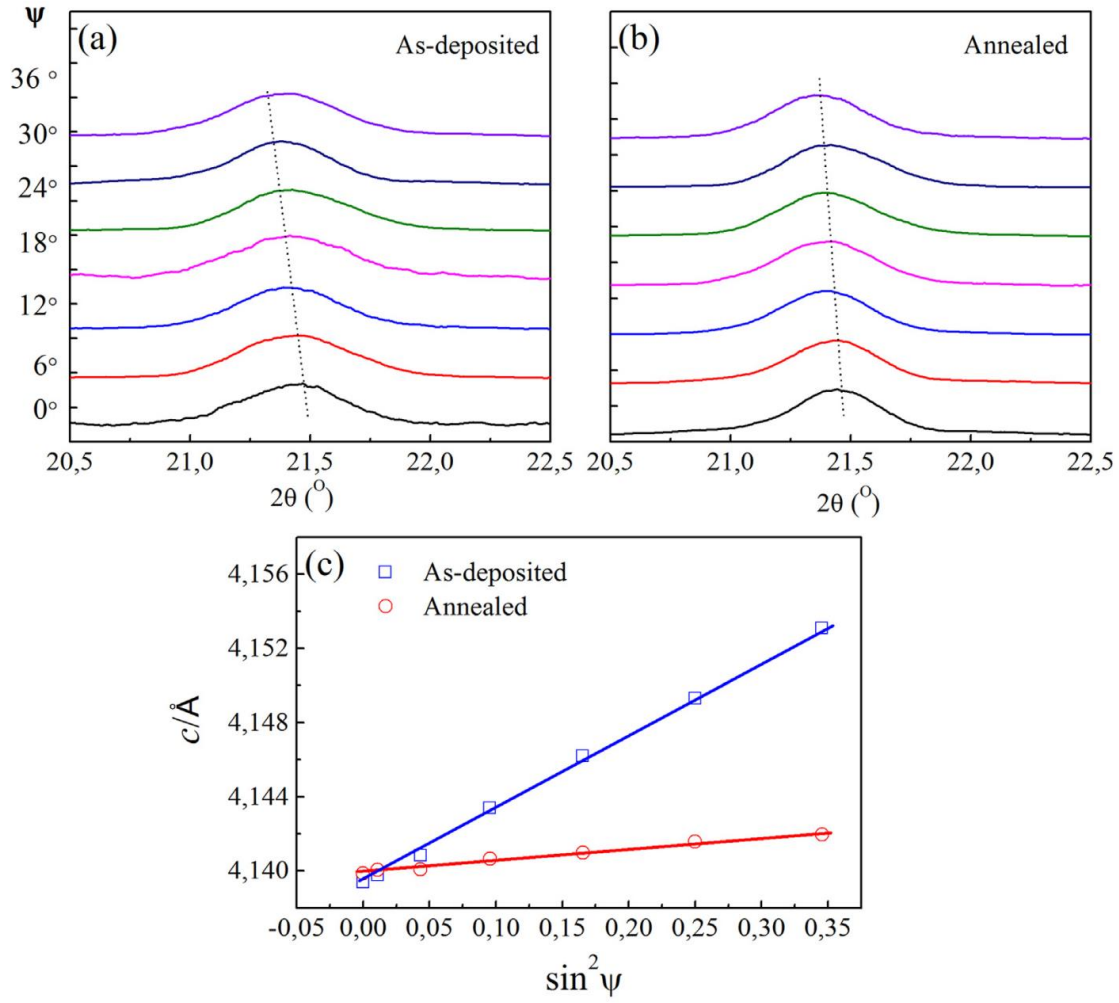

Figure 2.16 Enlarged view of PLZT (001) peaks measured under various tilt angles for (a) the as-deposited, and (b) the annealed samples, respectively. (c) d-spacing of PLZT (001) plane as a function of sin2ψ for the two samples.[37]

Recently, Wang *et al.* have fabricated an NMG/PLZT bilayer films to reveal further the interfacial stress-induced AFE-FE phase transition.[37] The NMG films were grown on PLZT-coated Pt/Si substrates, the austenite-martensite transformation of NMG top-layer during the annealing lead to the AFE-FE phase transition in PLZT film. They have made a quantitative residual stress analysis to reveal that the change of residual stress in the PLZT layer is up to 300 MPa during the annealing, which contributes to tuning the ferroelectric order of PLZT.

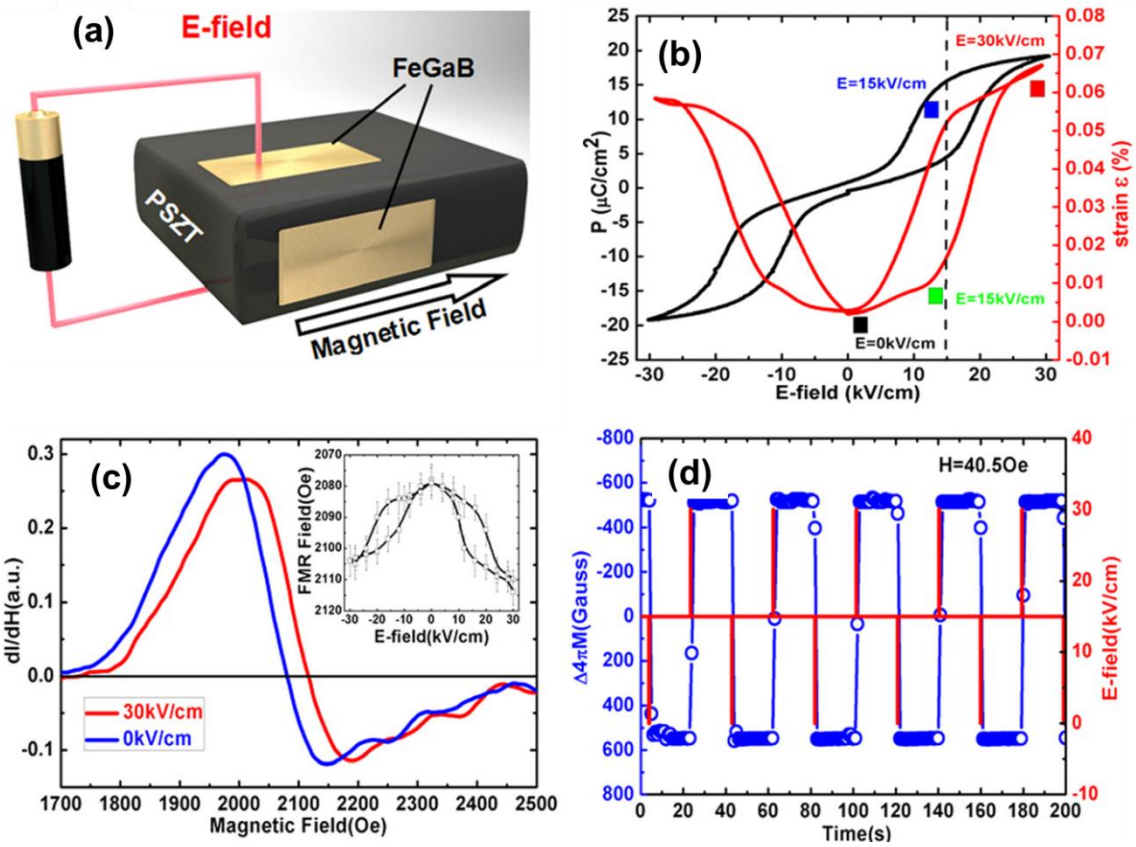

Figure 2.17 (a) The schematic of FeGaB film deposited on the top or on the side of PSZT ceramics, (b) *P*-*E* loop of PZST ceramic, (c) FMR spectra under varying *E*-field of FeGaB(top)/PSZT composites and inset the FMR field dependence of E-field, and (d) magnetization switch of FeGaB(top)/PSZT at 40.5 Oe induced by voltage impulse.[26]

Strong non-volatile voltage control of magnetization through *E*-induced AFE-FE phase transition in Pb(Zr, Sn, Ti)O_3 (PZST) ceramic has been achieved by Zhou *et al.*[26] The high strain/stress achieved by the FE–AFE phase transition in PZST leads to coercive field change of 7–10 Oe and FM resonance field shifts by 80 Oe in

FeGaB/PLSZT multiferroic heterostructure. They have deposited FeGaB thin films (50 nm) on the side or top of the PZST ceramic substrate [Fig. 2.17 (a)]. Due to the AFE-FE phase transition strain, the nonvolatile voltage induced FM resonance field shift and magnetization switching in FeGaB was obtained, as shown in Fig. 2.17 (c) and (d). Thus the magnetic properties (magnetization and FMR field) can be tuned by voltage. The nonvolatile voltage control of magnetism is showing promising applications in compact and power-effective multiferroic devices.

The large strain change from *E*-induced AFE–FE phase transition in AFE materials offers themselves great advantages to play a key role in realizing voltage control of magnetism. The present research of novel FM/AFE multiferroic structures has revealed a new path of design CME composites.

Since hundreds of literature focused on FE-based ME composites have been published, and various heterostructures have been brought out, the current research on AFE-based ME composites is quite limited. Only a few AFE-based ME heterostructures have been developed, and the published papers are less than ten. Thus, more AFE-based ME composites need to be developed. Besides, the difference of AFE- and FE-based ME composites in CME coupling effect is still unclear, which is necessary to understand these two type of heterostructures. Many applications of FM/FE composites have already been proposed, while few are related to AFE-based ME composites. The exploration of potential applications in AFE-based ME composites is also needed to be done.

3 Experimental Techniques

In this chapter, the experimental techniques used in this thesis are presented in detail. The fabrication of polycrystalline thin films and ceramics, the structural characterization and property characterizations are discussed.

3.1 Ceramic Synthesis

The ceramics preparation was finished by the author in Shanghai Institute of Ceramics, Chinese Academy of Science. The choice of FE (PMN-PZT) and AFE (PLZST) ceramics will be explained in chapter 4.

3.1.1 Raw materials

The ceramics were prepared by a conventional solid-state reaction. The raw powders used in this work are shown in Table 3.1.

Table 3.1 Main raw materials for the preparation of ceramics

Samples	Raw powders	Purity
$0.25(PbMn_{1/3}Nb_{2/3}O_3)$-$0.75(PbZr_{0.47}Ti_{0.53}O_3)$ (PMN-PZT)	Pb_3O_4	99.26%
	$MgCO_3$	99.98%
	Nb_2O_5	99.81%
	TiO_2	99.38%
	ZrO_2	99.99%
$(Pb_{0.97}La_{0.02})(Zr_{0.6}Sn_{0.3}Ti_{0.1})O_3$ (PLZST)	Pb_3O_4	99.26%
	La_2O_3	99.95%
	ZrO_2	99.99%
	SnO_2	99.5%
	TiO_2	99.38%

3.1.2 Solid-State Reaction Process

The raw powders were prepared by the conventional solid-state method according to the chemical formula of the ceramics with 0.5 wt.% excess Pb_3O_4 to compensate Pb

volatilization during sintering. The raw powders were weighed according to the compositions by the balance. Then, they were mixed with deionized water and milling ball according to the weight proportion of 1: (1.4 ~1.8) : (0.7 ~1.0). After 10 hours of ball milling, the mixed powders dried in the oven, sieved with mesh and then calcined at 850 ℃ for 2 hours. After calcination, the calcined powder was milled again for 24 hours and dried overnight before mixing with 6 wt.% of polyethylene glycol as a binder. Next, the calcined powders were uniaxially pressed into pieces of the disc with a thickness around 2 ~3 mm and a diameter of 15 mm. To decompose the binder fully, the green pellets were firstly put at 800 ℃ for 2 hours. Then for sintering, the green pellets were covered in a calcined powder of the same composition in a closed alumina crucible to avoid volatilization of Pb and sintered at 1240 ~1320 °C for 2 to 4 hours. Note that the heating and cooling rate used for both calcination and sintering was 2 °C/min.

3.1.3 Processing Techniques

The sintered pellets were mechanically ground to a final uniform thickness of approximately 0.5 mm. Then the silver electrodes were coated on two sides of the clean ceramic pellets through the screen printing technique, and the silver sintering was conducted at 700 ~750 °C for 15 ~30 minutes. Finally, the ceramic samples were ready for electrical measurements.

The sintered ceramics were machined and polished on both sides into the ceramic substrate. The roughness of the surface after polishing is about 10 nm. The substrate dimension is $10 \times 10 \times 0.5$ mm^3.

3.2 Thin Film Preparation

3.2.1 Magnetron Sputtering

Sputtering is one of the most common physical vapor deposition (PVD) techniques for fabricating thin films onto substrates. The sputtered films tend to be more uniform and dense with fine grain size (~ 10 nm) compared to other PVD methods.[100] Fig. 3.1 shows a schematic of a magnetron sputtering system. In this system, the target materials are connected to the negative terminal of a power supply, typically about a few kilovolts (kV), while the substrate may be grounded or biased positively.[101] The

chamber is first pumped down to a vacuum with the base pressure about 10^{-5} Pa, and then the working gas (typically, argon) is introduced and serves as a visible glow discharge medium between two electrodes. In the discharge, positive gas ions and electrons are produced and form a plasma. The ions strike the target and physically remove the target atoms. The target atoms enter and pass through the plasma region to eventually deposit onto the substrate and to form the film.[101] Sputtering methods include commonly direct current (DC) magnetron sputtering and radio-frequency (RF) magnetron sputtering. Typically, the former is used to sputter conductive materials, while the latter is used to sputter non-conductive materials. For magnetron sputtering, electrons and ions are trapped near the target by a magnetic field (*H*-field) to increase the plasma density and thus the deposition rate.[102]

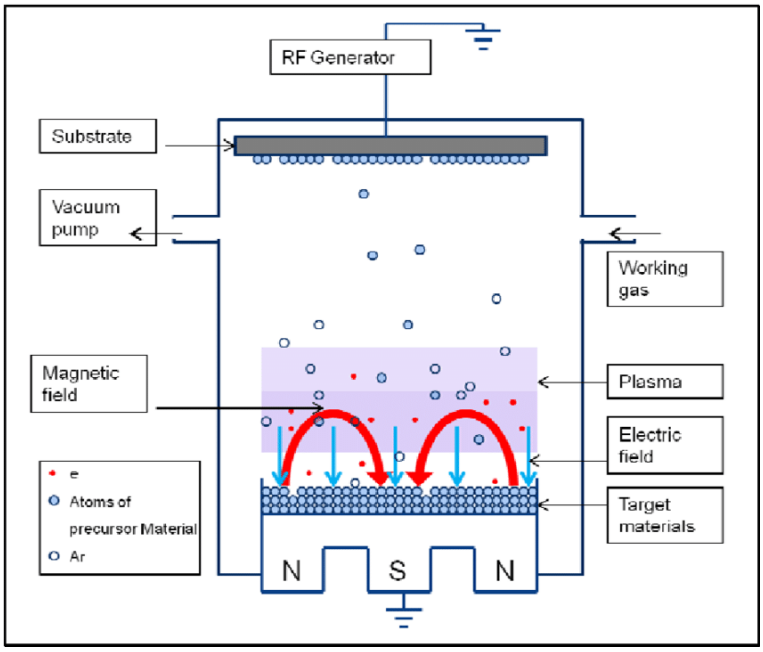

Figure 3.1 A principle schematic representation of RF magnetron sputtering[103]

Figure 3.2 RF magnetron sputtering system of Plassys.

In this work, the Plassys RF magnetron sputtering system was chosen to deposit YIG and NMG thin films onto Si substrate and polished ceramic substrates, as given in Fig. 3.2.

3.2.2 Targets Fabrication

Before the sputtering, the targets should be prepared first. In this work, the raw powders of Y_2O_3 and Fe_2O_3 were used to fabricate the YIG target. The raw powders were weighed according to the compositions by the balance. The total weight of raw powders was about 60 g. Then, they were mixed with propan-2-ol and milling ball for 10 hours of ball milling. Next, the mixed powders dried in the oven, sieved with mesh. Finally, the powders were pressed in cylindrical steel under the uniaxial pressure of 5, 10, 15, 20 Tons for 5 minutes, respectively. The targets are of thickness around 3 ~4 mm and a diameter of 3 inches.

The NMG magnetic alloy target with a composition of $Ni_{0.5}Mn_{0.33}Ga_{0.17}$ was bought from the company.

3.2.3 Electrodes Deposition

The Pt electrodes were included in some heterostructures, and metallic masks were used to confine the dimension of the electrodes. The Pt electrodes were deposited by DC magnetron sputtering process on Si or ceramic substrates.

3.3 Characterization Methods

3.3.1 Microstructural Characterization

(1) X-Ray Diffraction (XRD)

X-ray diffraction is powerful to determine the crystal structure, symmetry, and lattice parameters. In this study, we utilize an X-ray diffractometer (Rigaku D/MAX-2550, Japan) to characterize the phase structure of ceramics and thin films. The X-ray tube was operated at 40 kV and 40 mA with a wavelength of λ=0.154nm (Cu $K\alpha$).

(2) Atomic Force Microscope (AFM)

Atomic force microscope is to characterize the morphology, roughness, and other properties of surfaces on the atomic scale at environmental conditions. In this work, the surface morphology and roughness of the samples were measured using non-contact AFM (Nanonavi SII, Japan).

(3) Scanning Electron Microscope (SEM)

The scanning electron microscope is a useful magnification tool that utilizes focused beams of the electron to obtain information and provides high-resolution, three-dimensional images. The field emission SEM (JEOL/JSM-6700F, HITACHI/ FESEM-S4800, Japan) is used to characterize the morphology of thin films.

(4) Magnetic Force Microscope (MFM)

Magnetic force microscopy (MFM) is a kind of AFM where a magnetized tip can scan the magnetic sample and characterize the magnetic structure of the sample surface. In this work, the MFM (MultiMode, Bruker) measurements were performed with an external voltage applied to the sample by two probes at the same time to characterize the magnetic domain change with the electric field in ME composite films.

3.3.2 Electrical Measurements

The metal-insulator-metal (MIM) capacitor structure is built by depositing electrodes on the samples' surfaces.

(1) Dielectric Properties

The dielectric constant was measured using an LCR meter at a frequency of 100 – 100k Hz. The impendence analyzer HP 4284 and HP 4294A connected with VT 7004 and GJW-1 furnace. By measuring the capacitance of a sample, the dielectric constant is obtained from an equation as

$$\varepsilon_r = \frac{Cd}{A\varepsilon_0} \tag{3.1}$$

where C is capacitance (F), ε_0 is vacuum permittivity (8.85×10^{-12} F/m), A is the area of electrode surface (m^2), and d is the thickness of the sample (m).

(2) Ferroelectric Properties

The polarization-electric-field (*P-E*) hysteresis loops of samples were measured by TF Analyzer 2000 (aixACCT) system. The *P-E* loops can be measured in a temperature range from -40 ℃ to 200 ℃ and with a frequency of 1-5000 Hz.

(3) Strain Measurements

The strain-electric-field (*S-E*) curves of samples were also measured by TF Analyzer 2000 (aixACCT) system. The ceramics were characterized by TF Analyzer 2000 equipped with a laser interferometer vibrator.

3.3.3 Magnetic Properties Characterization

The vibrating sample magnetometer (VSM) system is used to test the low-frequency magnetic properties of magnetic materials. A typical VSM system includes an electromagnet to provide the DC magnetic field, a vibrating stage to vibrate the sample, and a pick-up coil assembly that measures the magnetization of the sample according to Faraday's law of induction. The output is usually the magnetic moment M or flux B vs. the field H. The magnetic hysteresis loops (*M-H*) are measured at room

temperature by using a VSM (ADE model EV9) with a vibration frequency of 75 Hz.[104]

3.3.4 Magnetoelectrical Properties Characterization

For the measurements of the magnetoelectric effect, a home-made system was set up based on VSM, as shown in Fig. 3.3. A voltage supply (High voltage supply, SRS Model PS350) was equipped to apply an electric field during the measurements. The sample is put into VSM while two Cu wires are attached to the electrodes of the sample. Thus, the electric field and magnetic field can be applied to the sample simultaneously. It is necessary to calibrate the measurements to exclude offset the influence of the substrate, electrodes, and wires. Thus we can record the magnetic response of YIG film only is recorded.

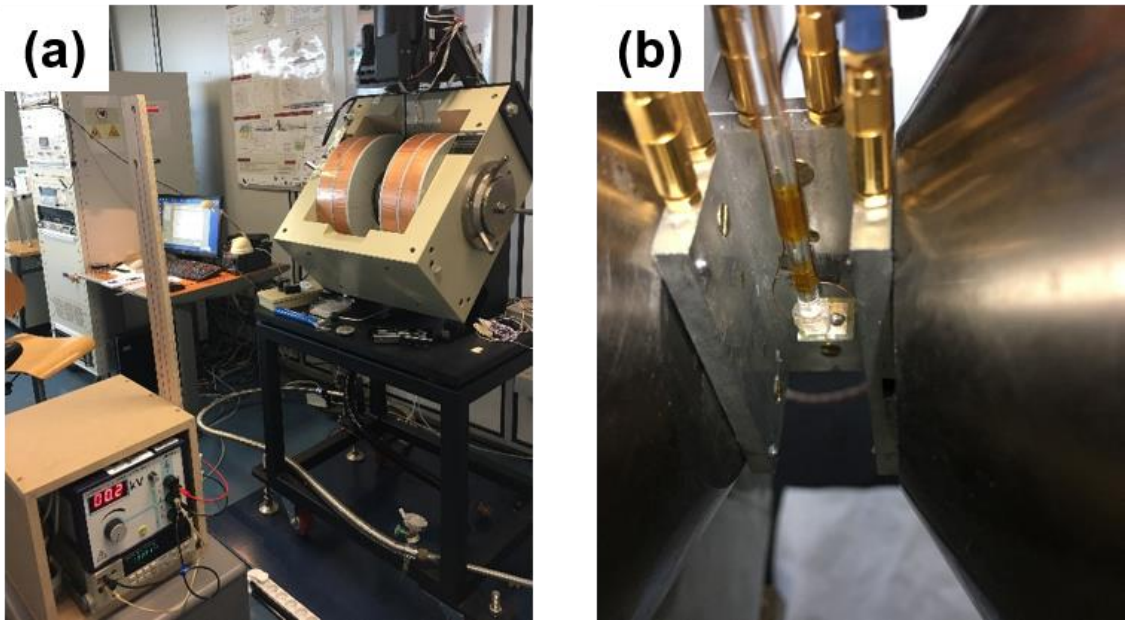

Figure 3.3 (a) Home-made VSM system, (b) Connected sample.

4 FE and AFE Ceramic Substrates

The AFE bulk materials have been developed for decades, but most of them are ceramics. Several researchers have tried to fabricate AFE single crystals,[105–107] but the preparation process of AFE single crystals is not mature, and they have not been widely used in other fields. Therefore, the AFE ceramic is a good choice for us to use in ME heterostructures. As a comparison, the FE ceramic is also selected in this study.

4.1 PMN-PZT FE Ceramic Substrates

4.1.1 Introduction

In strain-mediated multiferroic composites, the FE materials are usually materials with considerable *E*-induced strain, such as Pb(Zr, Ti)O_3 ceramics and Pb($Mg_{1/3}Nb_{2/3}$)O_3-$PbTiO_3$ single crystal.[108–111] PZT ceramics are the most well-known ones because of their excellent piezoelectric properties. PMN is a representative of relaxation ferroelectric material due to its high electrostriction, relaxation behavior, and high dielectric constant. Therefore, the solid solution between PMN and PZT has superior dielectric, piezoelectric, electromechanical coupling, and electrostrictive properties than single PMN and PZT.[112–114]

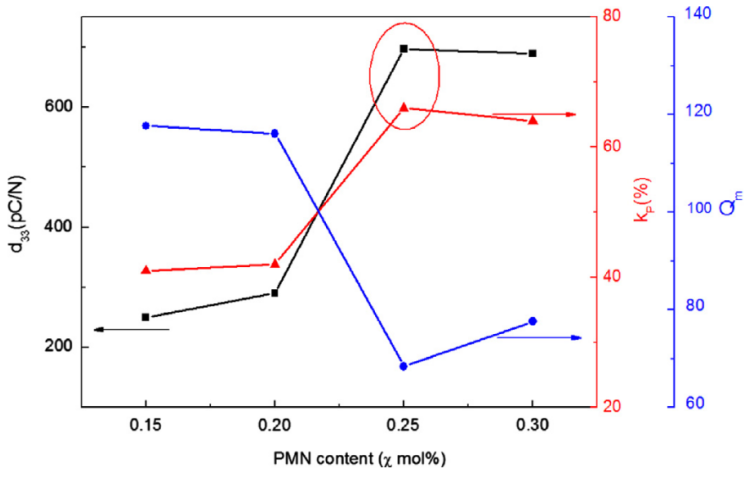

Figure 4.1 Piezoelectric coefficient d_{33}, electromechanical coupling factor k_p, and quality factor Q_m of the *x* PMN– (1-*x*) PZT ceramics.[115]

It has been reported that 0.25PMN–0.75PZT possessed superior piezoelectric properties due to its composition close to the MPB. The composition near the

morphotropic phase boundary (MPB) enables the existence of multiple polarization directions and consequently facilitates domain reorientation, which should be responsible for the superior piezoelectric properties. A sizeable piezoelectric coefficient (d_{33}) of 698 pC/N was obtained. Notably, a large field-induced strain of 2.2% (at 4 kV/cm) was attained, which shows an excellent potential for the ME coupling effect.[115]

4.1.2 Preparation of PMN-PZT Ceramic Substrates

The PMN-PZT ceramic was prepared by conventional solid-state reaction, as described in Chapter 3. After sintering, the ceramic was machined and polished into substrates with a dimension of 8 × 8 × 0.5 mm^3. The AFM picture of polished PMN-PZT surface and XRD pattern of PMN-PZT ceramic powders are given in Fig. 4.2. The well-polished surface can reach an average roughness of ~17 nm, which is lower enough for thin film growth. The XRD patterns of PMN-PZT illustrate that the ceramic is well-prepared, and no second phase can be detected.

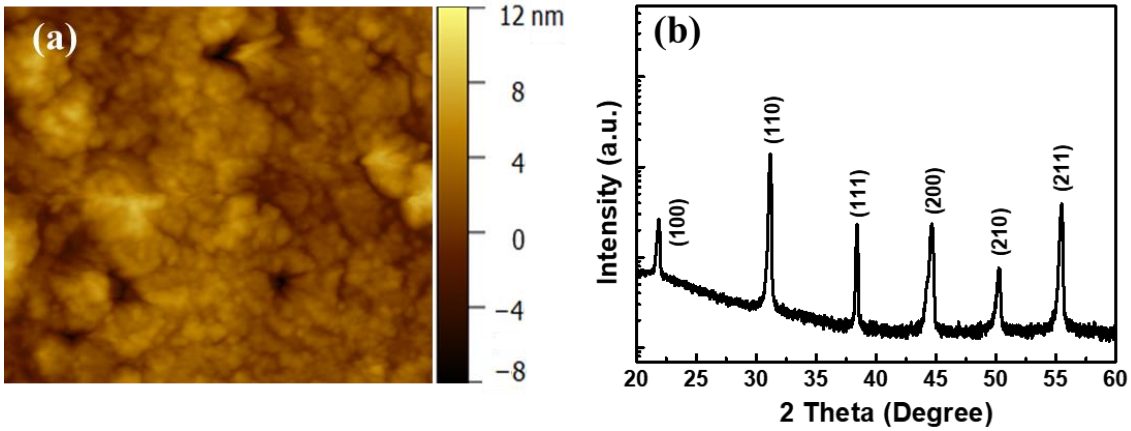

Figure 4.2 (a) AFM picture of the polished PMN-PZT substrate surface, (b) XRD patterns of PMN-PZT ceramic powders.

It is necessary to point out that, the roughness of polished PMN-PZT ceramic substrate measured by AFM was with a scanning range of 5 ~15 μm. In this scanning range, the polished PMN-PZT ceramic substrate shows smooth and even surface with an average roughness of 17 nm. However, on a large scale of view, the PMN-PZT ceramics prepared by the conventional solid-state reaction are inevitable to present holes, as given in Fig. 4.3. The polycrystalline ceramics cannot be perfect, and there are some holes between different grains. Thus the relative density of ceramics prepared

by the conventional solid-state reaction cannot reach 100%. In this work, the relative density of PMN-PZT ceramics is 96.3% through the Archimedes method, which is quite high when compared with other ceramics prepared by conventional solid-state reaction.[116–118]

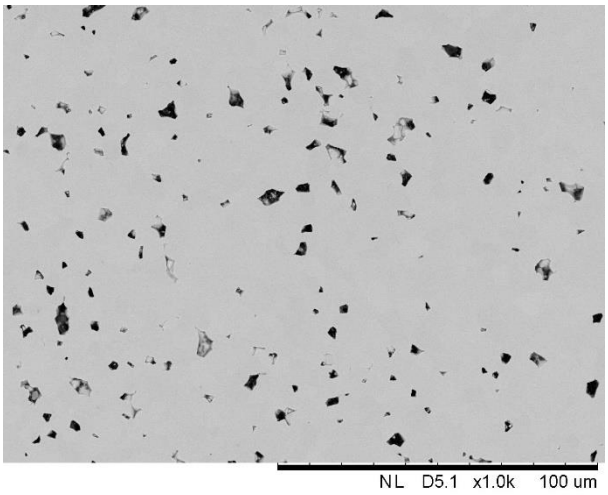

Figure 4.3 SEM picture of the polished PMN-PZT substrate surface.

Then the Pt electrodes were deposited on two sides of PMN-PZT ceramic substrates to measure its electrical properties, as given in Fig. 4.4. The X, Y, and Z axis are marked in the figure to demonstrate the electric-field-induced strains measured along different axes. The in-plane (X and Y axes) strain was measured with gauges attached to the PMN-PZT ceramic, while the out-of-plane (Z axis) strain was measured through TF Analyzer 2000 equipped with laser interferometer vibrator.

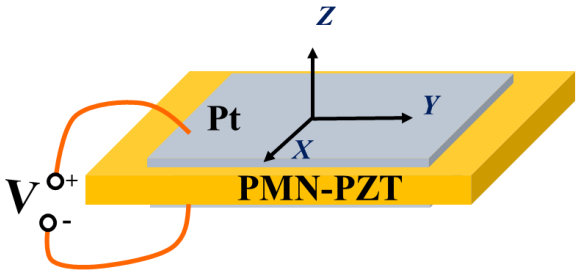

Figure 4.4 Schematic of PMN-PZT ceramic substrates for electrical measurements.

4.1.3 Results and Discussion

The PMN-PZT ceramics are in the ferroelectric phase with the coexistence of tetragonal and rhombohedra structures.[115] The Curie temperature of PMN-PZT ceramic is 197 °C. Figure 4.5 shows the *P-E* hysteresis loop of PMN-PZT ceramic substrate. The remnant polarization is 34 μC/cm^2, and the saturate polarization is 38

μC/cm^2, indicating strong ferroelectricity in PMN-PZT. The coercive electric field (E_C) of PMN-PZT is low, about 4.2 kV/cm.

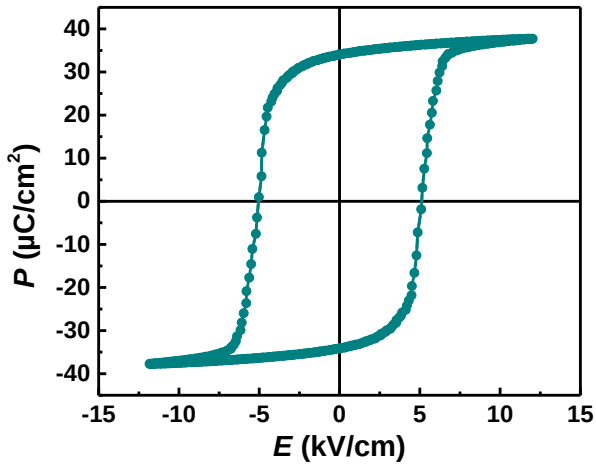

Figure 4.5 The *P*-*E* loop of PMN-PZT ceramic substrate.

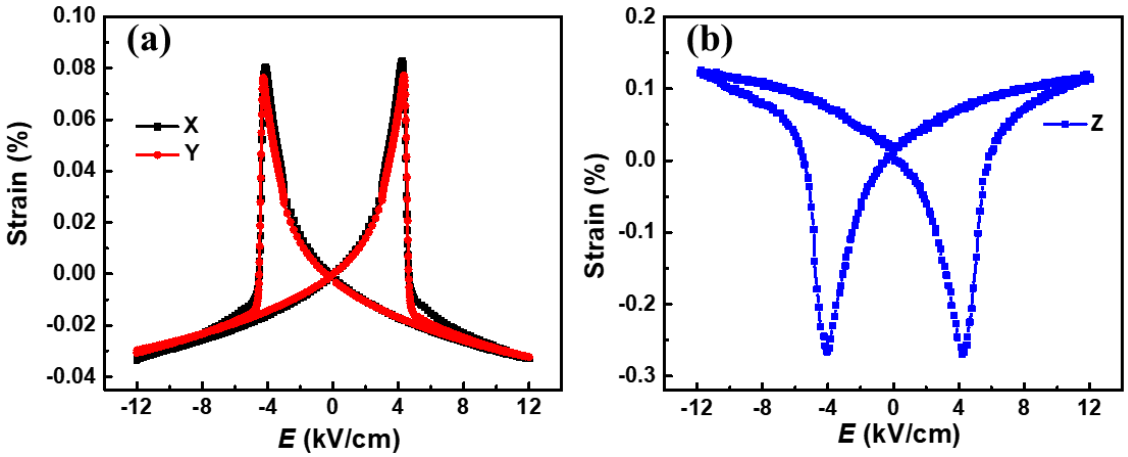

Figure 4.6 (a) The in-plane strain and (b) out-of-plane strain of PMN-PZT ceramic substrate.

The *S*-*E* curves along X and Y axes are the in-plane strain of PMN-PZT ceramic substrate, as shown in Fig. 4.6 (a). Since the ceramic is polycrystalline, the in-plane strains (X strain and Y strain) are the same in theory. The subtle differences in Fig.4.6 (a) are caused by the different minor placement of strain gauges during the measurements. With an application of the electric field, the in-plane tension strain is generated, while a compressive strain is generated along the Z axis, given in Fig. 4.6 (b). Thus the in-plane butterfly *S*-*E* curve and out-of-plane butterfly *S*-*E* curve are axis-symmetric, reaching the sharp strain peaks at the coercive electric field. The maximum of out-of-plane strain can be -0.27% at a small electric field of 4.2 kV/cm, and the in-

plane strain peak is 0.08%. The large electric-field induced strain change serves to promote the strain-mediated magnetoelectric effect in PMN-PZT-based multiferroic heterostructure.

4.1.4 Summary

The $0.75Pb(Mg_{1/3}Nb_{2/3})O_3$-$0.25Pb(Zr_{0.48}Ti_{0.52})O_3$ ceramic is chosen as the piezoelectric phase to couple with FM films in this work due to its high *E*-induced strain. The composition of 0.75PMN-0.25PZT is around the morphotropic phase boundary, where excellent piezoelectric performance exists. The 0.75PMN-0.25PZT ceramics were prepared by solid-state reaction, and average roughness of 17 nm can be reached in polished PMN-PZT ceramic substrates. The E_C of PMN-PZT ceramics is as low as 4.2 kV/cm, while the *E*-induced in-plane and out-of-plane strain can reach 0.08% and -0.27% at E_C, respectively.

4.2 PLZST AFE Ceramic Substrates

4.2.1 Introduction

The distinctive electromechanical coupling properties of AFE materials have attracted increasing attention ever since the first AFE compound $PbZrO_3$ was discovered by Kittel in 1951.[44] A typical example is the lightly lanthanum-doped, lead zirconate stannate titanate (PLZST) system. The PLZST system has displayed extremely high electric-field-induced longitudinal and volume strains, especially in the compositions close to the morphotropic phase boundary between the antiferroelectric and ferroelectric phases, as marked in Fig. 4.7. It has been reported that PLZST exhibits large *E*-field-induced strain (e.g., maximum 0.87% for bulk ceramics and 0.49% for thin films),[94–96] potentially enabling a range of device applications, such as actuators, sensors, electrocaloric devices, energy harvesting, and storage devices.[119] Such high strains have been considered to be related to a reversible, *E*-field-induced, tetragonal antiferroelectric (AFE_T) to rhombohedral ferroelectric (FE_R) phase transition.[120]

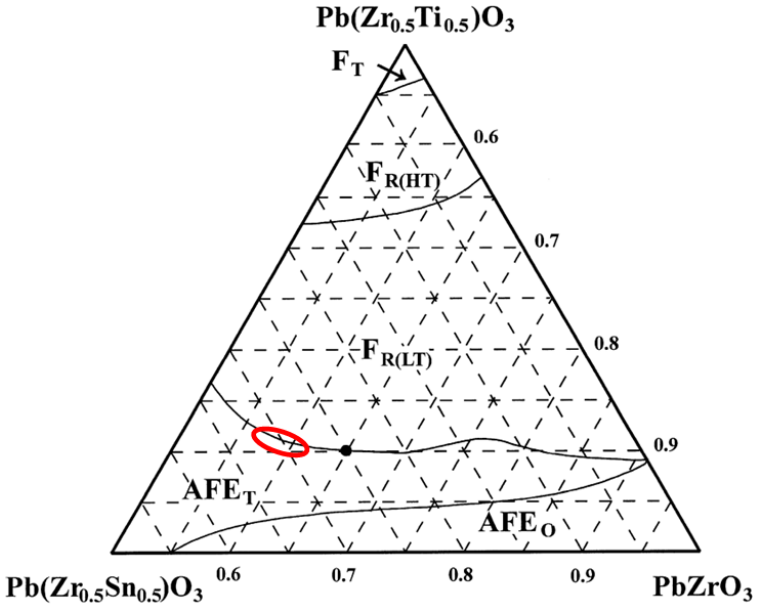

Figure 4.7 Ternary phase diagram of the $Pb_{0.97}La_{0.02}$(Zr, Sn, Ti)O_3 system.[121]

4.2.2 Preparation of PLZST Ceramics

The $Pb_{0.97}La_{0.02}Zr_{0.6}Sn_{0.3}Ti_{0.1}O_3$ (PLZST) ceramic, as a typical AFE material in the compositions close to the morphotropic phase boundary between the antiferroelectric and ferroelectric phases,[121] is selected to be the AFE ceramic substrate. The PLZST ceramic substrates are prepared by conventional solid-state reaction, as mentioned in Chapter 3.1. Then the sintered PLZST ceramic was machined and fine polished into 10 × 10 × 0.5 mm^3 substrates.

The AFM image of the PLZST substrate surface of PLSZT ceramic is given in Fig. 4.8 (a). The PLZST ceramic is well polished with an average roughness of ~10 nm. The XRD pattern of PLSZT ceramic is given in Fig. 4.8 (b), and the AFM image of the PLZST substrate surface is inset. The PLZST substrate is well-crystallized into the tetragonal AFE phase with small traces of lead oxide phase, which is due to the lead excess in the ceramic preparation process.

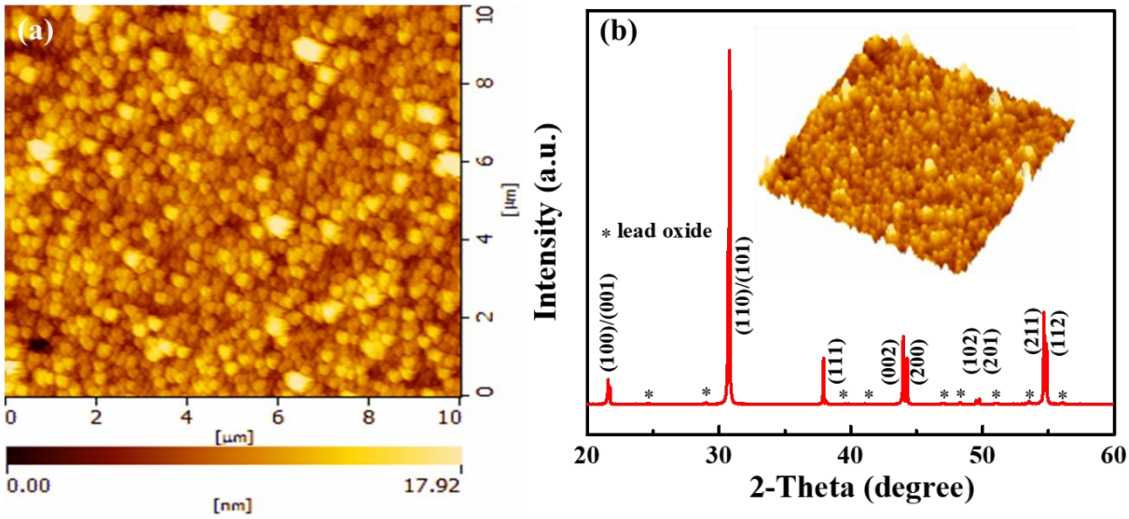

Figure 4.8 (a) The AFM picture and (b) XRD pattern of PLZST ceramic substrate.

As it has been explained in Chapter 4.1, the measurement of roughness in the polished ceramic substrate was carried out with a scanning range of 5 ~15 µm. However, the polished PLZST ceramic substrates are inevitable to present holes in a large scale of view because the relative density cannot reach 100% through conventional solid-state reaction. Figure 4.9 illustrates the surface of the PLZST ceramic substrate with a scanning view of 200 µm. In this work, the relative density of PLZST ceramics is 96.8% through the Archimedes method, which is quite high when compared with other ceramics prepared by conventional solid-state reaction.[116–118]

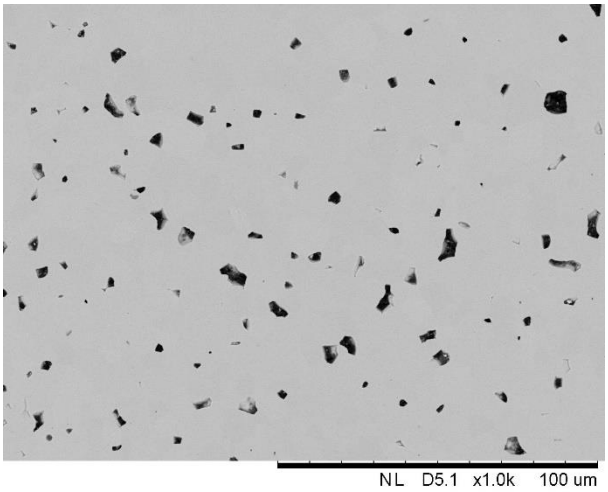

Figure 4.9 The surface SEM picture of the PLZST ceramic substrate.

4.2.3 Results and Discussion

The *P-E* loop and out-of-plane *S-E* curve of PLZST ceramic given in Fig. 4.10 shows a typical AFE characteristic. The forward and backward switching fields of PLZST are 5 kV/mm and 2.5 kV/mm, respectively. Once the electric-field-induced phase transition between the tetragonal AFE phase and the rhombohedral FE phase happens, a large strain change is generated simultaneously. The maximum strain value along out-of-plane direction can reach 0.2 %, whereas a considerable strain along in-plane can also be expected, which provides opportunities for strain-mediated CME coupling effect.

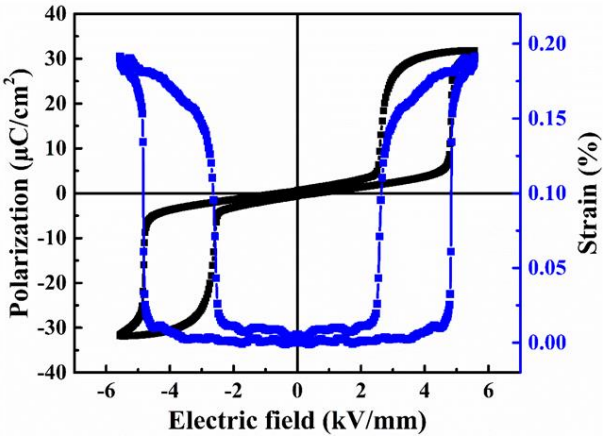

Figure 4.10 The *P-E* loop and *S-E* curve of the PLZST ceramic substrate.

4.2.4 Summary

In this part of the work, the $Pb_{0.97}La_{0.02}Zr_{0.6}Sn_{0.3}Ti_{0.1}O_3$ (PLZST) ceramics, as a typical AFE material in the compositions close to the morphotropic phase boundary between the antiferroelectric and ferroelectric phases,[121] were prepared to be the AFE ceramic substrate for its high electric-field-induced strain. The AFE-FE switching field of PLZST is 5 kV/mm with a maximum strain of 0.2 %.

4.3 Conclusions

The PMN-PZT FE and PLZST AFE ceramic substrates have been prepared and characterized in this chapter. The ceramic substrates were fabricated by the conventional solid-state reaction method, and the ceramics were machined and well-polished to reach a low average roughness (< 20 nm) despite the inevitable defects in

ceramics. The existence of these defects (holes) may have an influence on the CME coupling performances. The E_C of PMN-PZT ceramics is as low as 4.2 kV/cm, while the *E*-induced in-plane and out-of-plane strain can reach 0.08% and -0.27% at E_C, respectively. The AFE-FE switching field of PLZST is 5 kV/mm with a maximum strain of 0.2 %.

The good electric field-induced strain in PMN-PZT and PLZST ceramics gives us a way to fabricate FE- and AFE- based ME composites based on these ceramic substrates and reach good CME coupling effect. Moreover, the comparison of the performance of FE- and AFE- based ME composites can be carried out subsequently.

5 CME Coupling Effect in NMG/AFE Heterostructure

5.1 Introduction

Previous researchers have studied a variety of layered ME heterostructures of FM and FE components.[7,20–22] Actually, the main interest has been focused on FM/FE heterostructures and in particular the electric-field tuning of magnetic response resulting from the strain of FE component transferred to FM component, such as $CoFe_2O_4/BaTiO_3$, $Ni_{0.8}Zn_{0.2}Fe_2O_4/Pb(Zr,Ti)O_3$, Terfenol-D/$Pb(Mn,Nb)O_3$-$PbTiO_3$, FeBSiC/PVDF and so on. [16–19] AFE materials, with novel properties of electric-field-induced AFE/FE phase transition, exhibit a large and sharp strain change during the phase transition for atomic rearrangements and zero polarization and strain in a relaxed state. On the one hand, the significant strain of AFEs, which can reach 0.87 % in some AFE ceramics, make them extremely attractive for strain-mediated ME coupling.[122] On the other hand, the non-remnant state of AFEs results in no pre-poling process which shows good compatibility with various applications.[25] Concerning AFEs, a large strain can be obtained once the electric field is higher than the switching field, which provides a large practical operating voltage range for strains. So, the distinct characteristics of AFE materials give an additional opportunity to the electric field tuning of magnetism. However, very few works are dedicated to ME coupling of FM/AFE heterostructures, which seems to be interesting and promising in multiferroic composites.[26,27]

In order to observe the distinct coupling effect, the AFE PLZST ceramic bulk is selected to couple with FM layers, and the voltage-controlled magnetization switching and magnetic susceptibility variations are studied in different heterostructures.

In strain-mediated CME heterostructures, a strong coupling between elastic and magnetic domains is required for the magnetic component.[36] The Ni-Mn-Ga (NMG) alloys have attracted much attention as they combine both magnetic and elastic ordering. These properties make it possible to manipulate their ferroelastic domains by applying a magnetic field or mechanical stress.[40] These characteristics provide opportunities to induce a large magnetization change in NMG by an external mechanical stimulus, which is suitable for strain-mediated CME coupling.

Mirshekarloo and Wang *et al.* have studied NMG/AFE bilayers in the past, and the strain of austenite-martensite transformation in the NMG top layer can lead to AFE-FE phase transition in AFE films.[22,27,37] They have demonstrated the strain-induced AFE-FE phase transition, as well as strain-induced polarization change, in NMG/AFE heterostructures. However, the strain-mediated magnetization switching has never been studied in these structures.

Thus, evoked by the previous study of NMG/AFE heterostructure, the *E*-induced magnetization would be revealed in this part. The NMG film was considered for the FM phase as well as the electrode because of its strong combination of magnetic and elastic orderings and good conductivity.[40]

5.2 Preparation of NMG/PLZST/NMG

5.2.1 Film Growth

The NMG films were deposited using a "Plassys" RF sputtering system with a nominal alloy-composition target of $Ni_{0.5}Mn_{0.33}Ga_{0.17}$. The sputtering condition and annealing process of NMG films were referred to from reported work.[37,123] The details of the sputtering condition are given in Table 5.1.

Table 5.1 Sputtering parameters of NMG films

Sputtering Condition	NMG
Vacuum (Pa)	$< 3 \times 10^{-4}$
Power (W)	60
Temperature (°C)	RT
Atmosphere	Ar
Pressure (Pa)	1

After the deposition, the samples were annealed in a furnace to be crystallized. The annealing process is given in Table 5.2.

Table 5.2 Annealing parameters of NMG films

Annealing Condition	NMG

Heating Rate (℃/min)	2
Annealing (℃)	300, 400, 500
Duration (min)	60
Cooling Rate (℃/min)	2
Atmosphere	Air

To explore the annealing temperature of NMG films, three NMG/Si samples were prepared and annealed at 300, 400, and 500 ℃, respectively. Figure 5.1 shows the XRD patterns of NMG film annealed at different temperatures. It can be clearly observed that the austenitic NMG film is crystallized at 500 ℃ where the sharp Bragg peak (2θ ~ 43°) presents. The low FWHM of NMG film also indicates the good crystallization happens at 500 ℃.

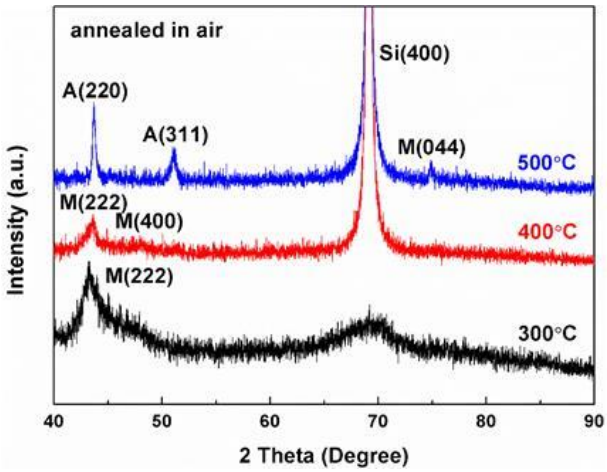

Figure 5.1 The XRD patterns of NMG films on Si substrates (A: Austenite; M: Martensite).

The magnetic hysteresis loops of NMG films annealed at different temperature is given in Fig. 5.2. The saturated magnetization of NMG films varies greatly with annealing temperature. The bad crystallization of NMG films annealed at 300 and 400 ℃ results in very low saturated magnetization. While the NMG film annealed at 500 ℃ shows the best magnetic performance, which confirms the NMG films can be well crystallized at 500 ℃ once again.

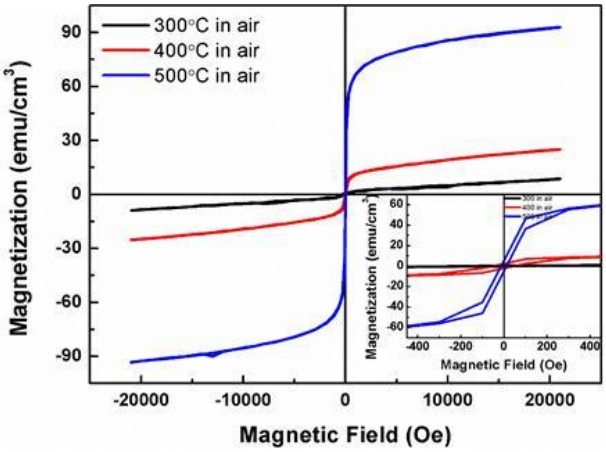

Figure 5.2 The magnetic hysteresis loops of NMG films on Si substrates annealed at different temperatures.

Thus the deposition and annealing process of NMG film is confirmed. The NMG films annealed at 500 ℃ can be well crystallized and present good magnetic performance. The growth of NMG films lays the foundation for preparing NMG/AFE ME composites.

5.2.2 ME Heterostructure Fabrication

The NMG films with a thickness of 700 nm (in this case, the ME signal is too weak to detect when the thickness of NMG is low) were deposited on the two sides of PLZST substrates by above mentioned sputtering and annealing process. Since NMG film is conductive, the NMG film is worked as electrodes as well. Thus the NMG/PLZST/NMG multiferroic heterostructure was fabricated, as illustrated in Fig. 5.3. The NMG polycrystalline film is isotropic, so the direction of the in-plane magnetic field does not matter and can be indifferently along the *x* or *y* axis.

Figure 5.3 Schematic of NMG/PLZST/NMG multiferroic heterostructure.

As the multiferroic composite interface quality plays a vital role in the magnetoelectric coupling,[124,125] the NMG/PLZST/NMG interface has been checked, as shown in Fig. 5.4 (a). The interface is clear, indicating no significant diffusion between the film and the ceramic substrate. The XRD patterns of NMG films on well-polished PLZST ceramic and Si/SiO_2 substrates are given in Fig. 5.4 (b). The presence of Bragg peak ($2\theta \sim 43°$) in NMG/PLZST, which can be indexed as (220) cubic setting corresponds to the austenitic phase of $Ni_2Mn_{0.85}Ga_{0.85}$, as we have reported previously.[123]

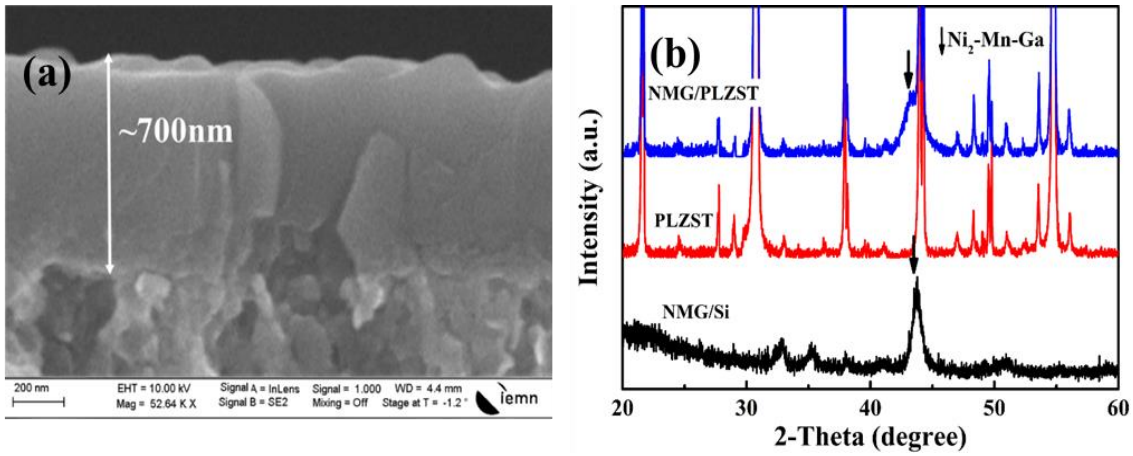

Figure 5.4 (a) The cross-sectional SEM picture of NMG/PLZST and (b)XRD patterns of NMG/Si, PLZST, and NMG/PLZST samples.

5.3 *E*-field controlled magnetization switching in NMG/PLZST/NMG Heterostructure

A typical *M-H* loop is observed in NMG/PLZST/NMG heterostructure when the magnetic field is parallel to the film plane, as shown in Fig. 5.5. The NMG film is isotropic in the plane. Thus the in-plane *M-H* loops along X or Y axis are the same. The NMG film shows good magnetic properties on the PLZST AFE ceramic substrate.

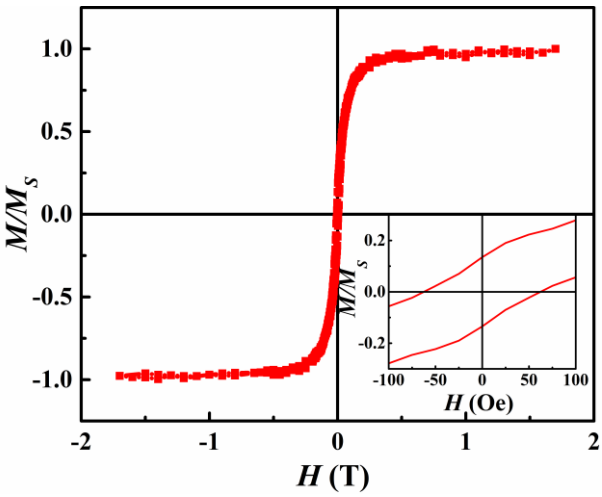

Figure 5.5 The *M-H* loop of NMG/PLZST/NMG heterostructure.

The *M-H* loops of NMG/PLZST/NMG heterostructure under different electric fields were measured by VSM system. As we have mentioned before, the switching field of PLZST ceramic is 5 kV/mm. So the *M-H* loops of the heterostructure without the electric field, with the electric field lower than switching field and with the electric field higher than switching field are given in Figure 5.6. There is a reduction of magnetization when the applied electric field is higher than the switching field of PLZST ceramic in the range of -1500 Oe ~1500 Oe.

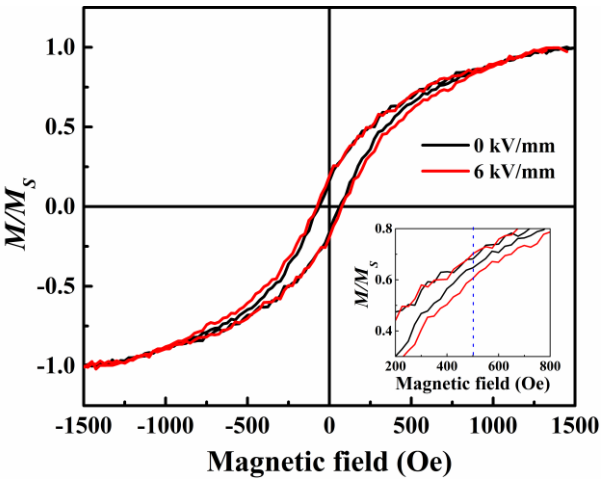

Figure 5.6 The *M-H* loop of NMG/PLZST/NMG heterostructure with and without an electric field.

The *M-E* curves of NMG/PLZST/NMG heterostructure were carried out under different magnetic fields, and several relative magnetization changes ($\Delta M/M_0$) versus *E* curves are illustrated in Fig. 5.7 (a) as representatives. The ($\Delta M/M_0$)-*E* loops are

symmetric with positive and negative E (as confirmed by Fig. 5.9 (a)), thus only the ($\Delta M/M_0$)-E curves under positive voltages are given. All the curves show a similar horn-like shape, and sharp reductions of $\Delta M/M_0$ happening at the switching field of PLZST.

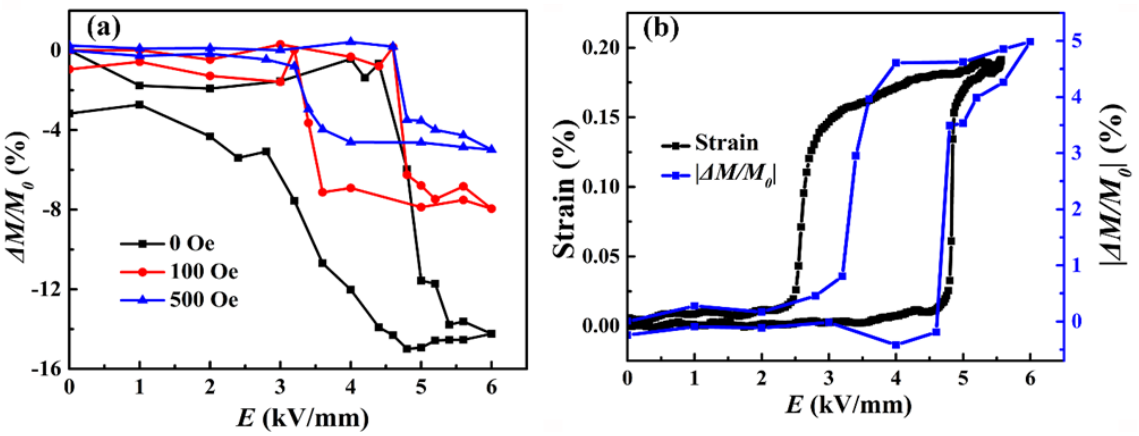

Figure 5.7 (a) ($\Delta M/M_0$)-E curves under bias magnetic field of 0, 100 and 500 Oe, and (b) S-E curve and $|\Delta M/M_0|$-E loop measured at 500 Oe of NMG/PLZST/NMG heterostructure.

To better reveal the relationship between strain and magnetization change, the absolute value of $\Delta M/M_0$ versus E ($|\Delta M/M_0|$-E) curve and S-E curve of PLZST are given together in Fig. 5.7 (b) for 500 Oe. The $|\Delta M/M_0|$-E curve is in good agreement with the S-E curve of PLZST. Once a large strain is generated in the PLZST substrate upon application of the electric field, the magnetization of NMG films greatly decreases, indicating a strong converse ME coupling effect. In theory, the field-induced strain originating from the field-induced AFE-FE phase transition deformation of the PLZST ceramic leads to anisotropy change in NMG films. In this case, the PLZST strain changes the magnetic domain configuration, which leads to a magnetization reduction, and the sign of $\Delta M/M_0$ is negative. The strain destroys the alignment of well-ordered magnetic domains and favors to rotate magnetic moments toward the opposite direction. The high agreement of S-E and $|\Delta M/M_0|$-E evolution demonstrates that AFE materials with strong electric-field-induced phase transition strain show great potential in ME coupling effect and can be promising candidates for multiferroic heterostructures.

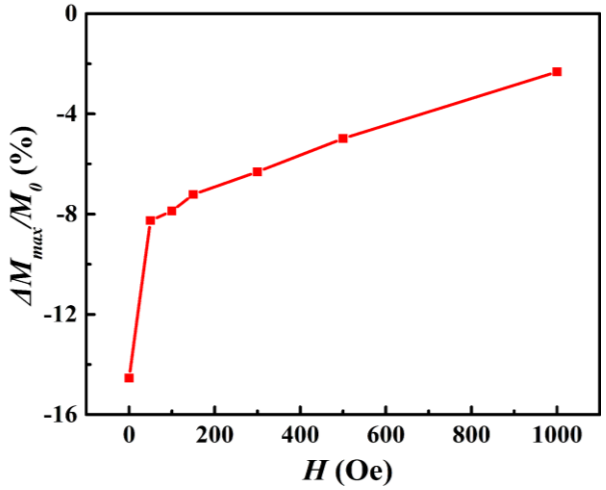

Figure 5.8 The ($\Delta M_{max}/M_0$)-H curve of NMG/PLZST/NMG heterostructure.

Figure 5.8 shows the curve of E-induced $\Delta M/M_0$ changing with the bias magnetic field. It can be seen that the maximum of $\Delta M/M_0$ (15%) is reached at 0 Oe, which is a very important asset in terms of design simplification and cost reduction, thus suggesting significant potential for future ME devices. With the bias magnetic field increases, the $\Delta M/M_0$ reduces quickly, indicating that it becomes difficult for the electric field induced strain to destroy the alignment of well-ordered magnetic domains and rotate them to other directions.

In Fig. 5.9 (a), the relationship between electric field tuning magnetization change and CME coefficient is illustrated. Since the sharp magnetization change occurs at the forward and backward switching fields of PLZST ceramic, four peaks of the CME coefficient happen correspondingly to the four switching fields. The peak values of the CME coefficient versus bias H curves are given in Fig. 5.9 (b). The ($\Delta M/M_0$)-E loop is symmetric with E, so the α_{max} shows a similar trend under positive and negative fields but different signs according to its definition. A maximum CME coefficient of 1.14×10^{-9} s/m is achieved at 500 Oe. Even if the CME coefficient value is not very high, these results clearly demonstrate the practicability of the strain-mediated CME coupling effect in ferromagnetic/antiferroelectric heterostructure.

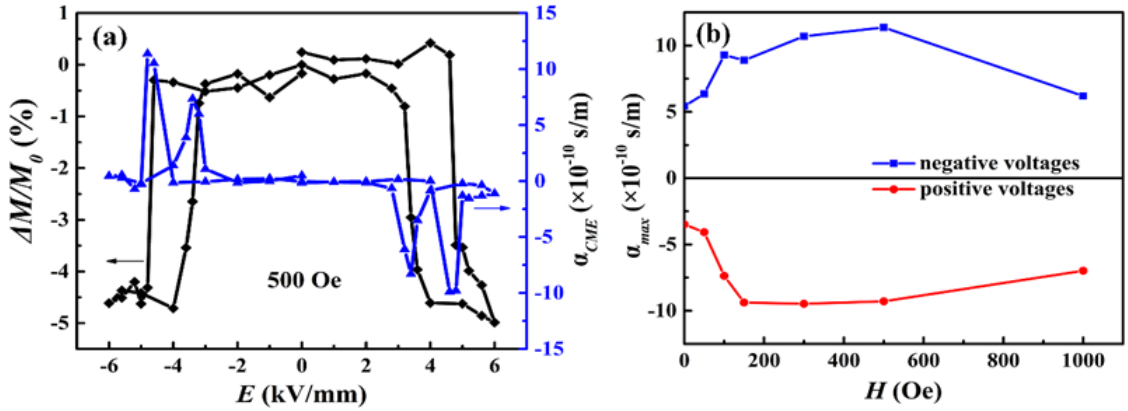

Figure 5.9 (a) $\Delta M/M_0$ and CME coefficient versus E under a bias magnetic field of 500 Oe, (b) the maximum of CME coefficient versus bias H under positive and negative voltages of NMG/PLZST/NMG sample.

5.4 Conclusions

In this part of the work, the in-plane CME effect and E-field controlled magnetization based on a composite consisting of NMG films and PLZST AFE ceramic have been investigated. It is remarkable that first, the evolution of ($\Delta M/M_0$) as a function of E is in good agreement with the ceramic strain evolution and secondly that the maximum $\Delta M/M_0$ variation, which attains a maximum value of 15%, is reached at 0 Oe (without bias magnetic field). The CME coefficient is small, probably due to the defects of NMG film on PLZST ceramic. Because there are inevitable grain gaps in ceramic substrates, many defects were observed in NMG film at the macroscale, and these defects influence the magnetic performance. Even though, these CME results also reveal the great potential of AFE materials in the ME coupling effect. It is the first time that the value of the CME coefficient is presented for an FM/AFE heterostructure.

6 CME Coupling Effect of YIG Films on AFE and FE Ceramics

Ferrite materials are an essential family of magnetic materials, and they are also widely used in ME coupling composites. Among them, YIG is considered as a good choice for the magnetic material when targeting tunable multiferroic microwave devices thanks to its outstanding advantages including small magnetocrystalline anisotropy, narrow ferromagnetic resonance linewidth, high resistivity, and low microwave losses. Therefore, many works are focused on magnetoelectric interactions of YIG/FE. Since YIG has preponderant advantages in ME composites, but the most work of YIG/FE composites is focused on *the E*-field controlled FMR shift, which is an indirect method to characterize the CME coupling effect. The most direct manifestation of the CME effect, the *E*-field controlled magnetization variations, is less studied. To understand the converse magnetoelectric (CME) coupling effect, it is necessary to study the electric-field tuning of magnetism of YIG at a static state.[126]

The study of *E*-field tuning of magnetism in YIG/AFE heterostructure has not been reported yet, to the best of the authors' knowledge. In this part, the ME composites of YIG/PLZST has been fabricated, and the in-plane and the out-of-plane voltage induced magnetism has been carried out. The YIG/PMN-PZT heterostructure has also been fabricated, and the *E*-field controlled magnetization switching and *E*-tunable susceptibility would be reported.

6.1 Preparation of YIG/AFE and YIG/FE Heterostructures

6.1.1 YIG film Growth

The YIG films were prepared by using a "Plassys" RF sputtering system with a YIG powder target. The sputtering condition and annealing process of YIG films have been explored by several researchers,[127–129] and in particular in the group. They have demonstrated that the post-annealing process has strong effects on the quality of YIG films. The details of the sputtering condition are given in Table 6.1.

Table 6.1 Sputtering parameters of YIG films

Sputtering Condition	YIG

Vacuum (Pa)	$< 3 \times 10^{-4}$
Power (W)	100
Temperature (℃)	RT
Atmosphere	Ar
Pressure (Pa)	1

After the deposition, the samples were annealed in a furnace to be crystallized. The reported crystallization temperature of the YIG film is 700~750 ℃. [127,128] The annealing process is given in Table 6.2. The YIG films were annealed at 700 and 750 ℃.

Table 6.2 Annealing parameters of YIG films

Annealing Condition	YIG
Heating Rate (℃/min)	2
Annealing (℃)	700, 750
Duration (min)	60
Cooling Rate (℃/min)	1
Atmosphere	Air

The YIG films were firstly deposited on SiO_2/Si substrates to check the sputtering condition and annealing process. Figure 6.1 shows the XRD patterns and magnetic hysteresis loops of YIG films on SiO_2/Si substrates with the different annealing process. From Fig. 6.1 (a), it can be observed that the YIG films cannot be crystallized on SiO_2/Si substrates when the annealing temperature is 700 ℃, but the crystallization can be achieved at 750 ℃. In Fig. 6.1 (b), the well-crystallized YIG film shows good magnetic properties. The high saturated magnetization (M_S =105 emu/cm^3) and low magnetic coercive field (H_C =43 Oe) can be reached in YIG films, which reveals the feasibility of the preparation process of YIG film.

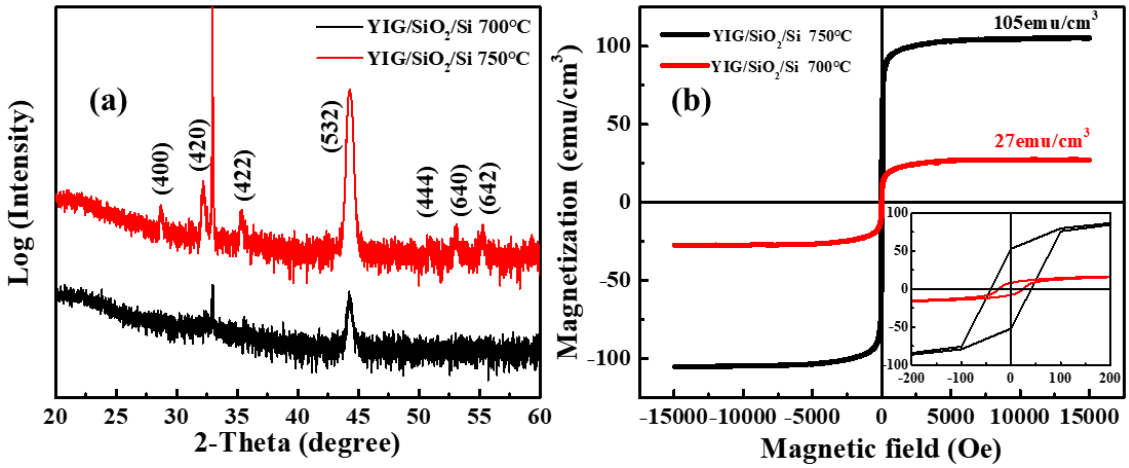

Figure 6.1 (a) The XRD patterns and (b) *M-H* loops of YIG films on SiO_2/Si substrates with different annealing temperatures.

6.1.2 Preparation of YIG/Pt/PLZST/Pt and YIG/Pt/PMN-PZT/Pt ME Heterostructures

The 2-2-type laminate composites consist of ferromagnetic films, and ceramic substrates can be simply prepared, and the high-resistance ferroelectric layer can effectively avoid the influence of leakage current when compared to other types of ME composites. Therefore, we choose this structure to prepare the ME composite structure.

Since YIG is an insulating material, the electrode layers are necessary for an application of the electric field. The multiferroic composites are designed to be a layered structure of YIG film and PLZST AFE and PMN-PZT FE ceramics with Pt electrodes as the interlayer. The Pt electrodes with good conductivity were deposited on both sides of PLZST and PMN-PZT ceramic with a thickness of 80nm by DC magnetron sputtering. The YIG films were deposited on Pt/PLZST/Pt and Pt/PMN-PZT/Pt structures by radio-frequency magnetron sputtering in a thickness of 400 nm. Concerning the thickness of the YIG film, the choice has been made according to previous studies. Lian *et al.* have investigated the effect of the YIG film thickness on the CME coupling.[126] The YIG film with a thickness of 400 nm has shown good CME coupling results, so we have decided to retain it for this study. The dimensions of the ceramic substrate are designed to be respectively 8 × 8 mm^2, while Pt electrodes and YIG film size are respectively restricted to be 6 × 6 mm^2 and 5 × 3 mm^2 by masks, as shown in Fig. 6.2.

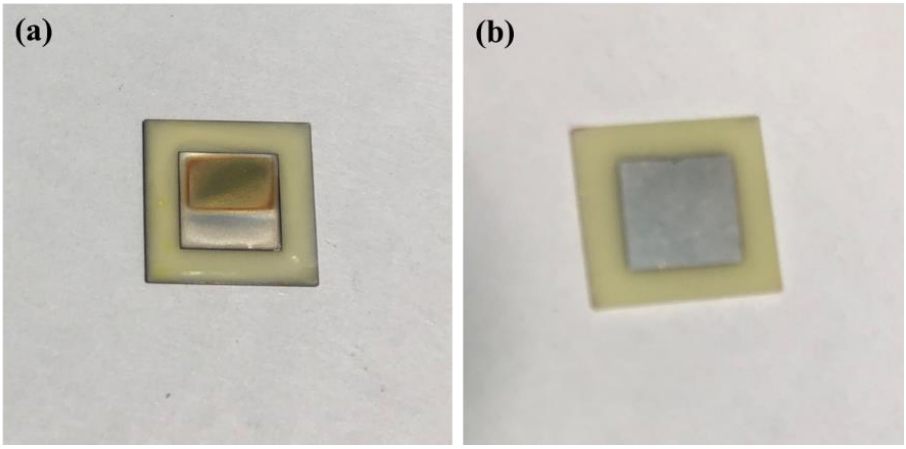

Figure 6.2 Schematic of YIG/Pt/PLZST (PMN-PZT)/Pt heterostructure (a) front side and (b) backside.

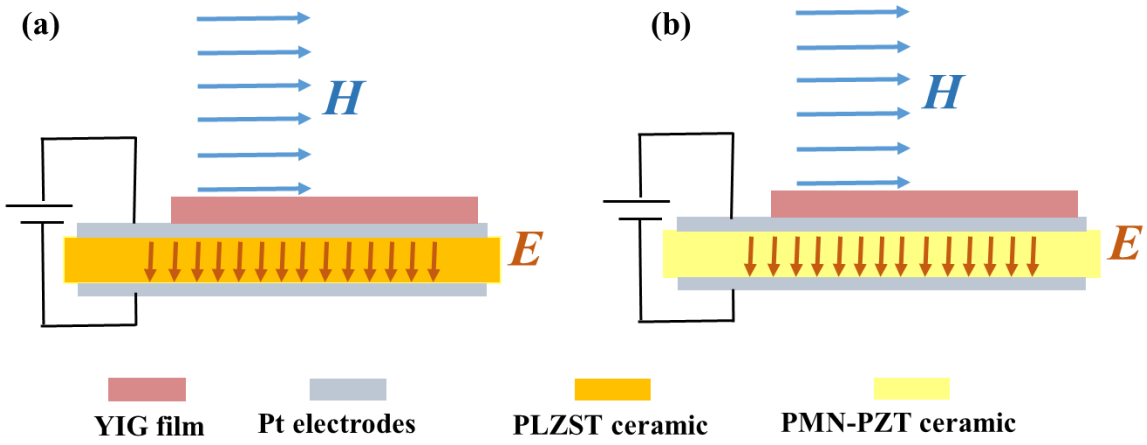

Figure 6.3 Schematic of (a) YIG/Pt/PLZST/Pt and (b) YIG/Pt/PMN-PZT/Pt ME heterostructures.

In order to apply the electric field, a soldering process was involved in connecting conductive wires with Pt electrodes. Thus the magnetic field and electric field can be applied to the sample simultaneously. Figure 6.3 illustrates the schematic of YIG/Pt/PLZST/Pt and YIG/Pt/PMN-PZT/Pt with the application of the electric and in-plane magnetic field.

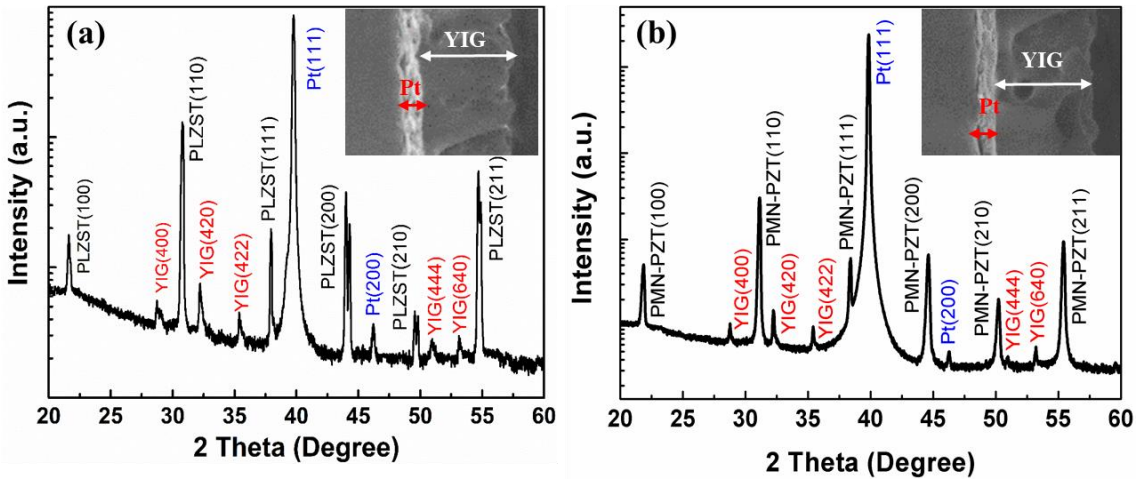

Figure 6.4 The XRD pattern and inset cross-sectional SEM image of (a) YIG/Pt/PLZST/Pt and (b) YIG/Pt/PMN-PZT/Pt heterostructures.

The phase structure and crystallization of YIG/Pt/PLZST/Pt and YIG/Pt/PMN-PZT/Pt laminate composites were confirmed by X-ray diffraction, and the cross-sectional morphology was characterized by SEM. Figure 6.4 depicts the XRD pattern and SEM image of YIG/Pt/PLZST/Pt and YIG/Pt/PMN-PZT/Pt heterostructures. The XRD analysis confirms the expected phase structures for all the materials. The origin of the various peaks is as labeled. Even though the diffraction peaks of YIG thin films are of much lower intensity when compared to the peaks of ceramic substrates and Pt electrodes, they are distinct enough, and all correspond to the pure YIG phase. The YIG films present a good crystallization in the desired phase of cubic $Y_3Fe_5O_{12}$ without any second phase. The cross-sectional SEM images demonstrate the clear interface of ceramic substrates, Pt electrodes, and YIG films, indicating no discernable diffusion happened.

6.2 YIG/Pt/PLZST/Pt heterostructure

6.2.1 In-plane CME Effect in YIG/Pt/PLZST/Pt Heterostructure

The YIG film being polycrystalline it demonstrates isotropic in-plane magnetic properties, thus the in-plane magnetic field direction is parallel to the substrate plane.

The in-plane *M-H* loop of YIG/Pt/PLZST/Pt heterostructure is shown in Fig. 6.5. The YIG film presents good magnetic properties on PLZST ceramic substrate, the same as YIG on PMN-PZT ceramic substrate. The values of the saturate magnetization (M_S),

remnant magnetization (M_r), coercive magnetic field (H_C) and magnetic susceptibility (χ) in YIG/Pt/PLZST/Pt are given in Table 6.3.

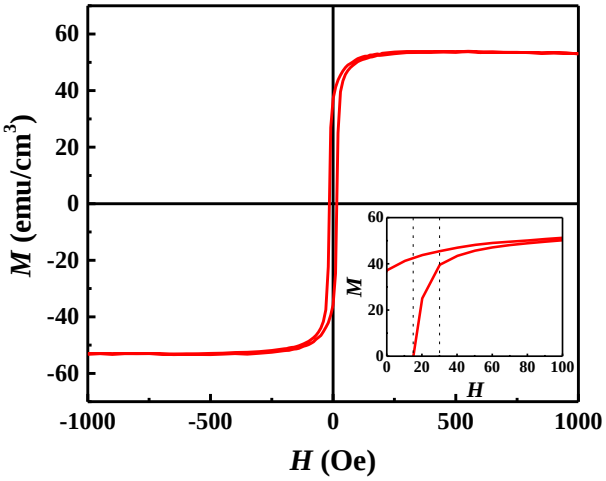

Figure 6.5 The in-plane *M-H* loops of YIG/Pt/PLZST/Pt heterostructure.

Table 6.3 The values of *Ms*, *Mr*, H_C, and χ of YIG/Pt/PLZST/Pt heterostructure.

Ms **(emu/cm^3)**	***Mr*** **(emu/cm^3)**	$\boldsymbol{H_C}$ **(Oe)**	$\boldsymbol{\chi}$
53.8	37.3	15	41

The *M-H* loops of YIG/Pt/PLZST/Pt heterostructure while an electric field is applied across the PLZST ceramic are measured in order to investigate the magnetoelectric coupling in a static electric state. The *M-H* loops with different electric fields and H_C-*E* curve are given in Fig. 6.6 (a) and (b). When the external electric field is lower than AFE-FE switching field of PLZST, the *M-H* loops coincide with the one without an electric field. Once the electric field is higher than the AFE-FE switching field, the remnant magnetization decreases sharply, and the *M-H* loops become difficult to be saturated. In this case, an induced magnetic coercive field shift is generated in response to the application of an electric field. The strain driven by the electric-field-induced AFE-FE phase transition is transferred through Pt electrode to YIG film, which leads to magnetic anisotropy transformation in the YIG film.

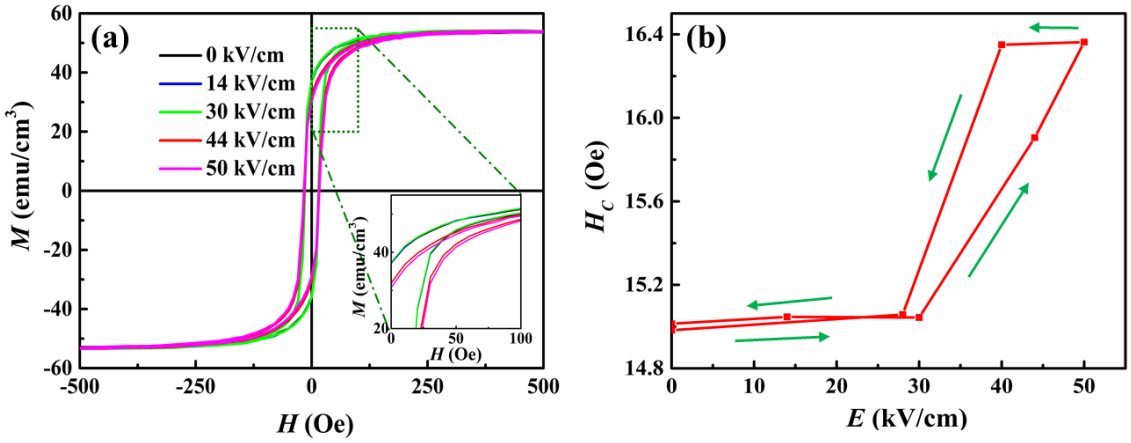

Figure 6.6 (a) *M-H* loops, inset the enlarged *M-H* loops, (b) H_C-*E* curve of YIG/Pt/PLZST/Pt heterostructure.

The χ-*H* curves with different electric fields are shown in Fig. 6.7 (a). All the χ reach maximums at 20 Oe, near H_C. To observe the influence of the electric field strength on the YIG film susceptibility at a given magnetic field, we show in Fig. 6.7 (b) the χ-*E* curve for a magnetic field of 10 Oe as a representative. It is noteworthy that the electric field facilitates a decrease in the susceptibility, which yields a maximum variation, as a function of the electric field, of $\Delta\chi$ = 13.5 at 10 Oe. The maximum relative χ change reaches $\Delta\chi/\chi_0$ = 33% at 10 Oe. This change of χ gives rise to the tunability of permeability and thus opens a pathway towards the design of voltage tunable inductor.

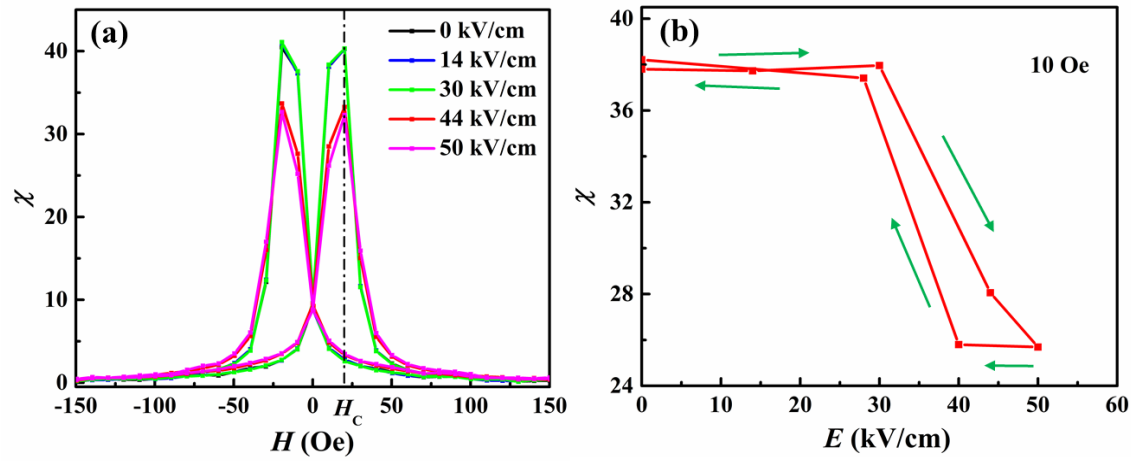

Figure 6.7 (a) χ-*H* curves with different electric fields and (b) χ-*E* curve at 10 Oe of YIG/Pt/PLZST/Pt heterostructure.

Additionally, the H_C-E and χ-E curves clearly display the familiar horn-like shape but in the opposite direction, which is attributed to the correlation between strain and electric field. The shape of H_C-E and χ-E curves demonstrate the effective control of magnetocrystalline anisotropy transformation by E-field via strain mediated mechanism.

In order to investigate the magnetoelectric coupling in a static magnetic state, the M-E curves were measured while applying an electric field across the PLZST ceramic. Before the measurements, the influences of the ceramic and the electrodes were excluded, and the YIG/Pt/PLZST/Pt heterostructure was fully magnetized at the same high bias magnetic field (2 T) to ensure the same initial state. The M-E curves under the bias magnetic field of 0, 15, and 30 Oe of YIG/Pt/PLZST/Pt heterostructure are given in Fig. 5.13. Under a specific magnetic field, the cycle for the change of the electric field is as follows: 0 → 54 → -54 → 0 kV/cm. The M-E curves were measured in two electrical cycles with a bias magnetic field of 0 Oe, while only one cycle for 15 and 30 Oe.

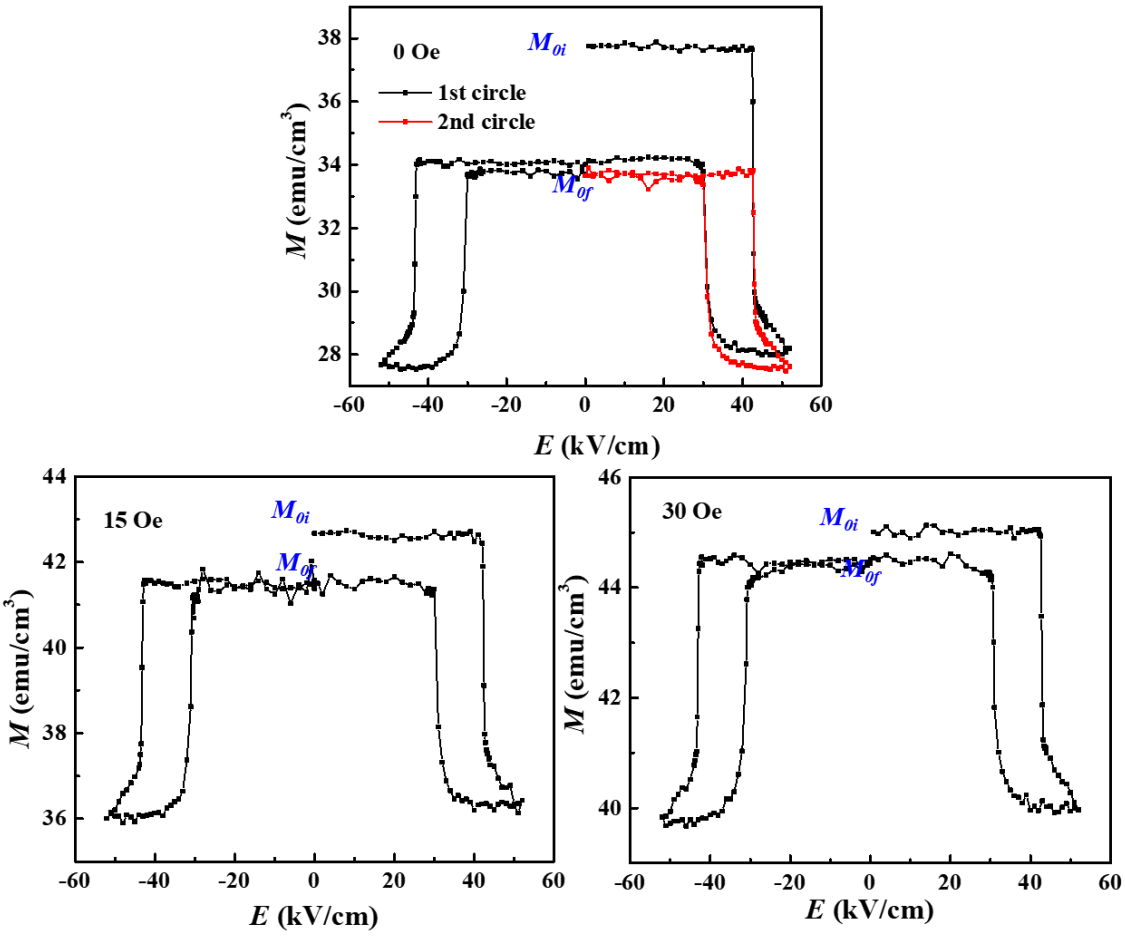

Figure 6.8 The *M*-*E* curves of YIG/Pt/PLZST/Pt at 0 Oe, 15 Oe, and 30 Oe. The labeled M_{0i} and M_{0f} are the initial magnetization and final magnetization at 0 kV/cm.

Figure 6.8 (a) presents two distinct effects. One is the reversible strain-driven magnetization change. The horn-like *M*-*E* curves show a similar shape to the *S*-*E* curve of PLZST in Fig. 4.10, demonstrating the magnetization variations are strongly induced electro-strain originated from PLZST ceramic. A second effect appears which also induces a change in the magnetization, that is, the difference of the magnetization between the initial state (M_{0i}), at the beginning of the measurements, and the magnetization state at the end of the first electrical cycle (M_{0f}). Since the YIG/Pt/PLZST/Pt heterostructure was fully magnetized at 2 T before the measurements, the magnetic domains of YIG film are highly aligned to one direction. The value of M_{0i} is, of course, in relation to bias *H* applied to the YIG film during the measurement. For example, in Fig. 6.8 (H = 0 Oe), M_{0i} associated is 37.8 emu/cm^3, while M_{0i} equals to 45.2 emu/cm^3 in Fig. 6.8 (H = 30 Oe). This difference of (M_{0i}-M_{0f}) is due to the irreversible demagnetization effect induced by the strain. The strain can easily destroy the alignment of well-ordered magnetic domains and favors to rotate magnetic moments toward the opposite direction. However, when the strain is removed, not all the magnetic domains can recover to its initial state. The unrecoverable part leads to the difference of (M_{0i}-M_{0f}). Thus the difference of (M_{0i}-M_{0f}) only exists in the first half electrical cycle of measurement.

As the bias magnetic field decreases, the ratio of the strain-controlled magnetization change ($\Delta M/M_{0f}$) as a function of the bias magnetic field is shown in Fig. 6.9 (a). It can be seen that $\Delta M/M_{0f}$ gradually decreases with the increase of the applied bias magnetic field, and there is a maximum value of 17.5% at the zero magnetic fields. This phenomenon indicates that the influence of electric field induced strain on YIG film is maximized when the bias magnetic field is 0 Oe, which is of great significance for the development of future magnetoelectric devices. In contrast, in the high magnetic field (30 Oe), the mechanical deformation of ceramics has a relatively limited regulation of the magnetization of YIG films, with only 11% of the magnetization changes. The ratio (M_{0i}-M_{0f})/ M_{0f} depends on the magnetic state of the YIG film. This ratio, as shown in Fig. 6.9 (b), gets its maximum at 0 Oe and then decreases quickly, as a function of *H*.

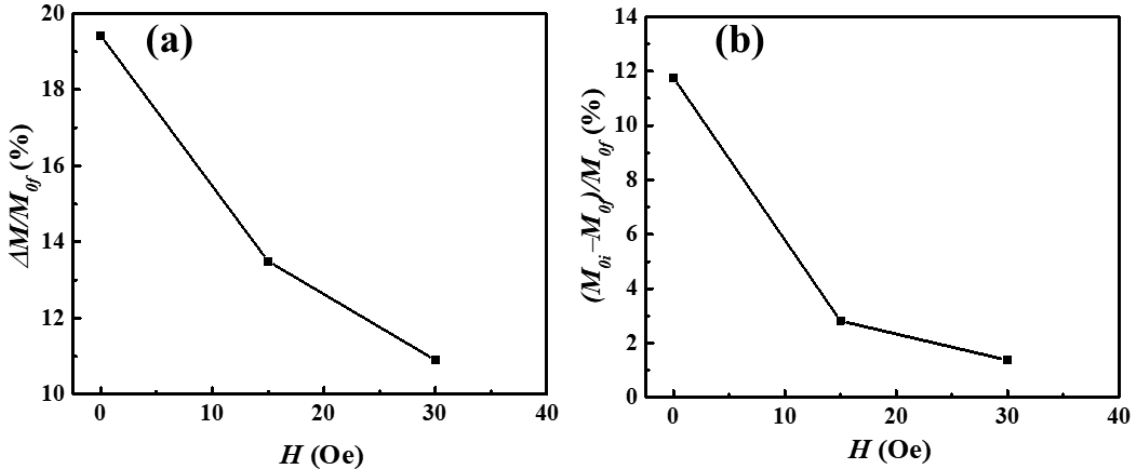

Figure 6.9 (a) The relative magnetization change versus magnetic field ($\Delta M/M_{0f}-H$) curve, (b) (M_{0i}-M_{0f})/$M_{0f}-H$ curve of YIG/Pt/PLZST/Pt heterostructure.

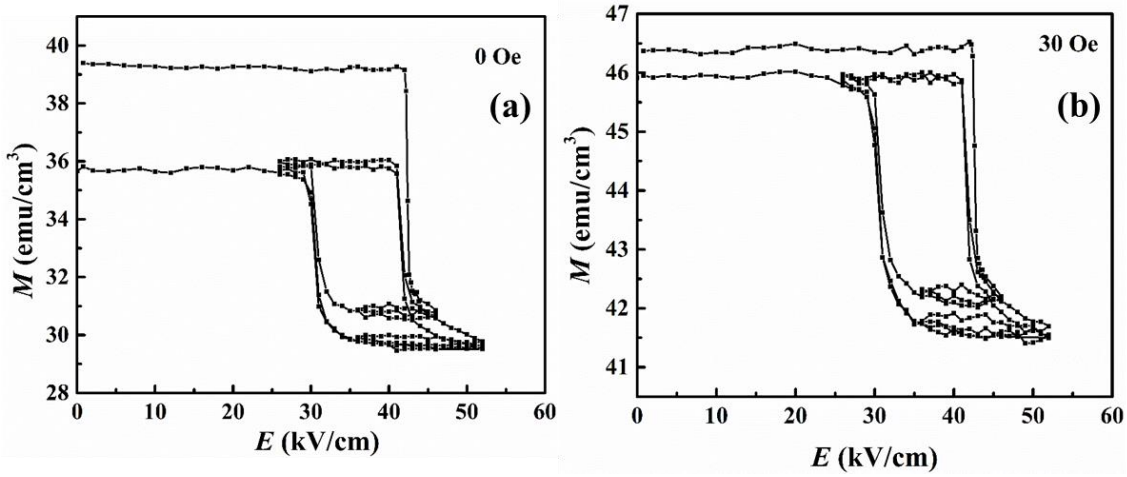

Figure 6.10 The magnetization versus electric field curves of YIG/Pt/PLZST/Pt (a) 0 Oe, (b) 30 Oe.

How would the magnetization of YIG/Pt/PLZST/Pt change if the magnitude of the applied electric field is randomly changed? We have measured *M* of YIG/Pt/PLZST/Pt heterostructure while applying a random electric cycle across the PLZST ceramic at 0 and 30 Oe, as shown in Fig. 6.10. The electric field we applied to the PLZST ceramic is as follows: 0 → 46 → 36 → 46 → 26 → 52 → 36 → 52 → 26 → 52 → 0 kV/cm. Again, YIG/Pt/PLZST/Pt heterostructure was fully magnetized under the same high bias magnetic field (2 T) prior to measurements to ensure the same initial state. It can be seen that the magnetization variations still follow the horn-like *M*-*E* curves, as given

in Fig. 6.10. Also, the difference of (M_{0i}-M_{0f}) also exists when the first half electrical cycle is loaded.

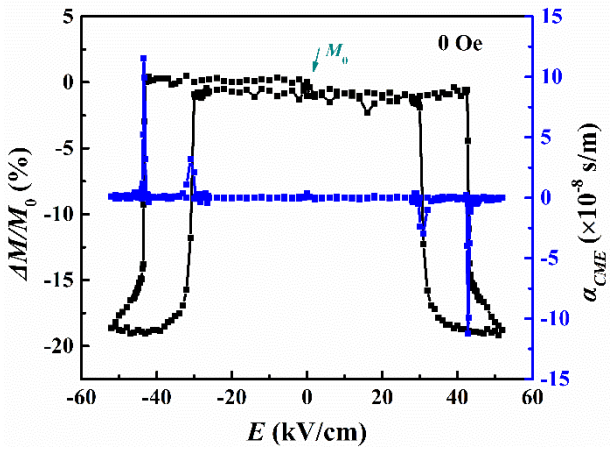

Figure 6.11 $\Delta M/M_0$-E and α_{CME}-E curves at 0 Oe of YIG/Pt/PLZST/Pt heterostructure.

The CME coefficient (α_{CME}), calculated from the equation: $\alpha_{CME} = \mu_0 \delta M/\delta E$ ($\mu_0 = 4\pi\times10^{-7}$ H/m), is also given in Fig. 6.11. It is observed that, because of the sharp strain change, the α_{CME} peaks at four phase transition switching fields. The maximum value recorded is 11.6 × 10^{-8} s/m.

The maximums of α_{CME} for three different bias magnetic fields (0, 15, 30 Oe) are reported in Fig. 6.12. The α_{CME} decreases with a bias magnetic field increasing, and the largest value of α_{CME} is obtained with a bias magnetic field of 0 Oe. The fact that the best performance of CME coupling is obtained without the magnetic field is a really important asset in terms of design when targeting ME devices conception.

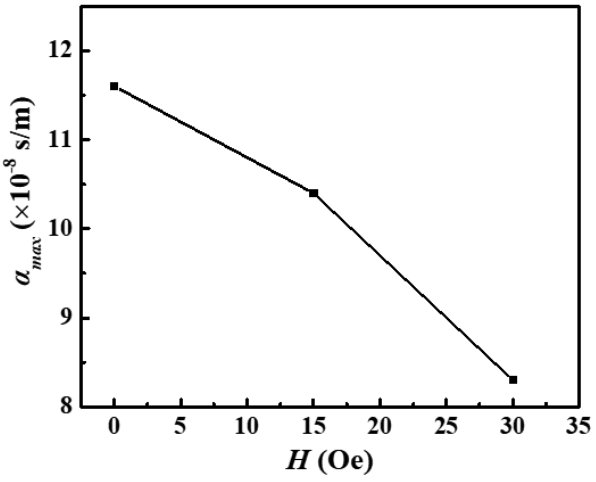

Figure 6.12 The CME coefficient versus bias magnetic field curves of YIG/Pt/PLZST/Pt heterostructure.

Table 6.4 Summary of magnetoelectric coupling parameters for some laminated structures.

Structure	α_{CME} ($\times 10^{-8}$ s/m)	$\Delta M/M$	*bias H* (Oe)	$\Delta\chi/\chi_0$
YIG/PLZST (this work)	11.6	17.4%	0	32.7% @10 Oe
YIG/PMN-PZT[130]	10.9	7%	40	16.8% @30 Oe
LSMO/PMN-PT(001)[111]	6	25%	100	-
CFO/PMN-PT(001)[131]	3.2	6%	500	-
CFB/ PMN-PT(001)[132]	200	17.6%	5	-

For comparison purposes, Table 6.4 summarizes important results measured at a static magnetic state for different layered structures recently reported. In review, we observe that the AFE-based structure reported here demonstrates the first reported CME coefficient and relative susceptibility change for ME heterostructures. Further, this CME coefficient is obtained without the application of bias magnetic field, which is a strong asset in terms of cost and ease of procedures. The high relative susceptibility change reveals a potential opportunity of AFE materials to develop future ME tunable devices.

6.2.2 Out-of-plane CME Effect in YIG/Pt/PLZST/Pt Heterostructure

In order to fully understand the CME Effect in YIG/Pt/PLZST/Pt heterostructure, the out-of-plane *E*-field induced magnetism was also carried out. For these measurements, the magnetic field is vertically applied to the YIG/Pt/PLZST/Pt heterostructure.

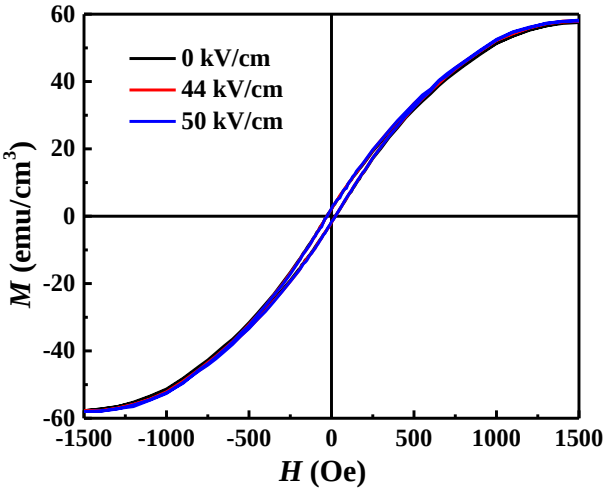

Figure 6.13 The out-of-plane *M-H* loops of YIG/Pt/PLZST/Pt heterostructure with different electric fields.

The electric-field dependence of out-of-plane *M-H* loops of YIG/Pt/PLZST/Pt heterostructure are illustrated in Fig. 6.13. It can also be observed that the out-of-plane saturate magnetic field of YIG film is much higher than in-plane results. The YIG polycrystalline film has an "easy plane" on the PLZST substrate plane that more energy is needed for YIG film to be saturated along out-of-plane direction. Under an application of electric field, the *M-H* loops weakly varies with the electric-field-induced strain.

The out-of-plane magnetization change as a function of the electric field at 500 and 1000 Oe in YIG/Pt/PLZST/Pt heterostructure are given in Fig. 6.14. The horn-like shape of *M-E* curves can be clearly observed, even the strain-induced magnetic variations are small. The out-of-plane strain favors the magnetization process. With the bias magnetic field increasing, the strain-induced magnetization effect is also hindered by the bias magnetic field.

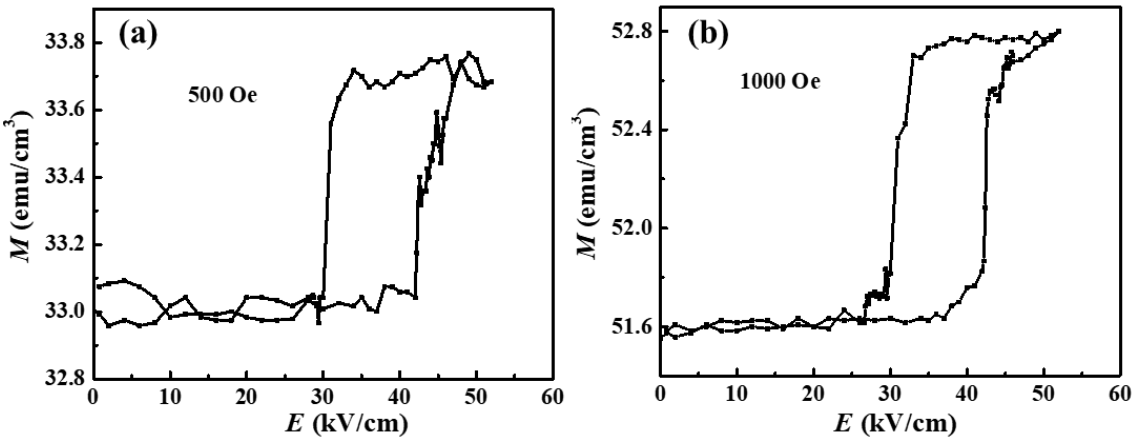

Figure 6.14 The out-of-plane *M-E* curves of YIG/Pt/PLZST/Pt heterostructure (a) 500 Oe, (b) 1000 Oe.

The in-plane and out-of-plane *M-E* curves of YIG/Pt/PLZST/Pt heterostructure are given in Fig. 6.15. The out-of-plane strain favors the magnetization process, while in-plane strain leads to the demagnetization process. The electric field induced in-plane magnetization variations are much larger than out-of-plane ones. These differences can also be explained by the strain-induced magnetic domain motion is hindered in thickness-direction due to its low dimension. However, large strain-induced magnetic variation can be achieved because of its large dimension in width- and length-direction.

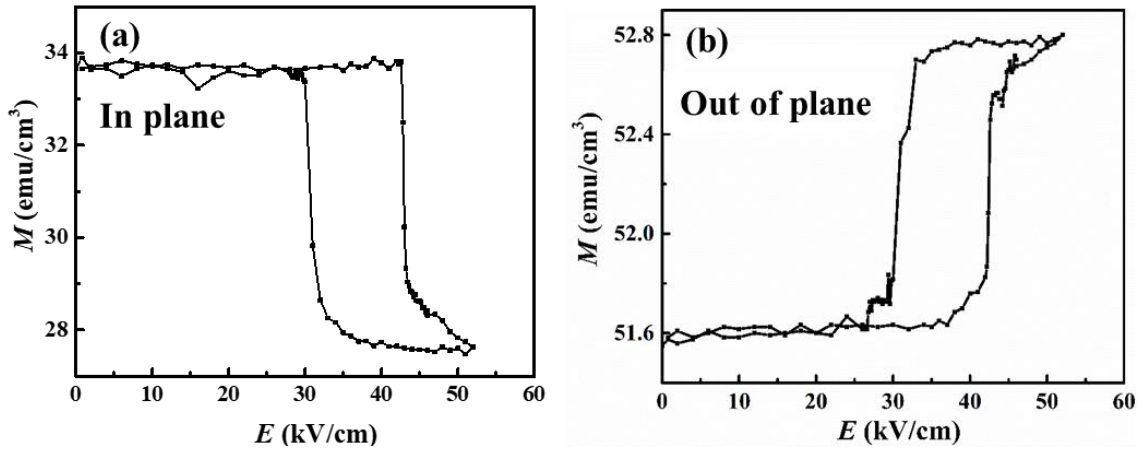

Figure 6.15 (a) The in-plane *M-E* curve and (b) out-of-plane *M-E* curve of YIG/Pt/PLZST/Pt heterostructure.

The schematic of the anisotropy axis change with the electric field in YIG/Pt/PLZST/Pt heterostructure can be illustrated in Fig. 6.16. When the electric field

is applied to PLZST ceramic, the strain will lead the anisotropy axis to tilt to the out-of-plane direction. Thus the in-plane magnetization (M_x) reduces, and out-of-plane magnetization (M_z) increases.

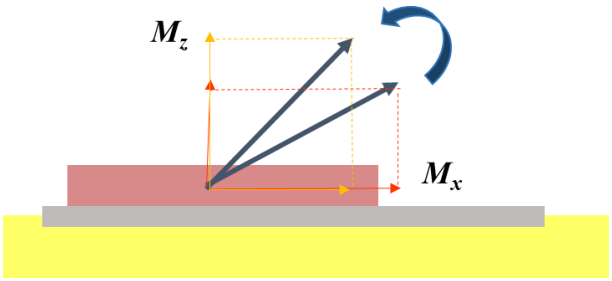

Figure 6.16 Schematic of the veer of the anisotropy axis in YIG film.

6.2.3 Summary

In summary, the *E*-field controlled magnetism in an AFE-based multiferroic heterostructure of YIG/PLZST is reported. A comprehensive study of in-plane magnetization, coercive magnetic field, magnetic susceptibility, and CME coefficient response to an electric field is achieved in this part. The electric field induced phase transition strain in AFE substrate plays a crucial role in ME coupling, and its unique zero-remnant state gives us extra advantages to avoid the pre-poling process. The maximum in-plane α_{CME} is 11.6 × 10^{-8} s/m without a magnetic field, and the in-plane $\Delta\chi/\chi_0$ can reach 33% with a low magnetic field of 10 Oe. The large susceptibility variation possibility given by this composite, YIG/Pt/PLZST/Pt, shows great potential for ME tunable devices. This *E*-field control of magnetism is originated from the *E*-field induced magnetic anisotropy change. The tensile out-of-plane strain generated in PLZST ceramic leads the magnetic anisotropy of YIG film to tilt to out-of-plane direction, thus results in in-plane demagnetization and out-of-plane magnetization effect with an application of the electric field.

6.3 YIG/Pt/PMN-PZT/Pt heterostructure

The YIG/FE heterostructures have been intensively studied in the past years, and various systems have been developed. In this part, the CME coupling effect of YIG/Pt/PMN-PZT/Pt was studied as a primary objective to compare the FE-based ME

coupling effect with Chapter 6.2. The in-plane and out-of-plane CME coupling effect would be discussed in YIG/Pt/PMN-PZT/Pt heterostructure.

6.3.1 In-plane CME Effect in YIG/Pt/PMN-PZT/Pt heterostructure

For these results, the applied magnetic field is parallel to the YIG/Pt/PMN-PZT/Pt plane.

Figure 6.17 shows the *M-H* loops of YIG/Pt/PMN-PZT/Pt heterostructure. As mentioned before, the YIG film on PMN-PZT ceramic is polycrystalline, indicating that the YIG film is isotropic in the plane. Good magnetic properties of YIG film can be obtained on PMN-PZT ceramic substrate, where the M_S, M_r, H_C, and χ are given in Table 6.5. The YIG films on PLZST and PMN-PZT are prepared by the same process, but the values in Table 6.5 are not close to the ones in Table 6.3. It can be explained by the differences of the ceramic substrates. Since the ceramic is a complex polycrystalline system and has many intrinsic holes, every piece of ceramic can be different. Even all the ceramic substrates are polished into an average roughness of several nanometers, the big grain gaps also exist. Also, they would affect the magnetic properties of YIG films and maybe the CME coefficient.

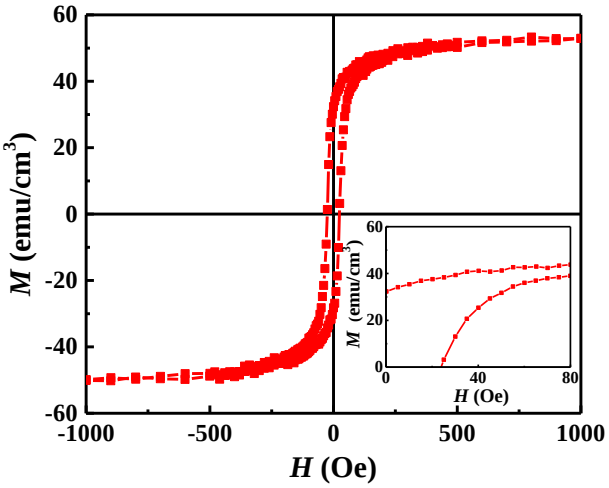

Figure 6.17 The normal and inset the enlarged *M-H* loop of YIG/Pt/PMN-PZT/Pt heterostructure.

Table 6.5 The magnetic properties of YIG/Pt/PMN-PZT/Pt heterostructure.

Ms **(emu/cm^3)**	***Mr*** **(emu/cm^3)**	***H$_C$*** **(Oe)**	χ

53.0	32.3	24.5	30

The electric-field dependence of in-plane *M-H* loops of YIG/Pt/PMN-PZT/Pt heterostructure are illustrated in Fig. 6.18 (a). Under an application of the electric field, the shape of *M-H* loops varies with the electric-field-induced strain. Since the PMN-PZT reaches the maximum tensile in-plane strain at $E = E_C$ and the maximum compressive in-plane strain at $E = E_{max}$, the *M-H* loops of YIG/Pt/PMN-PZT/Pt at an electric field of -4 kV/cm and 12 kV/cm are given as representatives. It can be seen that the compressive in-plane strain tends to upright *M-H* loops, while tensile in-plane strain tends to slanted *M-H* loops, revealing the strain-mediated transformation of magnetic anisotropy. The inset also reveals that the electric-field-controlled magnetization variations are more remarkable at low magnetic fields (0 ~ 300 Oe).

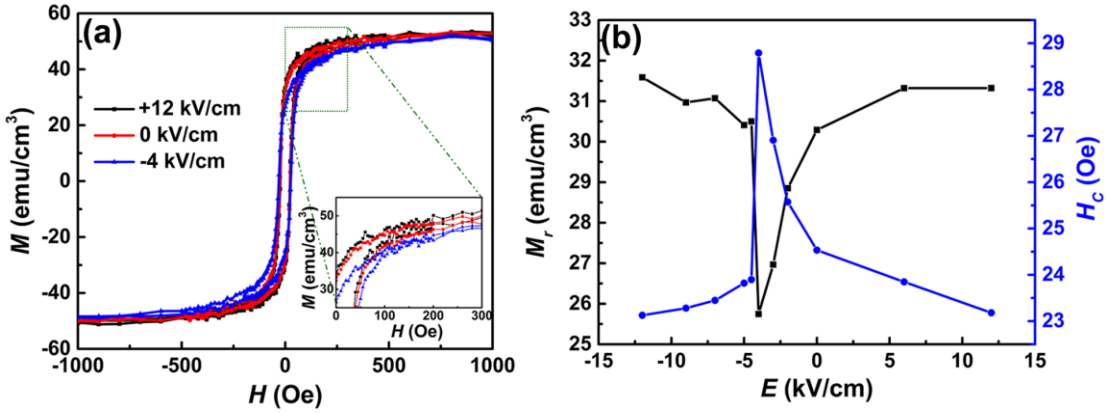

Figure 6.18 (a) *M-H* loops with different electric fields, inset the enlarged *M-H* loops, (b) M_r-*E* and H_C-*E* curves of YIG/Pt/PMN-PZT/Pt heterostructure.

As shown in Fig. 6.18 (b), the M_r and H_C change as a function of the applied electric field. The sharp rise of strain at $E = E_C$ results in the large jump in magnetization at an electric field of -4 kV/cm, and the H_C shifts up to 28.8 Oe. Additionally, the M_r-*E* and H_C-*E* curves of YIG/Pt/PMN-PZT/Pt heterostructure present similar butterfly shape to the *S-E* curve of PMN-PZT ceramic, which is attributed to the correlation between strain and electric field.

The change of *M-H* loops under electric fields refers to a shift of magnetic susceptibility (χ) manipulated by the electric field. Figure 6.19 (a) presents the χ-*H* curves under electric fields of -4, 0 and 12 kV/cm in YIG/Pt/PMN-PZT/Pt heterostructure. Under a specific electric field, the χ reaches the maximum at H_C. The

H_C varies with electric fields, thus the *E*-field controlled χ peaks at different magnetic fields (20 ~30 Oe). Under a specific magnetic field of 15, 20 and 25 Oe, the *E*-field controlled χ variations are given in Fig. 6.6 (b). At 20 Oe, it can be seen that the χ changes dramatically with the external electric field, being 33.6 at 12 kV/cm, 27.6 at zero fields and 15.5 at the coercive electric field. This equals a large tunable susceptibility $\Delta\chi$ = 18.1 and $\Delta\chi/\chi_0$ =65.6% under a low magnetic field of 20 Oe, implying great potential in ME tunable devices. When the magnetic field is 15 Oe or 25 Oe, the tunable susceptibility $\Delta\chi/\chi_0$ can reach 80.4% and 28.5%, respectively.

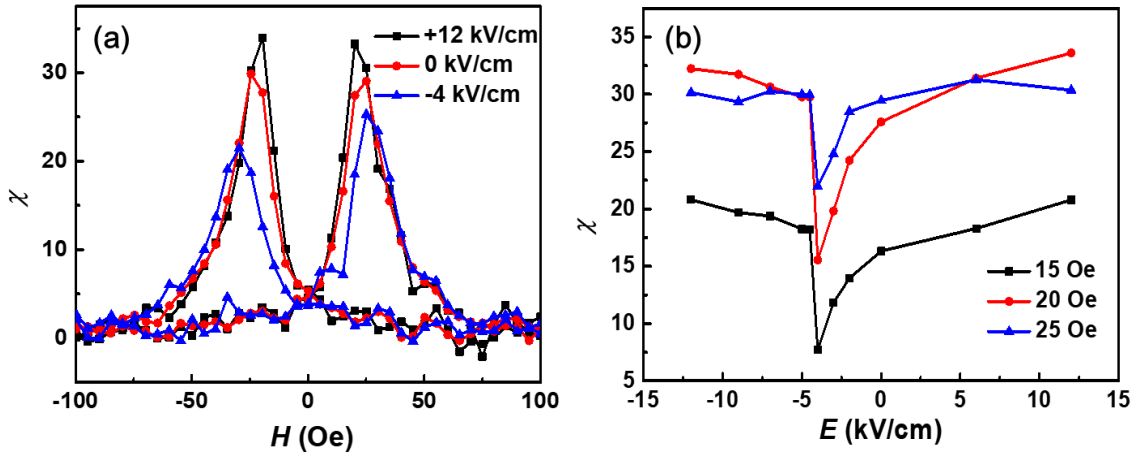

Figure 6.19 (a) χ-*H* curves with different electric fields and (b) χ-*E* curve at 15, 20, and 25 Oe of YIG/Pt/PMN-PZT/Pt heterostructure.

As mentioned in Chapter 6.2.1, the YIG/Pt/PLZST/Pt heterostructure was fully magnetized at the same high bias magnetic field (2 T) to ensure the same initial state. Since PMN-PZT is a ferroelectric material, it presents remnant state after an application of the electric field. To eliminate the influence of electrical history, the application of an electric field cycle starts from a value of +12 kV/cm to conform to the strain and polarization states of PMN-PZT. The change of the electric field is as follows: +12 → -12 → +12 → 0 kV/cm. Then the second cycle of the electric field can be applied as: 0 → -12 → +12 → 0 kV/cm. Figure 6.20 shows the first and second cycles of *M*-*E* curves with a bias magnetic field of 0 Oe as a representative. The difference of the magnetization between M_{0i} and M_{0f} exists in the first cycle of *the M*-*E* curve, which is due to the irreversible demagnetization of the previous "poling process" of YIG film. The first cycle of *the M*-*E* curve is measured from a high positive electric field of +12 kV/cm, so the curve is affected by this measurement process and presents in an

asymmetric butterfly-like shape. After the first cycle of *M-E* measurement, the electrical and magnetic load history can be removed. Then the second cycle of *M-E* measurement can be carried out to fully reveal the CME coupling effect in YIG/Pt/PMN-PZT.

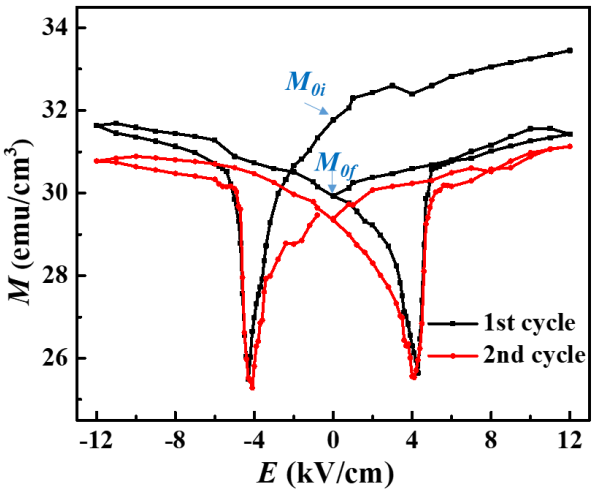

Figure 6.20 The first and second cycle of *M-E* curves at 0 Oe in YIG/Pt/PMN-PZT/Pt heterostructure.

The magnetization change as a function of the electric field in YIG/Pt/PMN-PZT/Pt heterostructure is given in Fig. 6.21. The butterfly-like shape of *M-E* curves resemble the *S-E* curves of PMN-PZT ceramic, which once again confirms that the change of magnetization in YIG film results from *E*-induced strain in the PMN-PZT ceramic. The compressive in-plane strain favors the magnetization process, while tensile in-plane strain leads to the demagnetization process. If the bias magnetic field is zero, the strain can easily control the magnetic response by destroying the alignment of well-ordered magnetic domains and rotating magnetic moments toward other directions. With the bias magnetic field increasing, the strain-induced magnetization or demagnetization process can be hindered by the bias magnetic field. Thus when the bias magnetic field is high enough (for example, 500 Oe), the strain-induced magnetization change can be entirely suppressed by a bias magnetic field induced magnetization process, and the strain-induced magnetization change becomes nearly zero, as shown in Fig. 6.21.

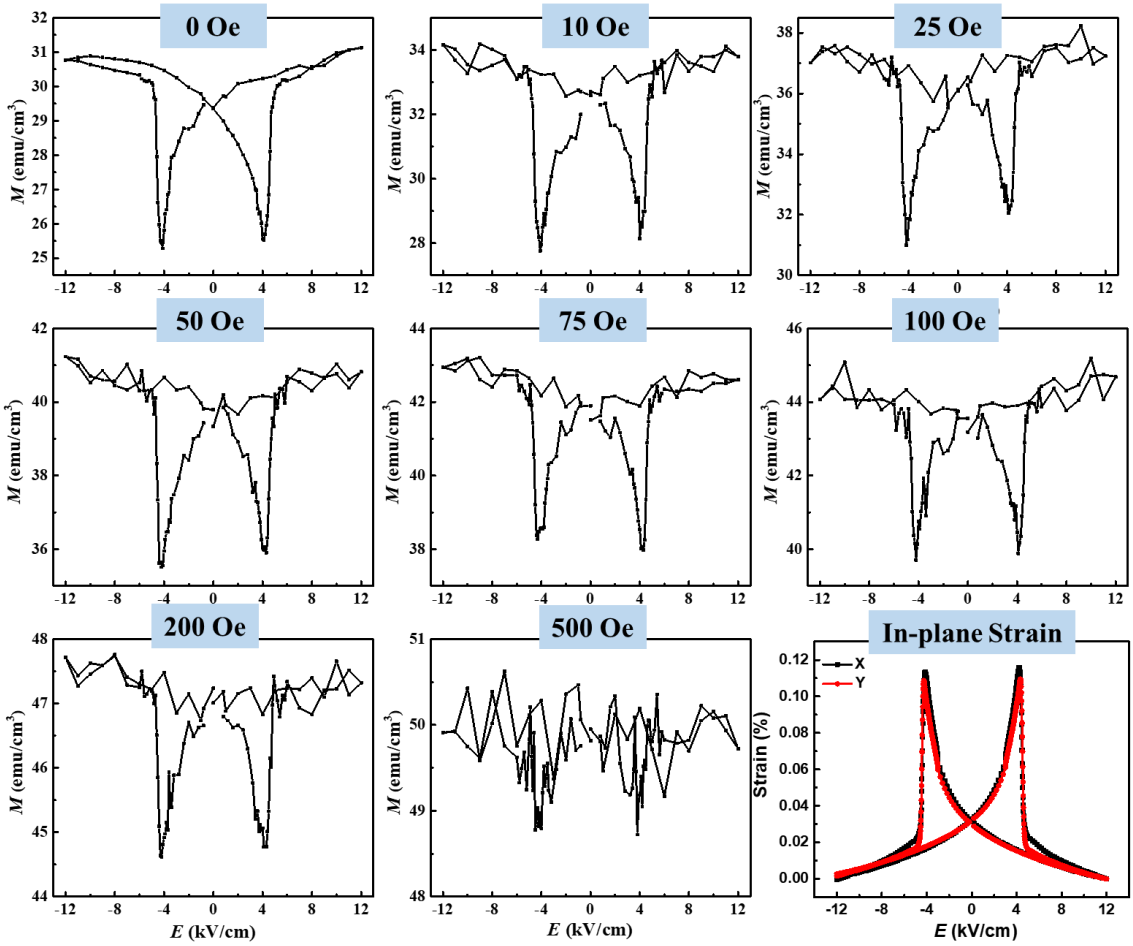

Figure 6.21 The electric-field-dependent magnetization (*M*-*E*) in YIG/Pt/PMN-PZT/Pt under the bias magnetic field of 0, 10, 25, 50, 75, 100, 200 and 500 Oe

In order to characterize it, the magnetization difference (ΔM) is defined as $\Delta M=M_E-M_0$, where M_E is the magnetization for E and M_0 is the magnetization without an electric field. Thus, the relative magnetization changes ($\Delta M/M_0$) versus E curves at 0 Oe is illustrated in Fig. 6.22(a) as representative. The converse ME coupling coefficient can be calculated by using the equation: $\alpha_{CME}=\mu_0\delta M/\delta E$ ($\mu_0=4\pi\times10^{-7}$ H/m). The CME coefficient (α_{CME}) as a function of the electric field at 0 Oe of YIG/Pt/PMN-PZT/Pt heterostructure is also given in Fig. 6.22 (a). The large tensile in-plane strain at E_C facilitates a sharp reduction in magnetization, which yields a maximum of $\Delta M/M_0$ and peaks of α_{CME}. As a consequence, the α_{CME} reaches a large value of 16.95 × 10^{-8} s/m in the absence of a bias magnetic field at a low electric field of 4.2 kV/cm. Thus these results make it possible to achieve a strong ME effect under a small electric field and zero magnetic field that promotes the realization of power-efficient ME devices.

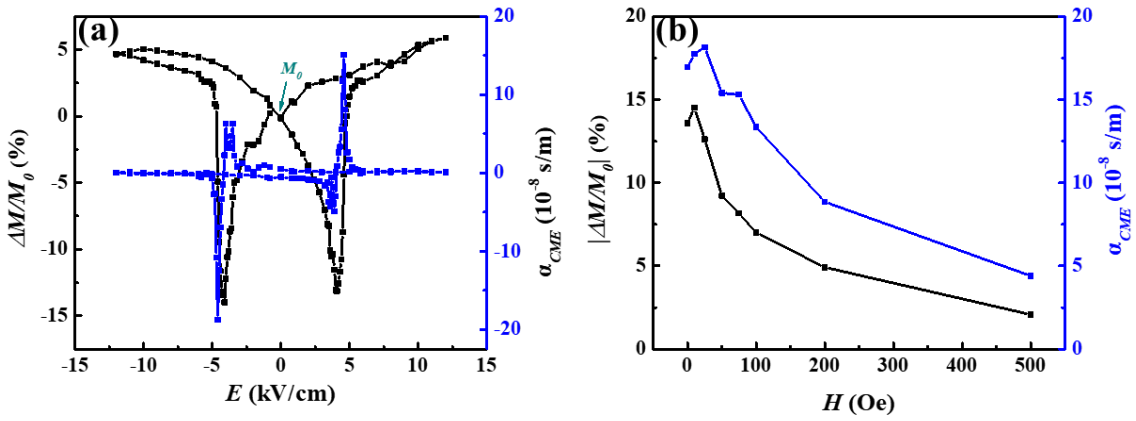

Figure 6.22 (a) $\Delta M/M_0$-E and α_{CME}-E curves at 0 Oe, and (b) $|\Delta M/M_0|$ -H and (α_{CME}) -H curves of YIG/Pt/PMN-PZT/Pt heterostructure.

The $|\Delta M/M_0|$ and α_{CME} as a function of bias magnetic field are presented in Fig. 6.22 (b). The $|\Delta M/M_0|$ and α_{CME} are respectively the peak values of the electric-field-induced magnetization reduction and CME coefficient under a specific magnetic field. The $|\Delta M/M_0|$ and α_{CME} firstly rise then decline with a bias magnetic field increasing. The maximum of $|\Delta M/M_0|$ is reached at 10 Oe, while the maximum of α_{CME} (18.15×10^{-8} s/m) appears at 25 Oe. The H_C of YIG film on PMN-PZT ceramic is around 25 Oe, where the magnetization can be easily switched. Thus the α_{CME} reaches the peak at this point, which is probably attributed to the easy magnetization switching at H_C. When the bias magnetic field is higher than H_C, the electric-field-induced demagnetization process is hindered by a large bias magnetic field that results in a low CME coefficient.

Since the E-induced strain plays a critical role in the ME coupling effect, the out-of-plane S-E curves of PMN-PZT ceramic measured by cycling electric field with different amplitudes are depicted in Fig. 6.23. The in-plane strain should show a similar evolution as the out-of-plane strain. When the amplitude of E is much higher than E_C, a whole butterfly-like curve appeared because of complete ferroelectric domain switching. While $E \leq E_C$, the shuttle-like curve was observed due to incomplete ferroelectric domain switching, which results in large remnant strain. Thus, two different strain states are generated when $E \leq E_C$, leading to two magnetization states in YIG film.

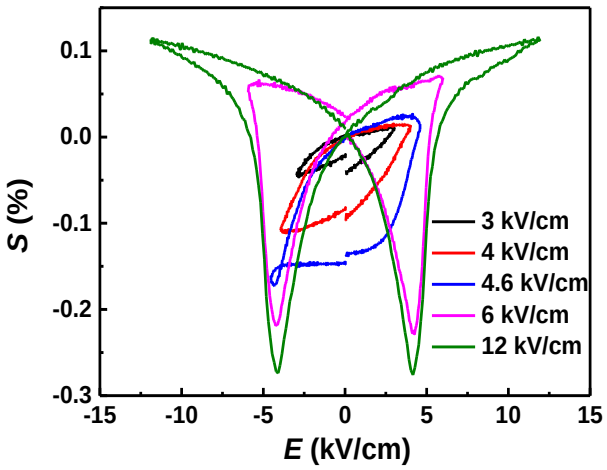

Figure 6.23 The out-of-plane strain evolution of PMN-PZT ceramic substrate.

According to the strain evolution, the *M*-*E* curves of YIG/Pt/PMN-PZT/Pt heterostructure under cycling electric field with different amplitudes at 0 Oe are given in Fig. 6.24. To remove the influence of electric load history, the YIG/Pt/PMN-PZT/Pt heterostructure was firstly poled at an electric field of 12 kV/cm for 3 min; then the *M*-*E* measurements were carried out. When the amplitudes of the electric field are lower than or around E_C, as shown in Fig. 6.24 (a), the shuttle-like *M*-*E* curves can be observed, which is consistent with those observed *S*-*E* curves. The direction of the inclination is *E*+. With the amplitude increasing, the shape of *M*-*E* curves switched into butterfly-like ones, and these butterfly-like *M*-*E* curves are also inclined to *E*+. The two different types of *M*-*E* curves reveal possibilities to prepare and utilize the ME composites with the low electric field. The shuttle-like *M*-*E* curves can provide two remnant magnetization states that are important to develop non-volatile CME memory devices.

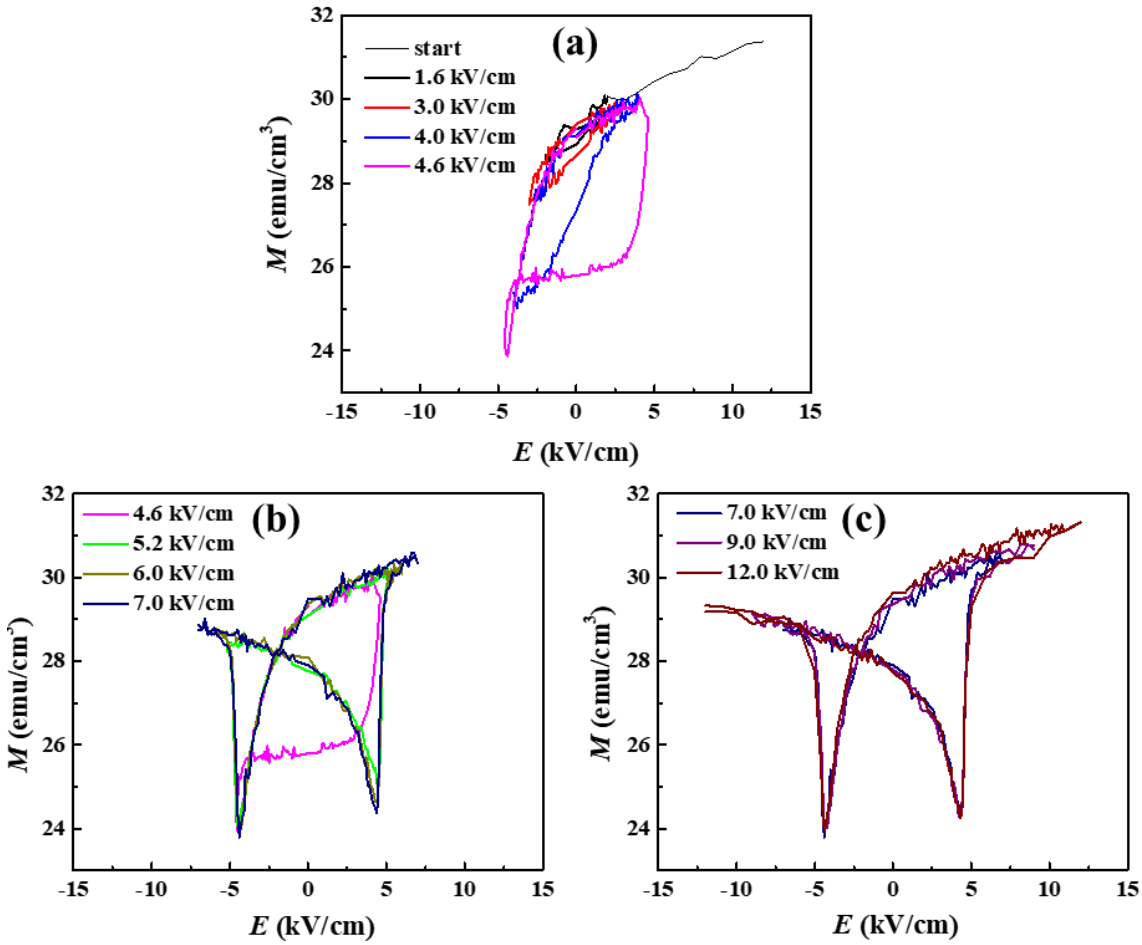

Figure 6.24 *M-E* curves of YIG/Pt/PMN-PZT/Pt heterostructure under cycling electric field with different amplitudes at 0 Oe. (a) *M-E* curves at 1.6, 3.0, 4.0, 4.6 kV/cm, (b) 4.6, 5.2 6.0, 7.0 kV/cm, (c) 7.0, 9.0, 12 kV/cm.

The *M-E* curves of YIG/Pt/PMN-PZT/Pt heterostructure are asymmetric, and there is a slope. To remove the influence of electric load history, the YIG/Pt/PMN-PZT/Pt heterostructure should be poled before the measurements. If it was poled at an electric field of +12 kV/cm for 3min, then the *M-E* curves would incline to *E*+, as shown in Fig. 6.25 (a). In Fig. 6.25 (b), the *M-E* curves would incline to *E*- when the YIG/Pt/PMN-PZT/Pt heterostructure was poled at an electric field of -12 kV/cm first. Thus, the inclined direction of asymmetric *M-E* curves is depended on the electric field history before the measurements.

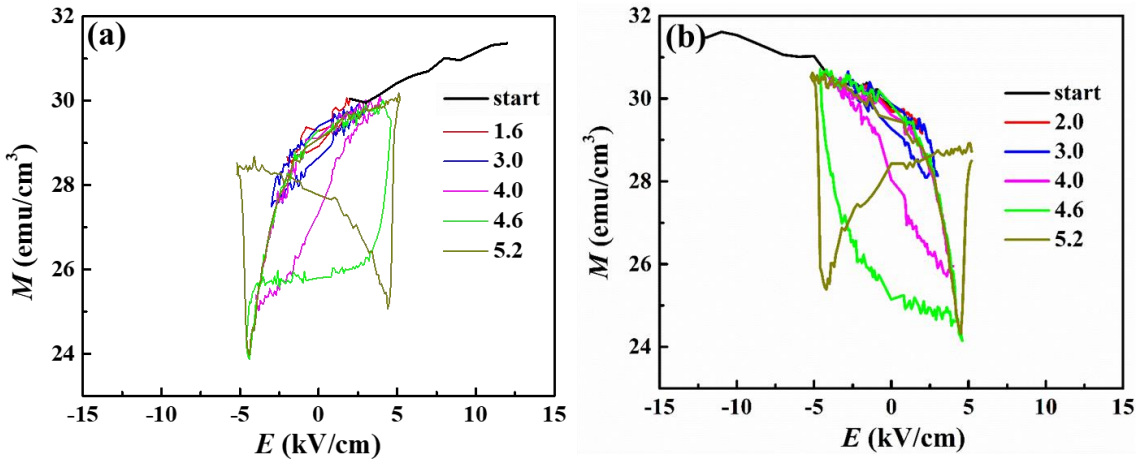

Figure 6.25 *M*-*E* curves of YIG/Pt/PMN-PZT/Pt heterostructure under cycling electric field with different amplitudes at 0 Oe. (a) Poled at +12 kV/cm and (b) poled at -12 kV/cm.

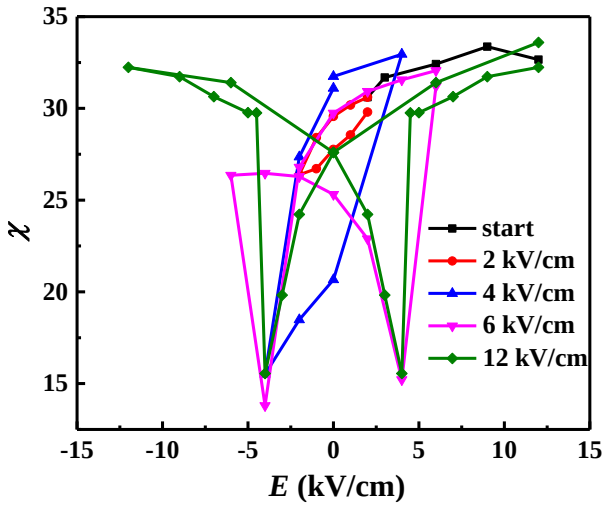

Figure 6.26 χ-*E* curves of YIG/Pt/PMN-PZT/Pt heterostructure under cycling electric field with different amplitudes at 20 Oe.

The χ-*E* curves of YIG/Pt/PMN-PZT/Pt heterostructure under cycling electric field with different amplitudes at 20 Oe are given as representatives in Fig. 6.26. When $E \leq E_C$, the shuttle-like χ-*E* curves can be observed. With the amplitude increasing, the χ-*E* curves switched into butterfly-like ones. The shuttle-like χ-*E* curves show great potential to fabricate linear *E*-tunable inductance.

The results of Fig. 6.25 and Fig. 6.26 have evoked two potential applications in YIG/Pt/PMN-PZT/Pt heterostructure with low amplitudes of cycling electric field; they are magnetoelectric memory devices and tunable devices. When the amplitude of *E* equals 4.6 kV/cm, the two *E*-field controlled distinct remnant magnetization states

show the great potential in the application of energy-efficient ME random access memory devices. While the amplitude of *E* equals 4 kV/cm, the slim shuttle-like *M*-*E* curve indicates large and linear *E*-tunable susceptibility for RF/microwave magnetic devices.

In order to simulate the real memory write process, a dynamic voltage-pulse-induced magnetization switching in YIG/PMN-PZT, is shown in Fig. 6.27. With the zero magnetic bias field, the magnetization response to the electric field shows a reversible hysteretic type behavior, as illustrated in Fig. 6.27 (a). The remnant magnetization was reversibly switched from state "1" to state "0" with a magnitude of magnetization ratio of 6.2%. Furthermore, memory-type dynamically switching of magnetization between the two magnetization states is demonstrated in Fig. 6.27 (b). The electric field pulses of 4.6 kV/cm and -4.6 kV/cm are applied alternately at a period of 60 s. As an E-field pulse of 4.6 kV/cm has been applied, magnetization in YIG rises and remains at a magnetization ratio of 54.4%, which means a switch from the state "1" to state "0". Similarly, the magnetization was reduced and stayed at a magnetization ratio of 48.2%, as an *E*-field pulse of -4.6 kV/cm has been applied, indicating the switching from “0” to “1.”Therefore, dynamic E-field-pulse-induced magnetization switching in YIG was realized with zero magnetic field and a low electric field of 4.6 kV/cm. This memory-type of magnetization switching would result in the non-volatile magnetization tuning with excellent energy efficiency.

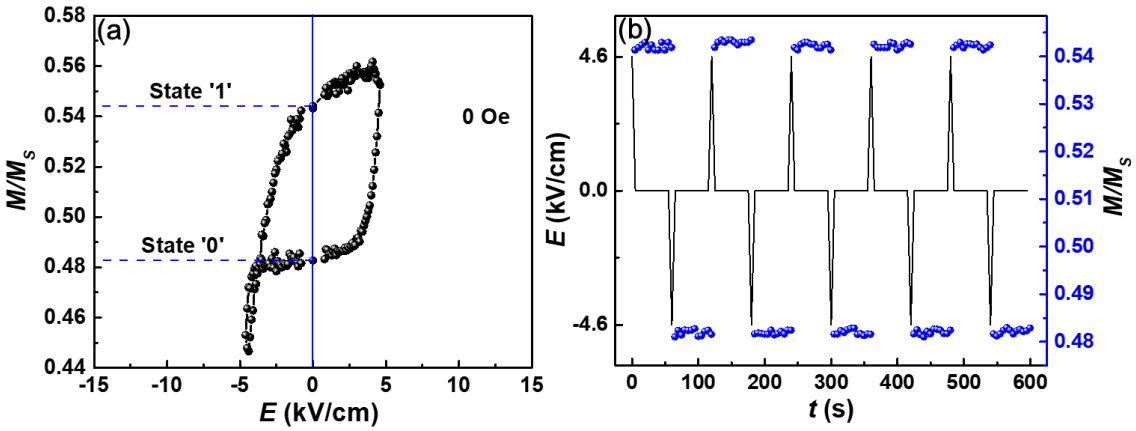

Figure 6.27 (a) The *M*-*E* curve with an electric field cycle from -4.6 kV/cm to 4.6 kV/cm, (b) the time-dependent magnetization switched by the electric field at 0 Oe of YIG/Pt/PMN-PZT/Pt heterostructure.

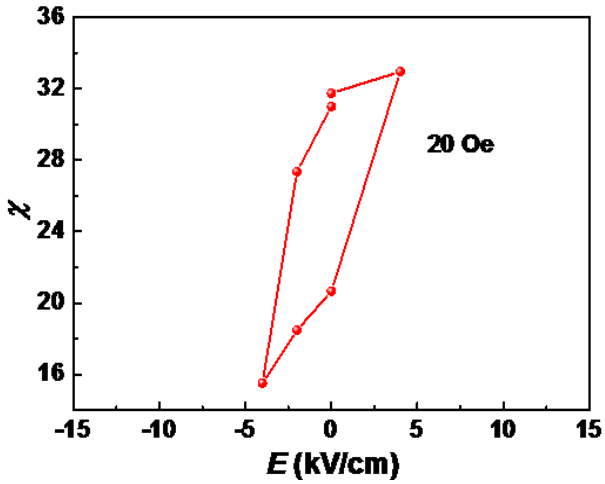

Figure 6.28 The χ-*E* curve with an electric field cycle from -4 kV/cm to 4 kV/cm at 20 Oe of YIG/Pt/PMN-PZT/Pt heterostructure.

The *E*-tunable susceptibility shifts of YIG/Pt/PMN-PZT/Pt heterostructure are presented in Fig. 6.28. With the cycling electric field of 4 kV/cm, the linear-like slanted χ-*E* curve is observed, and the χ varies in the range of 15.5 and 32.9. The large *E*-tunable susceptibility ratio can reach $\Delta\chi/\chi_{0+}$ =55.5% at 20 Oe and with a cycling electric field of 4 kV/cm. Other than conventional magnetic components or devices, *E*-tunable devices with larger tunability and lower energy consumption, where tunability is achieved by adjusting the electric field, can be developed.[20]

Thus two interesting multiferroic applications can be developed depending on YIG/Pt/PMN-PZT/Pt heterostructures. On the one hand, the voltage-pulse reversible magnetization switching of YIG/Pt/PMN-PZT/Pt heterostructures is realized at 0 Oe with an electric field impulse of ±4.6 kV/cm, which shows the feasibility of power-efficient *E*-field controlled nonvolatile memories. On the other hand, the linear *E*-tunable susceptibility change can be realized at 20 Oe and 4 kV/cm, and the tunable susceptibility can reach $\Delta\chi/\chi_{0+}$ =55.5%, indicating the potential of power-efficient magnetoelectric tunable devices.

6.3.2 Out-of-plane *E*-field controlled Magnetism in YIG/Pt/PMN-PZT/Pt heterostructure

For these measurements, the magnetic field is vertically applied to the YIG/Pt/PMN-PZT/Pt heterostructure.

The electric-field dependence of out-of-plane *M-H* loops of YIG/Pt/PMN-PZT/Pt heterostructure are illustrated in Fig. 6.29. With the absence of an electric field, the out-of-plane *M-H* loop shows different shapes from the in-plane *M-H* loop. It can be observed that the out-of-plane saturate magnetic field of YIG film is much higher than in-plane results, indicating that the YIG film has an "easy plane" in the PMN-PZT substrate plane that more energy is needed for YIG film to be saturated along out-of-plane direction. Under an application of electric field, the *M-H* loops weakly vary with the electric-field-induced strain. The minor electric field induced magnetic variations demonstrate that the strain-induced magnetization or demagnetization effect is weak along the out-of-plane direction. These results can be explained by the strain-induced magnetic domain motion is hindered in thickness-direction due to its low dimension. However, large strain-induced magnetic variation can be achieved because of its large dimension in width- and length-direction.

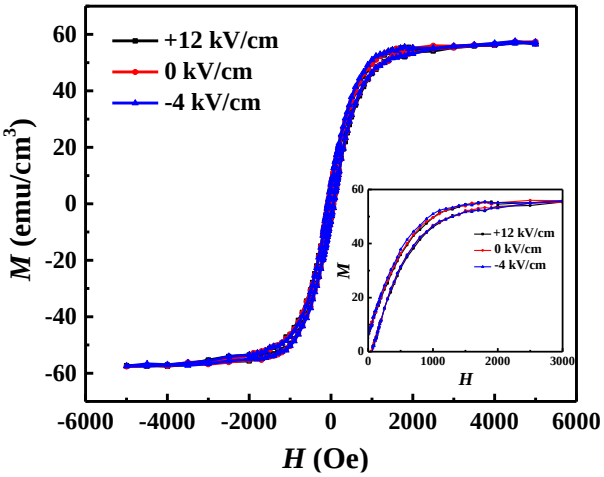

Figure 6.29 The electric-field dependent *M-H* loops of YIG/Pt/PMN-PZT/Pt heterostructure.

The out-of-plane magnetization change as a function of the electric field at 500 and 1000 Oe in YIG/Pt/PMN-PZT/Pt heterostructure are given in Fig. 6.30. The butterfly-like shape of *M-E* curves can be observed; even the strain-induced magnetic variations are small. The compressive out-of-plane strain favors the magnetization process, while tensile out-of-plane strain leads to the demagnetization process, which agrees with in-plane results. With the bias magnetic field increasing, the strain-induced magnetization or demagnetization process is also hindered by the bias magnetic field.

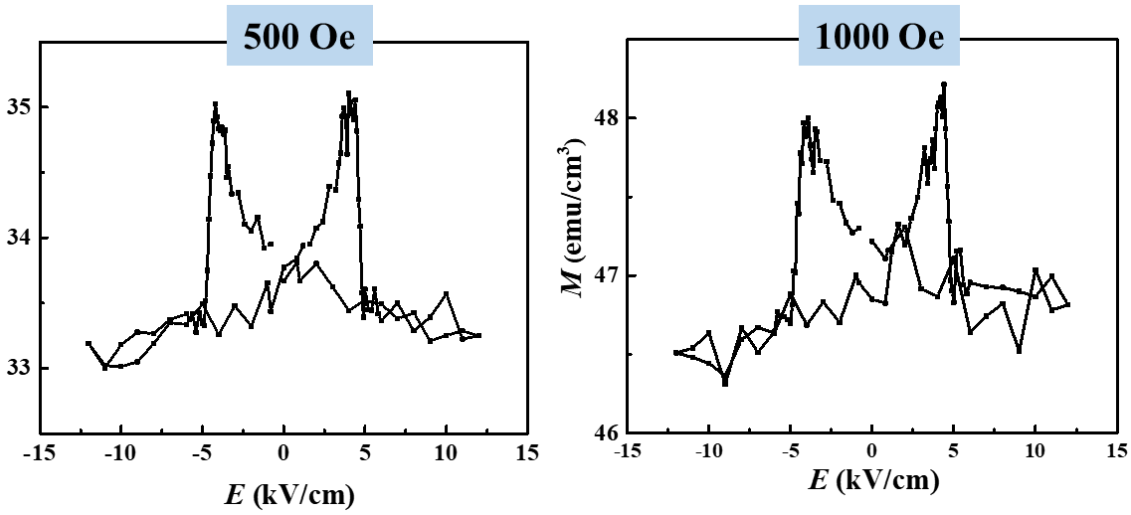

Figure 6.30 The out-of-plane *M-E* curves of YIG/Pt/PMN-PZT/Pt heterostructure.

The typical in-plane and out-of-plane *M-E* curves of YIG/Pt/PMN-PZT/Pt heterostructure are given in Fig. 6.31. Accounting to the in-plane and out-of-plane *S-E* curves of PMN-PZT, given in Fig. 4.6, it can be concluded that the compressive strain favors the magnetization process, while tensile strain leads to the demagnetization process in the YIG film. The electric field induced in-plane magnetization variations are much larger than out-of-plane ones. These differences can be explained by the strain-induced magnetic domain motion is hindered in thickness-direction due to its low dimension. However, large strain-induced magnetic variation can be achieved because of its large dimension in width- and length-direction.

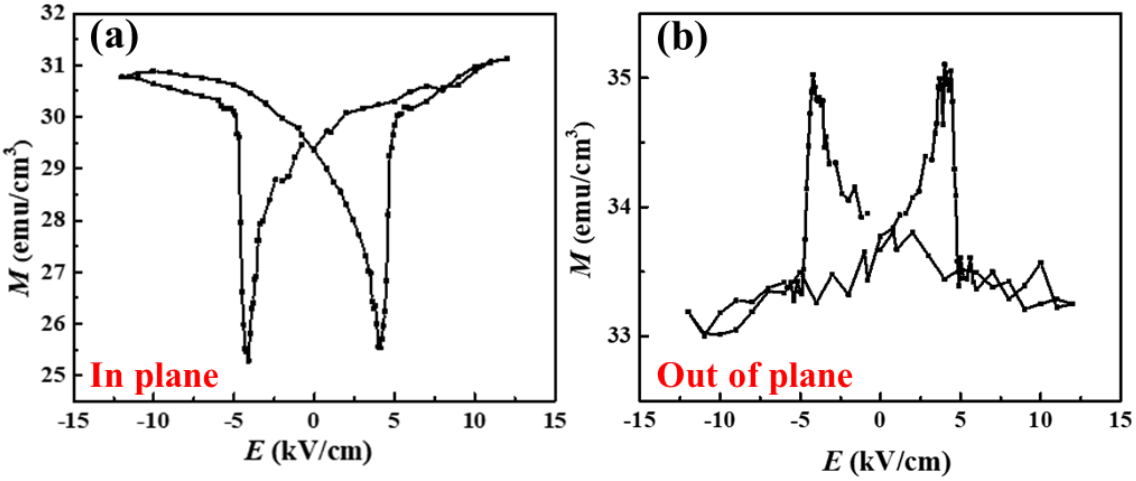

Figure 6.31 The in-plane *M-E* curve at 0 Oe and out-of-plane *M-E* curve at 500 Oe of YIG/Pt/PMN-PZT/Pt heterostructure.

The electric field induced magnetization change also indicates the transformation of the magnetic crystalline anisotropy. The schematic of the anisotropy axis change with the electric field can be illustrated in Fig. 6.32.

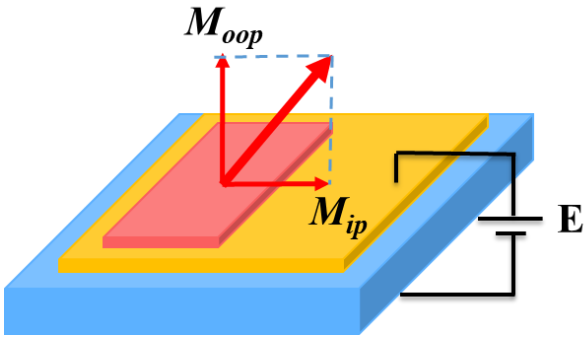

Figure 6.32 Schematic of electric field induced anisotropy change in YIG/Pt/PMN-PZT/Pt heterostructure.

When the electric field induces an in-plane compressive strain and an out-of-plane tensile strain at the same time, the anisotropy axis will tilt to in-plane direction. Thus the in-plane magnetization (M_{ip}) increases, and out-of-plane magnetization (M_{oop}) decreases. In contrast, when the electric field induces an in-plane tensile strain and an out-of-plane compressive strain, the anisotropy axis would tilt to the out-of-plane direction. Thus the in-plane magnetization (M_{ip}) reduces, and out-of-plane magnetization (M_{oop}) rises.

6.3.3 Summary

In this part, we have investigated the in-plane *E*-field controlled magnetism in YIG/Pt/PMN-PZT/Pt heterostructure. The electric-field-dependent *M-H* loops and χ-*H* curves reveal the strain-mediated transformation of magnetocrystalline anisotropy in the YIG film. As a result, the *E*-field controlled *Mr*, H_C, and χ change correspondingly with the PMN-PZT ceramic's strain evolution. The CME coefficient can reach 16.95 × 10^{-8} s/m in the absence of bias magnetic field at E_C of PMN-PZT ceramic, and the maximum of CME coefficient (18.15 × 10^{-8} s/m) is observed under the magnetic field of 25 Oe, demonstrating strong converse magnetoelectric coupling effect in

YIG/Pt/PMN-PZT/Pt heterostructure. When the application of electric field amplitude is close E_C of PMN-PZT, the *E*-induced shuttle-like strain evolution of PMN-PZT favors two possible applications in YIG/Pt/PMN-PZT/Pt heterostructure. On the one hand, two distinct remnant strain states lead to two stable magnetization states of the YIG film. The voltage-impulse reversible magnetization switching of YIG/Pt/PMN-PZT/Pt heterostructures is realized at 0 Oe with an electric field impulse of ±4.6 kV/cm, which shows the feasibility of power-efficient *E*-field controlled nonvolatile memories. On the other hand, the linear *E*-tunable susceptibility change can be realized at 20 Oe and 4 kV/cm, and the tunable susceptibility can reach $\Delta\chi/\chi_{0+}$ =55.5%, indicating the potential of power-efficient magnetoelectric tunable devices.

The *E*-field control of magnetism in YIG/Pt/PMN-PZT/Pt heterostructures is achieved by *E*-field induced magnetic anisotropy change. When the electric field induces an in-plane compressive strain and an out-of-plane tensile strain in PMN-PZT ceramic at the same time, the anisotropy axis of YIG film will tilt to in-plane direction. In contrast, when the electric field induces an in-plane tensile strain and an out-of-plane compressive strain in PMN-PZT ceramic, the anisotropy axis of YIG film would tilt to the out-of-plane direction.

6.4 Conclusions: comparison of FE (AFE)/YIG performances

The in-plane and out-of-plane *E*-field control of magnetism in YIG/AFE and YIG/FE (YIG/Pt/PLZST/Pt and YIG/Pt/PMN-PZT/Pt) heterostructures are studied in this part of work. The CME coupling effect in YIG/AFE and YIG/FE does share the same strain-mediated coupling mechanism, as given in following:

1. The *E*-field controlled *Mr*, H_C, and χ of YIG films change correspondingly with the substrate's strain evolution (*S*-*E* curves), indicating the effectiveness of strain-mediated CME coupling effect.

2. The strain-induced magnetic anisotropy transformation of YIG film results in the magnetization or demagnetization effect in the plane or along the OOP direction with an application of the electric field.

However, there are some differences in performances due to the different strain evolutions of the substrates under the electric field. The AFE materials display zero

remnant states; thus, in AFE-based ME composites, the pre-poling process is not necessary. The AFE-FE switching field of PLZST is 50 kV/cm with a maximum strain of 0.2 %. The FE materials show hysteresis loops, and the electric load history influences the following results. The E_C of PMN-PZT ceramics is as low as 4.2 kV/cm, while the *E*-induced in-plane and out-of-plane strain can reach 0.08% and -0.27% at E_C, respectively. When the electric field is lower than E_C, the *S*-*E* curves are shuttle-like, and there are two remnant strain states.

1. The large *E*-induced phase transition strain in AFE substrate leads to maximum in-plane α_{CME} (11.6×10^{-8} s/m) at 0 Oe in YIG/Pt/PLZST/Pt heterostructure under an electric field of 50 kV/cm. The in-plane CME coefficient in YIG/Pt/PMN-PZT/Pt heterostructure can reach 16.95×10^{-8} s/m in the absence of bias magnetic field at E_C of PMN-PZT ceramic, and the maximum of in-plane CME coefficient (18.15×10^{-8} s/m) is observed under the magnetic field of 25 Oe ($@H_C$). However, it is necessary to point out that even though the maximum of α_{CME} is obtained at a low electric field of 4.2 kV/cm, but a pre-polling process to PMN-PZT substrate is essential to obtain this high α_{CME}. Otherwise, a large in-plane strain of -0.27% cannot be obtained at E_C.

Good CME coefficients of YIG/Pt/PLZST/Pt and YIG/Pt/PMN-PZT/Pt show that AFE and FE materials are both potential candidates in ME composites. However, in general, the switching field of AFE materials is always very high, which may be not suitable to develop AFE-bulk ME composites. The required high voltage of AFE bulks would greatly restrict their applications in ME composites. The reduction of the thickness in AFE materials should be a solution to avoid high voltages. Thus, AFE-based ME thin films are a possible way to utilize the advantages (no pre-poling process) of AFE materials and avoid high voltages, which is interesting for volatile memory devices.

2. When the application of electric field amplitude is close to E_C of PMN-PZT, the voltage-impulse reversible magnetization switching and the linear *E*-tunable susceptibility change can be realized in YIG/Pt/PMN-PZT/Pt heterostructures because of the shuttle-like *S*-*E* curves of PMN-PZT substrate. These features of FE materials give us another way to develop FE-based ME composites with low power consumption. The reversible voltage-impulse reversible magnetization switching is realized at 0 Oe

and with the application of electric field pulse of which the amplitude is close to E_C of PMN-PZT, implying great potential in non-volatile memory devices.

3. The maximum of in-plane $\Delta\chi/\chi_0$ in YIG/Pt/PLZST/Pt heterostructure is 33% at 10 Oe and with an electric field cycle from 0 to 50 kV/cm, and a linear *E*-tunable susceptibility change is realized. In YIG/Pt/PMN-PZT/Pt heterostructures, the linear *E*-tunable susceptibility change can be realized at 20 Oe and with an electric field cycle from -4 to +4 kV/cm, and the tunable susceptibility can reach $\Delta\chi/\chi_{0+}$ =55.5%. Once again, the AFE- and FE-based ME composites show good potential in E-tunable microwave devices. The difference in the values in $\Delta\chi/\chi_0$ may be due to the differences in strain values. Again, the reduction of the thickness in AFE materials should be a solution to avoid high voltages.

The *E*-field controlled magnetism in YIG/AFE and YIG/FE demonstrated that the electric-field induced strain is responsible for the plays a vital role in the CME coupling effect. The difference in the relationship of strain and electric field in ceramic substrates favors the difference in the CME coupling effect of YIG/AFE and YIG/FE. The interfaces quality plays, of course, a key role in the coupling efficiency, we do not take into account this parameter in our studies.

7 CME Coupling Effect of $[(TbCo_2)/(FeCo)]_{20}$ Films on AFE and FE Ceramics

Various materials have been used as the ferromagnetic/ferrimagnetic phases to couple with FE phases. In the last chapter, the CME coupling effect between the ferrimagnetic phase (YIG) and AFE or FE phases has already been demonstrated. In general, ferromagnetic materials, especially the 3d-transition metals (Fe, Co, and Ni) and alloys (permendur, Terfenol-D, Galfenol), present a more excellent magnetic performance at low frequency. They are also essential parts of designing FM/FE composites, in which the excellent ME coupling effect has already been demonstrated. The rare-earth metal Tb modified Co/Fe alloy shows excellent magnetic properties, high magnetostriction, and large saturated magnetization when compared with ferrite YIG,[35,133,134] which makes it an excellent ferromagnetic material in ME composites. In this chapter, the ferromagnetic materials (Tb modified Co/Fe alloy) are used to couple with AFE and FE phases to understand the AFE- and FE- based CME coupling effects.

Amorphous $[(TbCo_2)/(FeCo)]_{20}$ (TCFC) film was chosen to be another FM layer due to its high perpendicular magnetic anisotropy, which allows us to study the CME effect along different in-plane axes.[135,136] The previous work of $[(TbCo_2)/(FeCo)]_x$ (TCFC) films on PMN-PT single-crystal slabs has shown great potential in voltage-controlled magnetoelectric read and write operations when focusing at random access memory devices.[35,38,39] TCFC films show many advantages in ME composites, but the study of *E*-field tuning of magnetism in TCFC/AFE heterostructures has not been reported yet. In this chapter, the TCFC/PLZST heterostructure was carried out, and the CME coupling effect has been studied. Since the TCFC is anisotropic in the plane, it is interesting to explore the differences of the CME coupling effect along different in-plane axes (easy axis and hard axis). To further understand the CME coupling effect of TCFC films on ceramic substrates, the TCFC/PMN-PZT heterostructure has also been carried out in this part, and the voltage induced magnetism along different axes has been studied.

7.1 Preparation of TCFC/AFE and TCFC/FE Heterostructures

The [(TbCo$_2$)/(FeCo)]$_{20}$ multilayers were deposited by sputtering on one side of the PLZST and PMN-PZT ceramic substrates layer by layer, where the thickness of each layer is 5 nm, as given in Fig. 7.1 (a). An easy magnetic axis is obtained in the magnetic layer by applying a magnetic field during deposition. This layer also serves as the top electrode for its good conductivity. The final thickness of the multilayers is 200 nm. The dimensions of TCFC film was restricted to be 6 × 6 mm^2 by masks. Since the TCFC films are sensitive to temperature and can lose its magnetic properties at ~100 ℃. A soldering process for wire attachments is not suitable in this case. Then the Au electrodes were deposited on both sides on the heterostructure. The choice of Au electrodes is for the following nano Au wire growth method to attach wires. The easy axis and hard axis of TCFC film are perpendicular, and they are controlled to be in the plane through the deposition process, as shown in Fig. 7.1 (b).

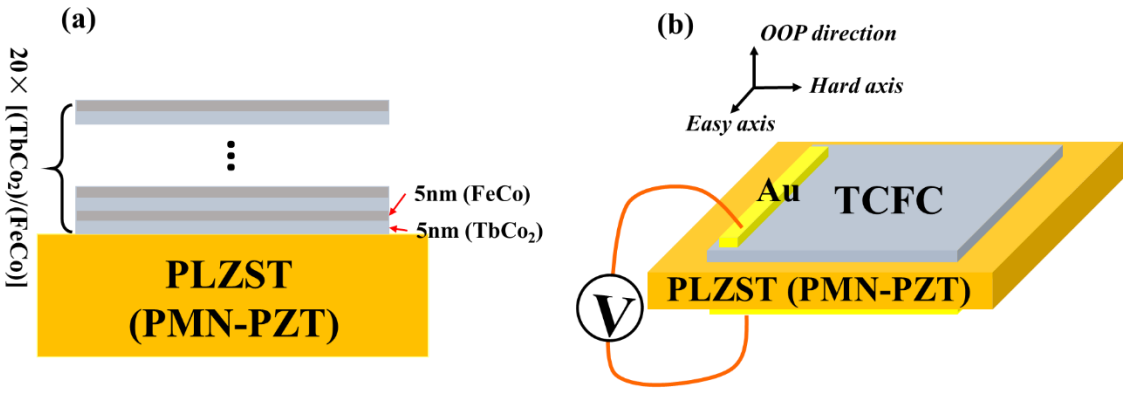

Figure 7.1 (a) Schematic of TCFC multilayers and (b) TCFC/PLZST/Au heterostructure.

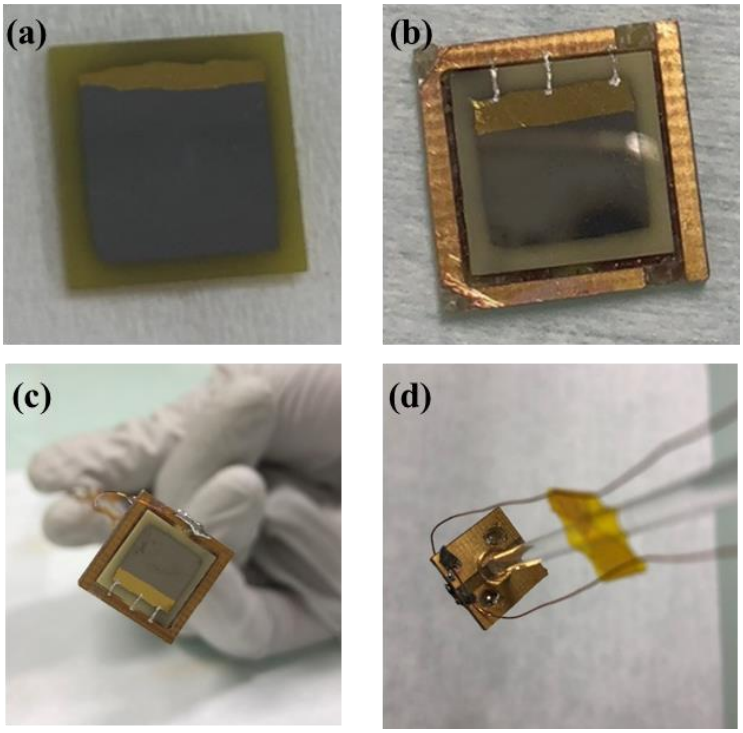

Figure 7.2 (a) Front side of TCFC/PLZST (PMN-PZT)/Au heterostructure, (b) picture of TCFC/PLZST (PMN-PZT)/Au connected to sample holder, (c) front side and (d) backside of TCFC/PLZST (PMN-PZT)/Au connected with wires.

The TCFC film is sensitive to temperature that the hot soldering process should avoid being directly on TCFC film. A designed sampler holder is used for wire connection. Figure 7.2 illustrates that the TCFC/PLZST (PMN-PZT)/Au heterostructure is able to connect with wires through a connection of sample holder. Firstly, the front and back Au electrodes of TCFC/PLZST (PMN-PZT)/Au heterostructure connect to the front and back sides of the sample holder using the nano Au wire growth method, respectively. Then the wires can be attached to the conductive front and back sides of the sample holder through the soldering process.

7.2 [(TbCo$_2$)/(FeCo)]$_{20}$/PLZST/Au Heterostructure

Magnetocrystalline anisotropy is the energy necessary to deflect the magnetic moment in a single crystal from the easy to the hard direction, and it is an intrinsic property of magnetic materials. It can be easily seen by measuring magnetization curves along with different crystal directions. Depending on the crystallographic orientation of TCFC film in the magnetic field, the magnetization reaches saturation in different

fields. The magnetization in the easy axis is mostly easy to reach the saturation, while the magnetization in hard-axis is usually saturated in a higher magnetic field.

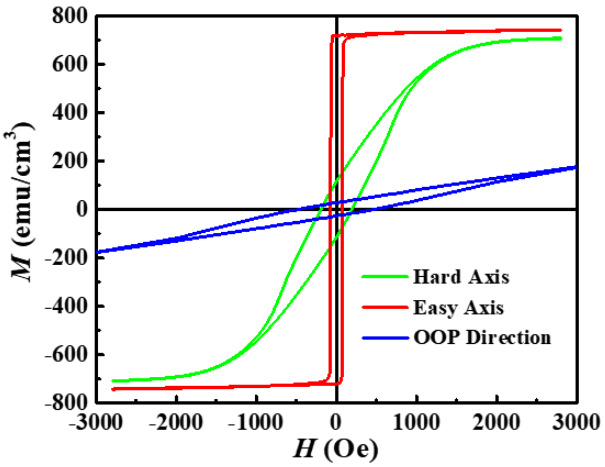

Figure 7.3 The *M–H* loops of TCFC/PLZST/Au heterostructure along with different directions.

The *M–H* loops of TCFC/PLZST/Au heterostructure along different directions are given in Fig. 7.3. The TCFC multilayer presents excellent magnetic performance on the ceramic substrate. A saturated magnetization of ~700 emu/cm^3 was observed in the TCFC multilayer, demonstrating its strong ferromagnetism. The TCFC multilayer is a uniaxial film in the plane; thus, different *M-H* loops were obtained along with different directions. When the magnetic field is along the OOP direction, the TCFC film cannot be saturated with a magnetic field of 2.1 Tesla, indicating there is a strong in-plane anisotropy field that larger energy is needed to deflect the magnetic moment from in-plane to OOP direction.

7.2.1 CME Effect along Hard Axis

Figure 7.4 shows the *M-H* loop of TCFC on PLZST ceramic along the hard axis. The saturated magnetization of TCFC can reach 706 emu/cm^3, and the H_C is 190 Oe. It can be observed that the TCFC film gets saturated with a magnetic field of ~1500 Oe.

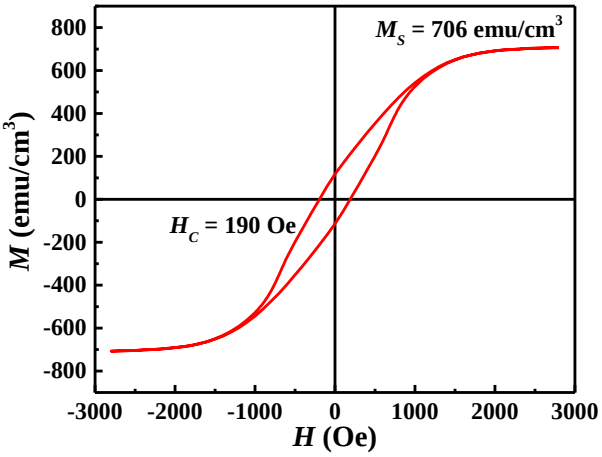

Figure 7.4 The *M–H* loop of TCFC/PLZST/Au heterostructure along the hard axis.

In TCFC film, the magnetic moments are spontaneously aligned to the easy axis. When the external magnetic field is perpendicular to the easy axis, magnetic moments become to rotate. If the amplitude of the external magnetic field is lower than the saturation field of TCFC, parts of magnetic moments are spontaneously aligned to the easy axis, parts are aligned to the hard axis, and the rest parts are in between. In this case, if the electric field induced strain is applied to TCFC film, the orientation of magnetic moments can be easily changed.

The *M–E* curves of TCFC/PLZST/Au heterostructure along the hard axis are given in Fig. 7.5. Under a specific magnetic field, the sample was also saturated in a high magnetic field of 2.1 Tesla before the measurements to eliminate the historical effect, then the first cycle and second half cycle of electric-field-induced magnetization were recorded. For the first cycle of *the M-E* loop, the magnetization variations can be divided into two parts, that is the reversible part and the irreversible part. As it has been discussed in Chapter 6.2.1, the irreversible part only occurs in the first *M-E* loops, and it can be characterized by the difference of the magnetization between the initial state (M_{0i}), at the beginning of the measurements, and the magnetization state at the end of first electrical cycle (M_{0f}) in the first cycle of *M-E* loop. For the second half of the *M-E* loop, the magnetization of the initial state and the end state are almost the same. Thus it is reversible.

In Fig. 7.5, when the external magnetic field is lower than H_C, the *M-E* curves show typical horn-like loops, which is in the same shape of *the S-E* curve of the PLZST

ceramic substrate. The horn-like M-E curves demonstrate the effectiveness of the strain-mediated ME coupling effect. The application of strain (AFE-FE) can destroy the alignment of magnetic moments to the hard axis and leads to a demagnetization process, and the removal of strain (FE-AFE) can lead to a magnetization process. When the external magnetic field is equal to or greater than H_C, the application of strain gradually becomes a role in leading to a magnetization process, and the removal of strain leads to a demagnetization process. In the first cycle of *the M-E* curve at 500 Oe, the magnetization of TCFC first decreases greatly at the AFE-FE switching field, which can be attributed to that the strain destroys the remnant alignment of magnetic moments to the hard axis. When the external magnetic field is 1000 Oe, the applied electric field induced strain of PLZST can rise the magnetization of TCFC, indicating that the strain helps the magnetic moments to align to the hard axis. And the remove of strain can destroy the alignment of magnetic moments and lead to a demagnetization process. In a word, with the application of different amplitudes of the external magnetic field, the applied electric field induced strain can result in different effect, i.e., a demagnetization effect when $H < H_C$, a magnetization effect when $H \geq 1000$ Oe and a mixing effect at $H_C \leq H < 1000$ Oe. A detailed discussion and analysis of this phenomenon will be given in Chapter 7.3.

Since the second cycles of *M-E* curves give the reversible *E*-field controlled magnetization switching, the ΔM and CME coefficient is calculated from the second half *M-E* curves, as given in Fig. 7.6. The M_0 is the magnetization without the electric field in the second half *M-E* curves, and the ΔM is the magnetization difference between M_E and M_0. The peaks of the CME coefficient always occur at the switching field of PLZST ceramic, where the phase transition strain bursts out. The quick change of *E*-field induced strain results in sharp magnetization change and leads to a large α_{CME} at switching field of PLZST.

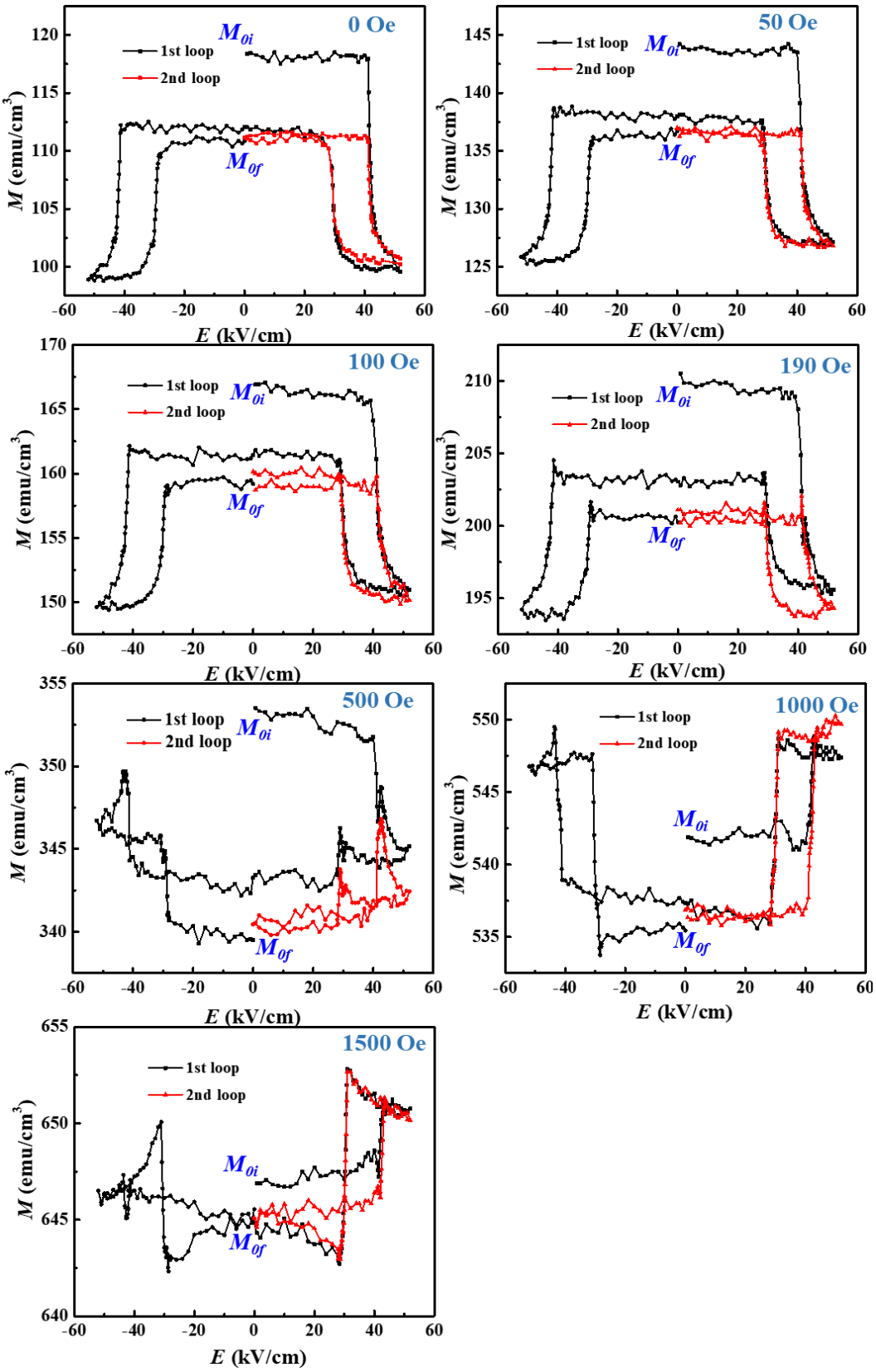

Figure 7.5 The *M*–*E* curves of TCFC/PLZST/Au heterostructure along the hard axis at 0, 50, 100, 190, 500, 1000, and 1500 Oe.

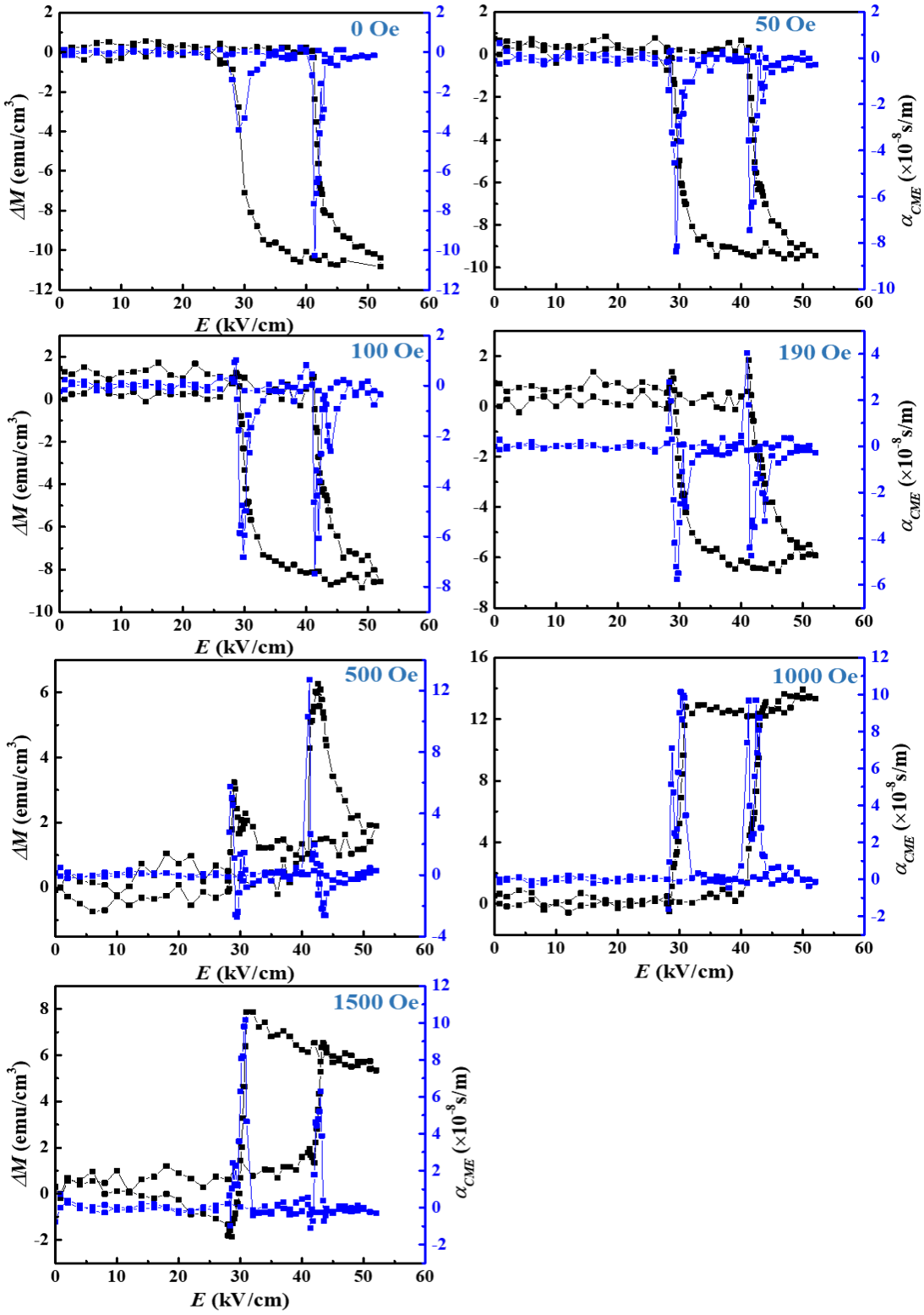

Figure 7.6 The ΔM–E, and α_{CME}–E curves of TCFC/PLZST/Au heterostructure along the hard axis at 0, 50, 100, 190, 500, 1000, and 1500 Oe.

Table 7.1 gives the reversible and irreversible parts of *E*-field induced magnetization in TCFC/PLZST/Au heterostructure along the hard axis. The irreversible part (M_{0i}-M_{0f}) is calculated from the first loop of *M*-*E* curves. With the external magnetic field increasing, the ΔM is firstly negative; then it goes to positive. The irreversible part is positive under a different magnetic field, demonstrating the existence of an unrecoverable part of the magnetic domain motion caused by *E*-field induced strain.

Table 7.1 The reversible and irreversible parts of *E*-field induced magnetization in TCFC/PLZST/Au heterostructure along the hard axis.

Bias *H* (Oe)	0	50	100	190	500	1000	1500
ΔM (emu/cm^3)	-10.88	-10.33	-10.14	-7.45	6.35	12.28	7.58
(M_{0i}-M_{0f}) (emu/cm^3)	7.51	7.52	7.70	10.27	14.04	6.46	1.36

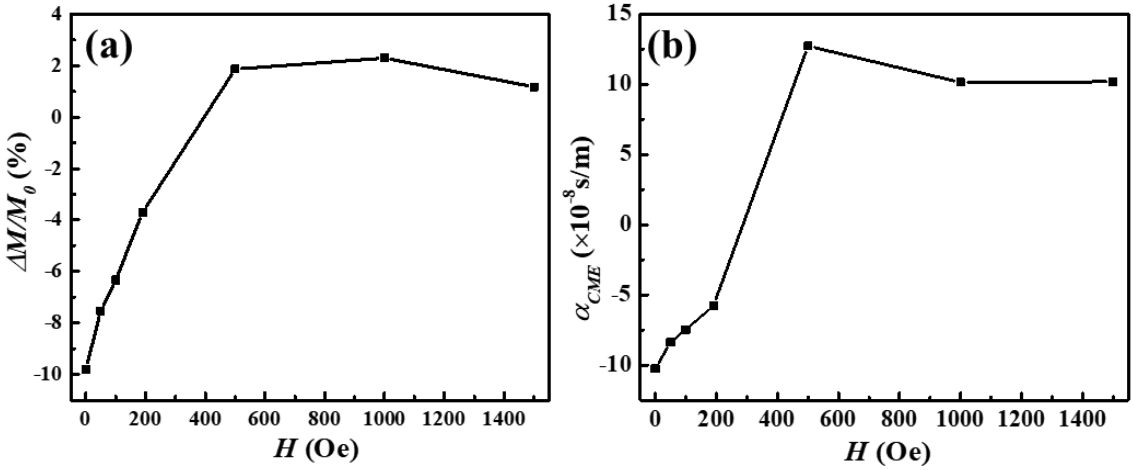

Figure 7.7 (a) The $\Delta M/M_0$-*H* curve and (b) α_{CME}–*H* curve of TCFC/PLZST/Au heterostructure along hard axis.

Figure 7.7 shows the $\Delta M/M_0$-*H* curve and α_{CME}–*H* curve of TCFC/PLZST/Au heterostructure along the hard axis. The relative magnetization change $\Delta M/M_0$ can reach -9.8% with an absence of a magnetic field, then it goes up to 1.9% at 500 Oe and reaches the maximum of 2.3% at 1000 Oe. Without the external magnetic field, the α_{CME} is at the negative maximum of -10.3×10^{-8} s/m, and the positive maximum of α_{CME} is at 500 Oe with a value of 12.7×10^{-8} s/m.

7.2.2 CME Effect along Easy Axis

Figure 7.8 shows the *M*-*H* loops along the easy axis of TCFC/PLZST/Au heterostructure under different electric fields. With an application of the electric field of 44 kV/cm, the electric-field induced AFE-FE phase transition happens in PLZST, accompanied by a large phase deformation strain. However, the large *E*-induced strain did not lead to a distinct change in *M*-*H* loops. The inset shows enlarged *M*-*H* loops around H_C, but the *E*-induced variation is too small to be distinguished. The highly intrinsic crystallographic orientation in the magnetic field of TCFC makes it difficult to induce the magnetic moment rotation or motion by strain. The strain-induced magnetization variations are almost forbidden along the easy axis. Thus it is difficult to realize the CME effect along the easy axis in TCFC/PMN-PZT/Au heterostructure.

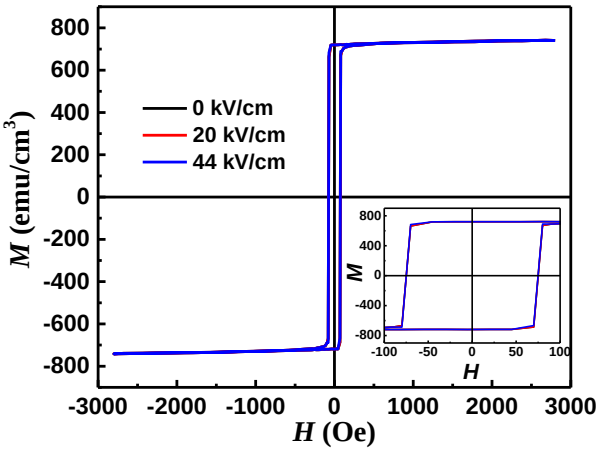

Figure 7.8 The *M* -*H* loops along the easy axis of TCFC/PLZST/Au heterostructure under different electric fields.

7.2.3 CME Effect along OOP Direction

Figure 7.9 shows the *M*-*H* loops along the OOP direction of TCFC/PLZST/Au heterostructure under different electric fields. With an application of the electric field, the *M*-*H* loops have not presented any visible variations. The TCFC film has a strong in-plane anisotropy field that larger energy is needed to deflect the magnetic moment from in-plane to OOP direction. In this case, the energy of *E*-induced strain in PLZST maybe not high enough to deflect the magnetic moment from in-plane to OOP direction. Thus the CME coupling effect is too small to be detectable along the OOP direction.

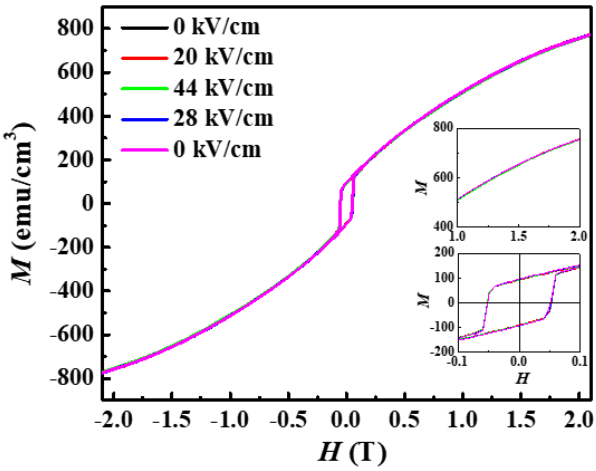

Figure 7.9 The *M* -*H* loops along the OOP direction of TCFC/PLZST/Au heterostructure under different electric fields.

7.2.4 Summary

In this part of the work, the [(TbCo$_2$)/(FeCo)]$_{20}$/PLZST/Au heterostructure has been prepared, and the *E*-induced magnetism along different axes has been studied. Along the easy axis of TCFC film, the *E*-induced magnetization variation is suppressed by the highly intrinsic crystallographic orientation with the magnetic field. Along the hard axis, the *E*-field controlled magnetization under different bias magnetic fields has been demonstrated, as well as the CME coefficient. A reverse of *M*-*E* curves occurred with the bias magnetic field increasing along the hard axis. The maximum of $\Delta M/M_0$ can reach -9.8% with an absence of the magnetic field, and the α_{CME} is at the negative maximum of -10.3×10^{-8} s/m at the same time. The positive maximum of α_{CME} is at 500 Oe with a value of 12.7×10^{-8} s/m. Along OOP direction, the *E*-induced magnetism is not visible, which can be attributed to that the energy of *E*-induced strain in PLZST is not enough to deflect the magnetic moment from in-plane to OOP direction.

7.3 [(TbCo$_2$)/(FeCo)]$_{20}$/PMN-PT/Au heterostructure

The *M*–*H* loops of TCFC/PMN-PZT/Au heterostructure along different axes are given in Fig. 7.10.

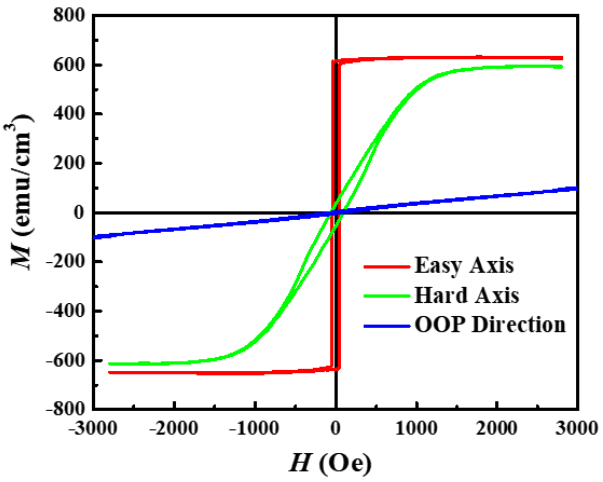

Figure 7.10 The *M–H* loops of TCFC/PMN-PZT/Au heterostructure along with different directions.

The TCFC multilayer presents excellent magnetic performance on the PMN-PZT substrate. A saturated magnetization of ~600 emu/cm^3 was observed. When the magnetic field is along the OOP direction, the TCFC film cannot be saturated with a magnetic field of 2.1 Tesla, indicating there is a strong in-plane anisotropy field that larger energy is needed to deflect the magnetic moment from in-plane to OOP direction.

7.3.1 CME Effect along Hard Axis

Figure 7.11 shows the *M-H* loops along the hard axis of TCFC/PMN-PZT/Au heterostructure under different electric fields. The shape of *M-H* loops changes with different electric fields, indicating apparent strain-induced magnetization variations along the hard axis. A higher magnetic field is needed to deflect magnetic moments from the easy to the hard direction in TCFC film. Thus when the applied magnetic field is low, some parts of the magnetic moments in TCFC film are aligned along the hard axis, and some are not. Then the large strain generated in PMN-PZT ceramic can easily rotate some intermediate magnetic moments and lead to large magnetization variations. As given in Fig. 7.11 inset, when the magnetization is not saturated in TCFC film, the distinguishable strain-induced magnetization variations are observed.

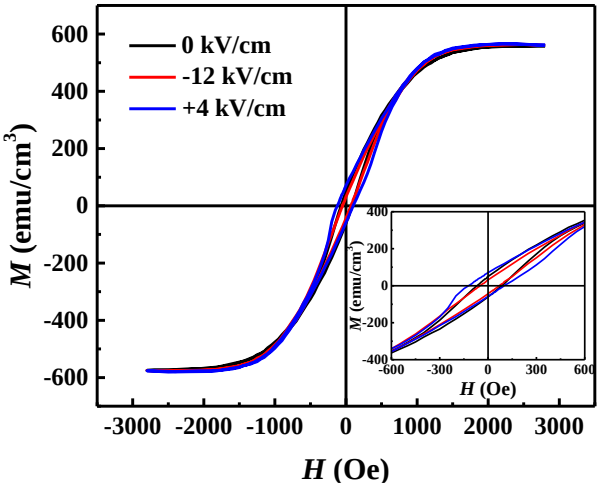

Figure 7.11 The *M-H* loops along the hard axis of TCFC/PMN-PZT/Au heterostructure under different electric fields.

The *M-E* curves of TCFC/PMN-PZT/Au heterostructure along the hard axis are carried out under different magnetic fields. Under a specific magnetic field, the sample was saturated in a high magnetic field of 2.1 Tesla before the measurements to eliminate the historical effect, then the first cycle of electric-field-induced magnetization was recorded. Also, several second cycles of electric-field-induced magnetization were also recorded. Thus the *M-E* curves under a specific magnetic field were finished, then repeated the steps. Figure 7.12 shows how an electric cycle goes. Since the FE ceramic has remnant state after an application of electric field, the applied electric field started from -12 kV/cm to assure that the ceramic was in the same state before the measurements.

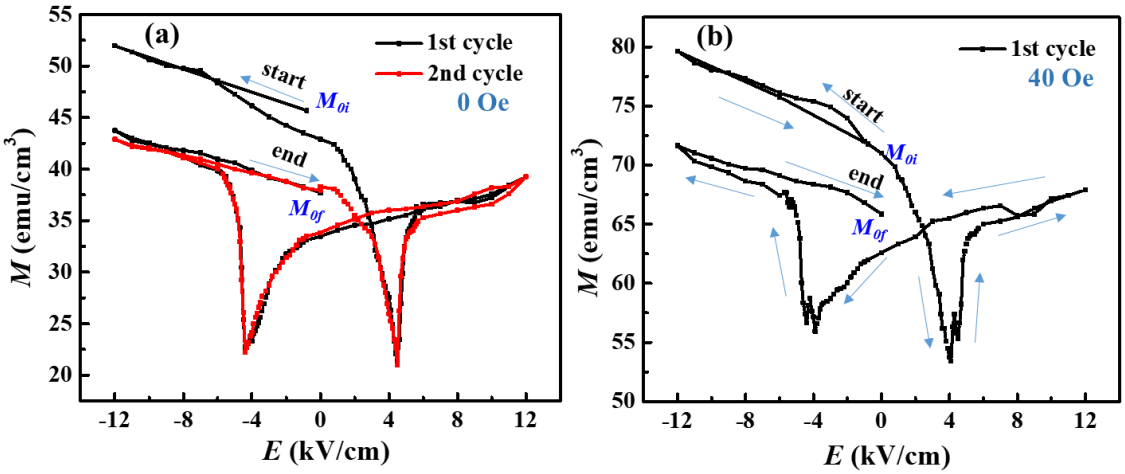

Figure 7.12 The *M-E* curves along the hard axis of TCFC/PMN-PZT/Au heterostructure at 0 and 40 Oe.

For the first cycle of *M-E* curves, the magnetization variations can be divided into two parts, that is the reversible part and the irreversible part. As it has been discussed in Chapter 6.2.1, the irreversible part only occurs in the first cycle of *M-E* curves, and it can be attributed to the unrecoverable magnetic domain motion. For the second cycle of *the M-E* curve, the magnetization of the initial state and the end state are almost the same; thus, it is reversible.

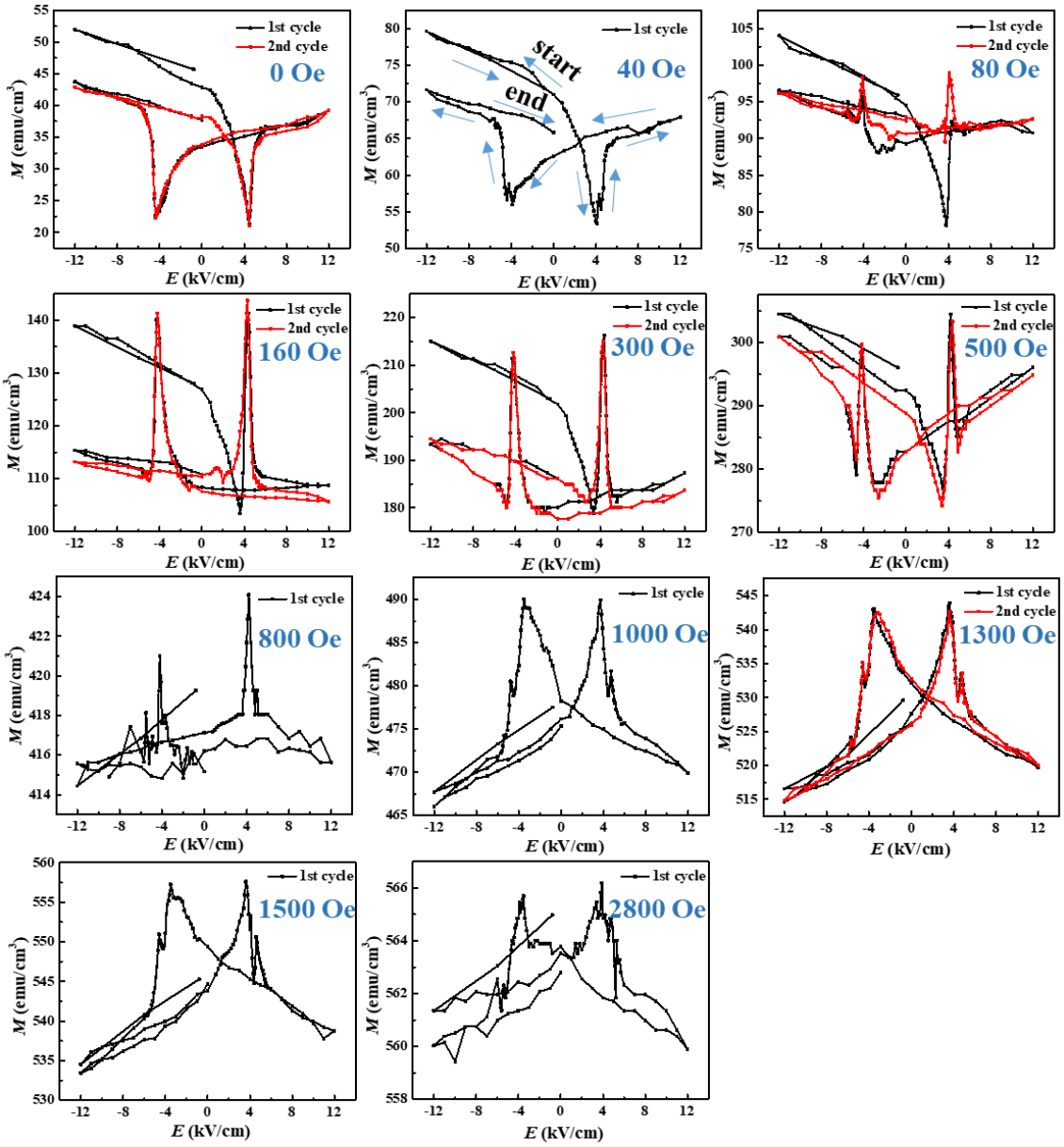

Figure 7.13 The *M-E* curves along the hard axis of TCFC/PMN-PZT/Au heterostructure under different magnetic fields.

Figure 7.13 shows *M-E* curves along the hard axis of TCFC/PMN-PZT/Au heterostructure under different magnetic fields. With the absence of an external magnetic field, the *M-E* curve has a typical butterfly shape which resembles the *S-E* curves of PMN-PZT ceramic. With a magnetic field of 40 Oe, the shape of *the M-E* curve begins to change, and the peak of hindwing of the butterfly-like *M-E* curve gets inverted. Then as the magnetic field increases, the inversed part expands. At 500 Oe, the whole hindwing of the *M-E* curve is inverted when compared with the butterfly-like *M-E* curve at 0 Oe. At 800 Oe, the *E*-field controlled magnetization variations are tiny, and it is difficult to find a relationship between the *E*-field induced strain and magnetization. When the external magnetic field keeps increasing, the *M-E* curve is completely inversed at 1000 Oe, and there are two magnetization peaks around E_C.

To further explain the bizarre behavior of *M-E* curves, the ideal magnetic hysteresis loop along the hard axis is given in Fig. 7.14. For a perfect single crystal, when the applied magnetic field is perpendicular to the easy axis of the material, it presents an oblique-line-like *M-H* loop, and no remnant magnetization and zero H_C. The single crystal saturates at the anisotropy field (H_a), where $H_a=2K/M_S$, M_S is the saturated magnetization, K is the anisotropy coefficient.

If the magnetoelastic coupling constant of a single crystal is negative, and the anisotropy field is H_0. According to Equation 2.4, the external tensile strain would lead more magnetic moments to align perpendicularly to the strain direction, and the magnetic moments tend to align along compressive strain direction. In this case, when an *E*-field induced tensile strain is given, the anisotropy field decreases to H_1. While an *E*-field induced compressive strain is given, the anisotropy field rises to H_2.

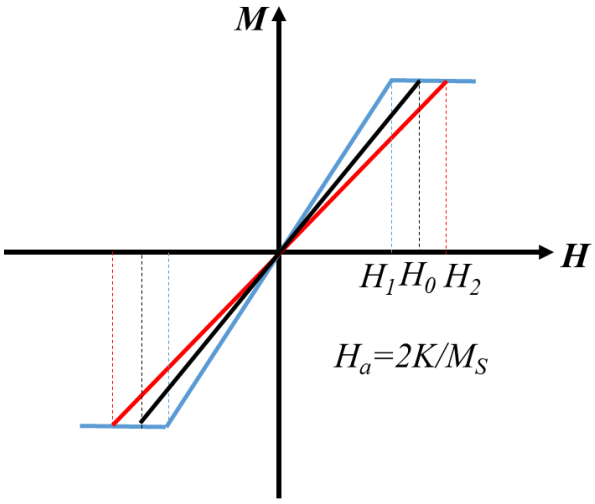

Figure 7.14 The ideal *M*-*H* loops along the hard axis of a single crystal with different strains.

In TCFC/PMN-PZT/Au heterostructure, the magnetoelastic coupling constant of TCFC is negative (-7 MPa).[38] When an *E*-field induced tensile strain is applied to the film, the anisotropy field of TCFC should decrease, and the anisotropy field increases when an *E*-field induced compressive strain is applied.

Figure 7.15 illustrates the details of the real *M*-*H* loops ng hard axis in TCFC/PMN-PZT/Au heterostructure with an application of the electric field. When an electric field of 4 kV/cm is applied to PMN-PZT ceramic, a large tensile in-plane strain and compressive OOP strain would be generated in the ceramic substrate and be transferred to TCFC film. Figure 7.15 (a) shows how the *M*-*H* loop changes with the *E*-field induced tensile in-plane strain and compressive OOP strain. The slope of the *M*-*H* loop varies synchronously with the ideal model, demonstrating the reduction of anisotropy field. When an electric field of -12 kV/cm is applied to PMN-PZT ceramic, a large compressive in-plane strain and tensile OOP strain would be generated in the ceramic substrate and be transferred to TCFC film. The slope of the *M*-*H* loop decreases and leads to a larger anisotropy field, as it can be observed in Fig. 7.15 (b).

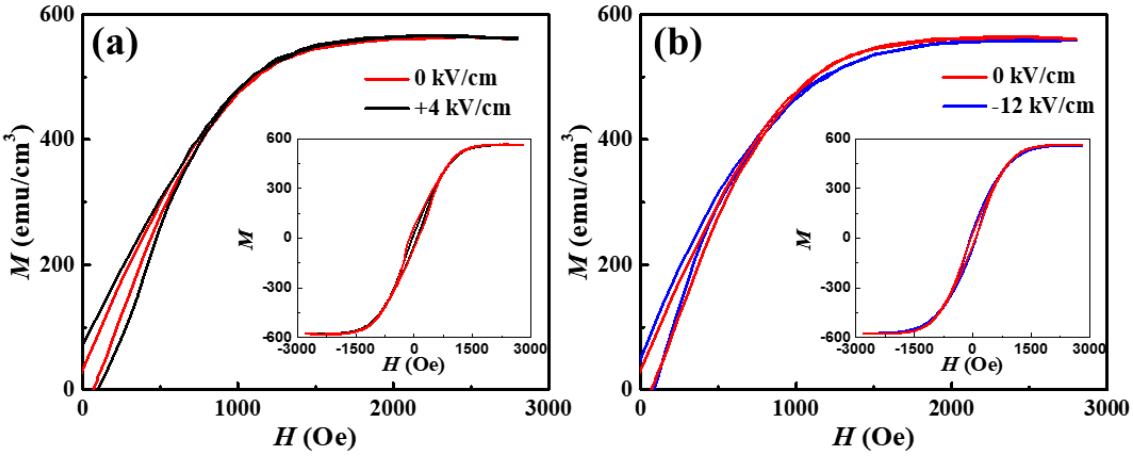

Figure 7.15 The *M-H* loops along the hard axis of TCFC/PMN-PZT/Au heterostructure under different magnetic fields.

Thus, under a specific magnetic field that is lower than the anisotropy field, the magnetization rises with tensile strain and reduces with compressive strain. The ideal *M-E* curves of TCFC/PMN-PZT/Au heterostructure should be in the inverted-butterfly shape if TCFC film is perfectly uniform and without defects.

It can be noticed that the *M-E* curves are in the inverted-butterfly shape when the magnetic field is higher than 800 Oe in Fig. 7.13, which is in accordance with the ideal deduction. However, here are some issues that the ideal model cannot explain:

a). The double magnetization peaks around E_C;

b). The appearance of direct butterfly-like *M-E* curves when the magnetic field is lower than 800 Oe;

c). The inverse process of the butterfly *M-E* curves.

As it is mentioned in Chapter 4, the surface of ceramic substrates is uneven, and many holes present. The diameter of the holes can be tens of micrometers, while the thickness of TCFC film is only 200 nm. Some parts of the TCFC film can be deposited into the holes of ceramic substrates. Thus the film is not exactly on the same plane. The magnetic anisotropy of different parts of TCFC film on different planes can lead to a complicated and mixed effect. As a result, the TCFC film is not perfect; it exhibits large remnant magnetization and non-zero H_C along the hard axis. The hysteresis part, which

appears when the magnetic field is lower than 800 Oe in Fig. 7.15, is the reason for the issues listed above. Since ceramic is polycrystalline, it consists of many different oriented grains. It is challenging to bring out a model to simulate the ME coupling effect in this complex system. However, a hypothesis is given above to explain the wired phenomena in TCFC/PMN-PZT/Au heterostructure.

The ΔM and CME coefficient is calculated and given in Fig. 7.16. The peaks of the CME coefficient always occur around the E_C of PMN-PZT ceramic, where the large strain presents. The quick change of E-field induced strain results in sharp magnetization change and leads to a large α_{CME} around the E_C of PMN-PZT.

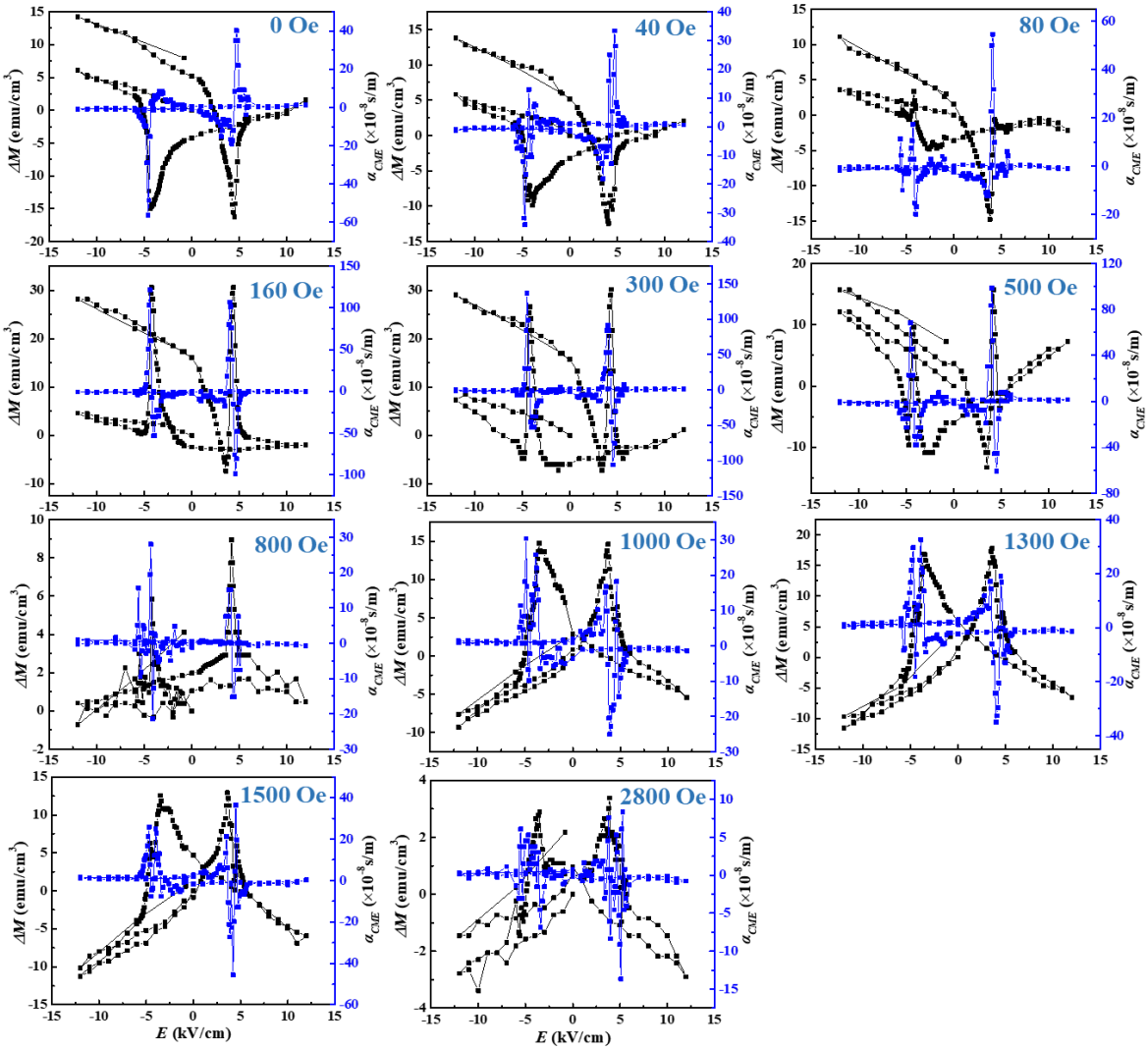

Figure 7.16 The ΔM–E and α_{CME}–E curves of TCFC/PMN-PZT/Au heterostructure along the hard axis at 0, 40, 80, 160, 300, 500, 800, 1000, 1300, 1500 and 2800 Oe.

The maximum of the CME coefficient under the specific magnetic field can be reached around the E_C of PMN-PZT. Figure 7.17 shows the value of the α_{max} versus bias magnetic field. With the bias magnetic field increasing, the α_{max} firstly decreases and then increases. The maximum of α_{max} is reached under a bias magnetic field of 300 Oe with a significant value of 136.6 $\times 10^{-8}$ s/m. At 300 Oe, the unfinished inverse of *the M-E* curve at E_C of PMN-PZT accounts for the significant CME coefficient. As the bias magnetic field further rises, the α_{max} reduces quickly and is lower than 50 $\times 10^{-8}$ s/m until H = 2800 Oe. It is necessary to point out that, the α_{max} can reach 56.2 $\times 10^{-8}$ s/m with an absence of the magnetic field.

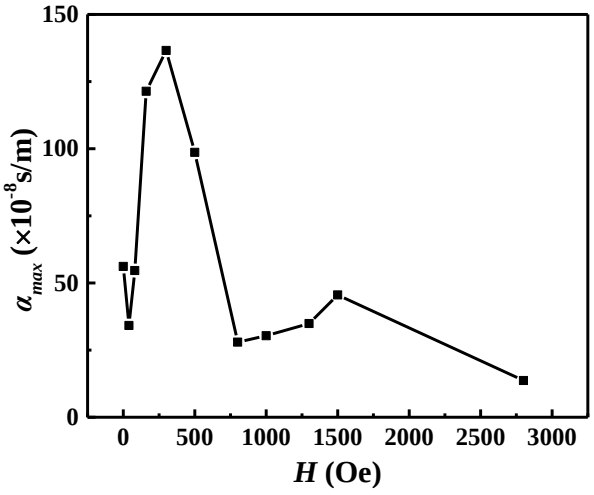

Figure 7.17 The α_{max}-*H* curve along the hard axis of TCFC/PMN-PZT/Au heterostructure.

7.3.2 CME Effect along Easy Axis

Figure 7.18 shows the *M-H* loops along the easy axis of TCFC/PMN-PZT/Au heterostructure under different electric fields. With an application of the electric field of 4 kV/cm, the maximum in-plane strain can be generated in PMN-PZT ceramic, but the large tensile strain did not lead to a distinct change in *M-H* loops. The inset shows minor variations in H_C, but the variation is too small. The highly intrinsic crystallographic orientation in the magnetic field of TCFC makes it difficult to induce the magnetic moment rotation or motion by strain. The strain-induced magnetization variations are almost forbidden along the easy axis. Thus it is difficult to realize the CME effect along the easy axis in TCFC/PMN-PZT/Au heterostructure.

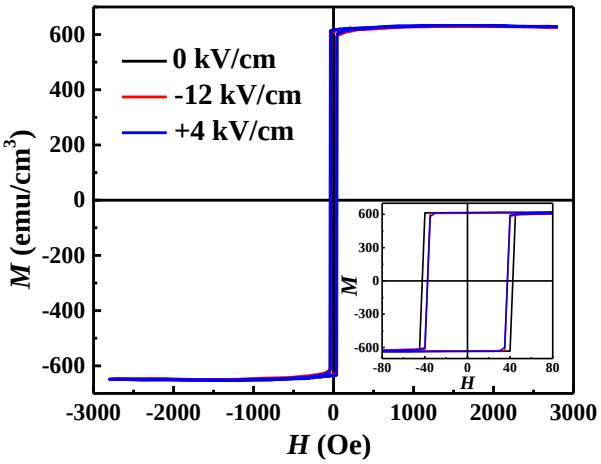

Figure 7.18 The *M-H* loops along the easy axis of TCFC/PMN-PZT/Au heterostructure under different electric fields.

7.3.3 CME Effect along OOP Direction

Figure 7.19 shows the *M-H* loops along the OOP direction of TCFC/PMN-PZT/Au heterostructure under different electric fields. With an application of different electric fields, the linear-like *M-H* loops vary with the *E*-induced strain. To reveal the relationship between the slope of *M-H* loops and the electric field, a linear fitting of *M-H* loops has been done, as given in Fig. 7.20 (a). Then the fitting slope of *M-H* loops versus the electric field curve can be carried out in Fig. 7.20 (b).

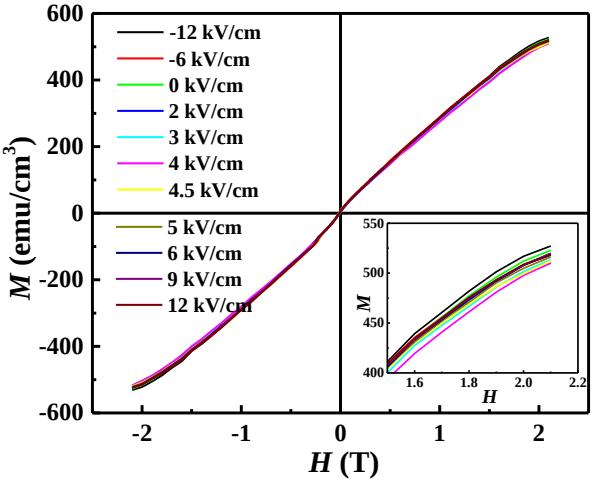

Figure 7.19 The *M-H* loops along the OOP direction of TCFC/PMN-PZT/Au heterostructure under different electric fields.

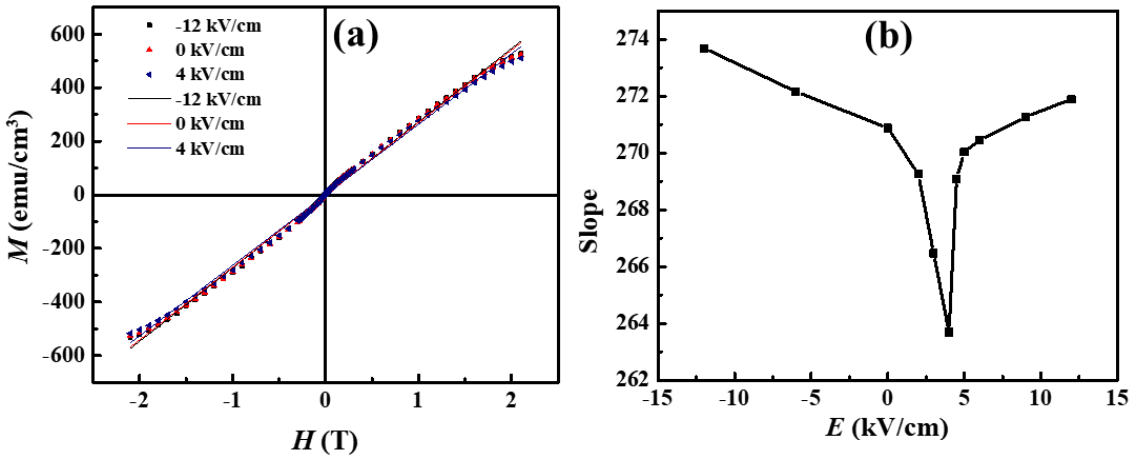

Figure 7.20 (a) The *M-H* loops and linear fitted under different electric fields, and (b) the slope of fitted lines versus electric fields along the OOP direction of TCFC/PMN-PZT/Au heterostructure.

The slope of *M-H* loops changes implies the transformation of magnetic anisotropy. In Fig. 20 (b), the slope vs. *E* curve is in the similar shape of *S-E* curves of PMN-PZT, once again revealing the strain-mediated magnetic anisotropy transformation along the OOP direction. When there is a tensile OOP strain generated in PMN-PZT, the slope of *M-H* loops increases, indicating that the anisotropy axis tilts to OOP direction. While a compressive OOP strain is generated, the slope reduces, and the anisotropy axis deviates from the OOP direction.

As a result of *E*-induced anisotropy transformation, the *E*-field controlled magnetization variations can be observed along the OOP direction. Figure 7.21 shows the *M-E* curves of TCFC/PMN-PZT/Au heterostructure at 5000 and 15000 Oe. The typical butterfly-like *M-E* curves can be well observed.

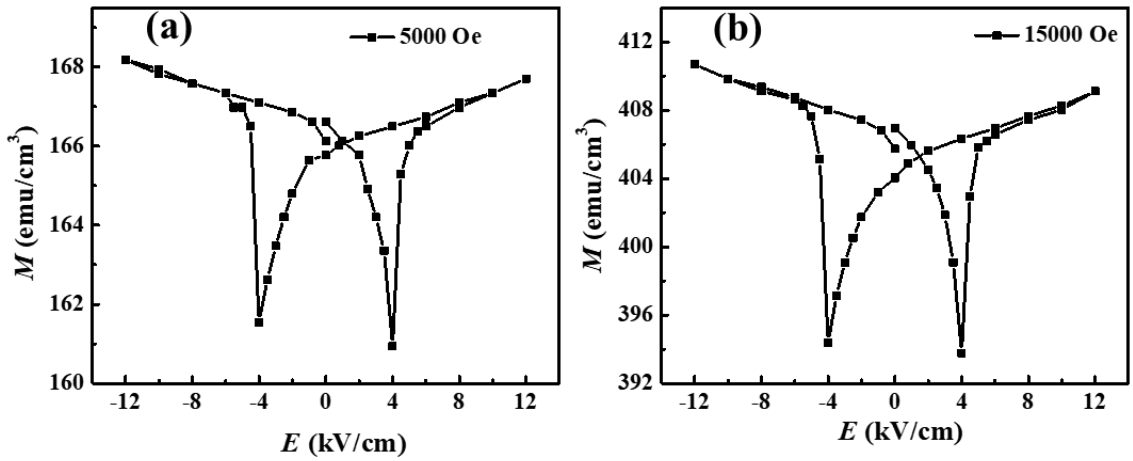

Figure 7.21 The *M-E* curves along the OOP direction of TCFC/PMN-PZT/Au heterostructure (a) at 5000 Oe and (b) at 15000 Oe.

To evaluate the CME coupling effect along OOP direction, the $\Delta M/M_0$-E and α_{CME}-E curves of TCFC/PMN-PZT/Au heterostructure at 5000 and 15000 Oe are given in Fig. 7.22. The large $\Delta M/M$ is reached at E_C of PMN-PZT with a value of ~3% at 5000 and 15000 Oe, and the CME coefficient peaks E_C as a result. The peak value of α_{CME} at 5000 Oe is 6.6 $\times 10^{-8}$ s/m, while it is 16.0 $\times 10^{-8}$ s/m at 15000 Oe.

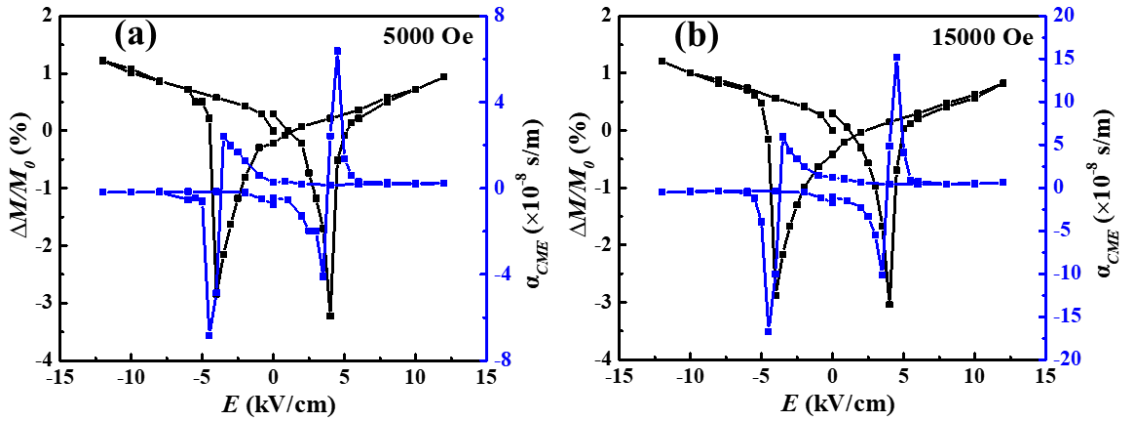

Figure 7.22 The $\Delta M/M_0$-E and α_{CME}-E curves along the OOP direction of TCFC/PMN-PZT/Au heterostructure (a) at 5000 Oe and (b) at 15000 Oe.

7.3.4 Summary

In this part of the work, the [(TbCo2)/(FeCo)]20/PMN-PZT/Au heterostructure has been prepared, and the *E*-field induced magnetism along different axes has been studied. The *M-H* loops under different electric fields and *E*-field controlled magnetization variations along the hard axis of TCFC film have been investigated. The *M-E* curves are in accord with the butterfly *S-E* curve of the PMN-PZT substrate. An inverse process of *M-E* curves happens with the bias magnetic field increasing, and double magnetization peaks occur around the E_C of PMN-PZT substrate. The appearances of the inverse transition of *M-E* curves and double peaks in this heterostructure may be due to the uneven distribution of TCFC film on a ceramic substrate with inevitable holes. The maximum of α_{CME} is at a substantial value of 136.6 $\times 10^{-8}$ s/m with a bias magnetic field of 300 Oe. The weird inverse process of *M-E* curves has provided a possibility to reach a substantial CME coupling effect. Along the easy axis of TCFC film, the *E*-induced magnetization variation is suppressed by the highly intrinsic

crystallographic orientation with a magnetic field. Along OOP direction, clear evidence of *E*-field induced magnetic anisotropy transformation has been observed, i.e., the slope shifts of *M-H* loops with the electric field. The curve of slope versus electric field agrees with the strain evolution of PMN-PZT ceramic under an electric field. This is the direct evidence of the occurrence of strain-mediated magnetic anisotropy transformation in TCFC/PMN-PZT/Au heterostructure. The *E*-field controlled magnetization variations and CME coefficient along the OOP direction have also been demonstrated.

7.4 Conclusions

The rare-earth Tb modified 3d-transition alloys $(TbCo_2)/(FeCo)$ is used to couple with PLZST and PMN-PZT ceramic substrates in this part. The $[(TbCo_2)/(FeCo)]_{20}$/PLZST/Au and $[(TbCo_2)/(FeCo)]_{20}$/PMN-PZT/Au heterostructures have been fabricated. To explore the CME coupling effect along different orientations, the TCFC films are prepared to exhibit mutually perpendicular in-plane easy axis and hard axis. The *E*-induced magnetism along easy axis, hard axis, and OOP direction have been discussed.

1. Along the easy axis of TCFC film, the *E*-induced magnetization variation is suppressed by the highly intrinsic crystallographic orientation with the magnetic field.

2. Along the hard axis, a reverse process of *M-E* curves appears with the bias magnetic field increasing. The appearances of the inverse transition of *M-E* curves may be due to the uneven distribution of TCFC film on a ceramic substrate with inevitable holes. In TCFC/PLZST/Au, the maximum of $\Delta M/M_0$ can reach -9.8% with an absence of a magnetic field, and the α_{CME} is at the negative maximum of -10.3×10^{-8} s/m at the same time. The positive maximum of α_{CME} is at 500 Oe with a value of 12.7×10^{-8} s/m. In TCFC/PMN-PZT/Au, the maximum of α_{CME} can reach a large value of 136.6×10^{-8} s/m with a bias magnetic field of 300 Oe.

3. Along OOP direction, the *E*-induced magnetism is not visible in TCFC/PLZST/Au heterostructure, which can be attributed to that the energy of *E*-induced strain in PLZST is not enough to deflect the magnetic moment from in-plane to OOP direction. However, in TCFC/PMN-PZT/Au heterostructure, clear evidence of *E*-field induced magnetic anisotropy transformation has been observed, i.e., the slope

shifts of *M-H* loops with the electric field. The curve of slope versus electric field agrees with the strain evolution of PMN-PZT ceramic under an electric field.

8 YIG/AFE and YIG/FE Heterostructures in Full Thin-Film Form

Extensive investigations have been devoted to the research of multiferroic composites in full thin-film in past years with the development of integration and miniaturization.[77,85,93,137–139] Compared with bulk ME composites, multiferroic thin films have unique superiorities. The multiferroic thin films show great potential in integrated magnetic/electric devices, such as sensors, microelectromechanical system, high-density memories, and spintronics.[137,139–141,93]

In the previous parts, the CME coupling effect has been demonstrated in AFE- and FE-based bulk heterostructures. The large thickness of AFE ceramic substrates requires an application of high voltage to reach the switching field, which is a big challenge for future applications. Thus, it is necessary to develop AFE- and FE-based multiferroic films and compare their performance in thin-film form. The ferrite YIG films are used to deposit on AFE and FE films for their good coupling effect.

8.1 Preparation of YIG/AFE and YIG/FE Heterostructures in Full-Thin-Film Form

In these heterostructures, the $PbZrO_3$ (PZ) AFE film Pb(Zr, Ti)O_3 (PZT) FE film were grown on SiO_2/Si substrate where the $LaNiO_3$ (LNO) film was introduced as the bottom electrodes. Then Pt top electrodes and the following YIG films were deposited. The YIG/Pt/PZ/LNO/SiO_2/Si and YIG/Pt/PZT/LNO/SiO_2/Si heterostructure in full thin-film form can be prepared.

8.1.1 LNO film Growth

The LNO electrode layer was prepared by using an "Addax" RF sputtering system with an LNO ceramic target. The sputtering condition and annealing process of LNO films have been explored by several researchers and well known in the group.[142–146] The details of the sputtering condition are given in Table 8.1.

Table 8.1 Sputtering parameters of LNO films

Sputtering Condition	LNO
Vacuum (Pa)	$< 3 \times 10^{-4}$
Power (W)	100
Temperature (℃)	450
Atmosphere	O_2/Ar=1/4
Pressure (Pa)	1

After the deposition, the samples were annealed in a furnace to be crystallized. The annealing process is given in Table 8.2.

Table 8.2 Annealing parameters of LNO films

Annealing Condition	LNO
Heating Rate (℃/min)	2
Annealing (℃)	750
Duration (min)	60
Cooling Rate (℃/min)	1
Atmosphere	Air

Figure 8.1 shows the XRD patterns of LNO films on SiO_2/Si substrates, and it can be observed that the LNO films can be well crystallized on SiO_2/Si substrates at 750 ℃. The LNO film is highly (100)-oriented, which will favor the (100)-oriented films on the top.

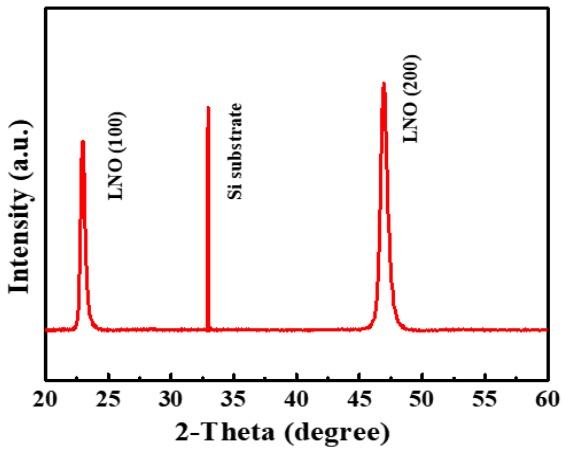

Figure 8.1 The XRD patterns of LNO films on SiO_2/Si substrates.

8.1.2 Preparation of Pt/PZ/LNO/SiO_2/Si ME Heterostructures

The PZ film was prepared by our cooperation group with SICCAS and in particular with Prof. Wang Genshui's team, through a chemical solution deposition process. The $Pb(CH_3COO)_2 \cdot 3H_2O$ with an excess of 20 mol.% and zirconium (IV) n-propoxide $Zr[O(CH_2)_2CH_3]_4$ (70% wt% in n-propanol) were dissolved in glacial acetic acid solvent (>99.5%) with acetylacetone chelating agent. The solution concentration was adjusted to 0.3 mol/L by adding acetic acid. Then solution was refluxed at 80 °C for 1 hour. The PZ layer was spin-coated and then pyrolyzed at 350 °C and at 600 °C respectively. These steps were repeated for six times to achieve the thickness of 500 nm. Finally, the films were annealed at 750 °C in Rapid Temperature Annealing. Usually the annealing temperature of PZ films is 700 °C, here a high annealing temperature of 750 °C is to adapt to the following annealing process of YIG films.

The PZ film with a thickness of 500 nm shows good crystallization on LNO/ SiO_2/Si substrates, as given in Fig. 8.2. The highly (100)-oriented PZ films are formed with no impurity phases detected.

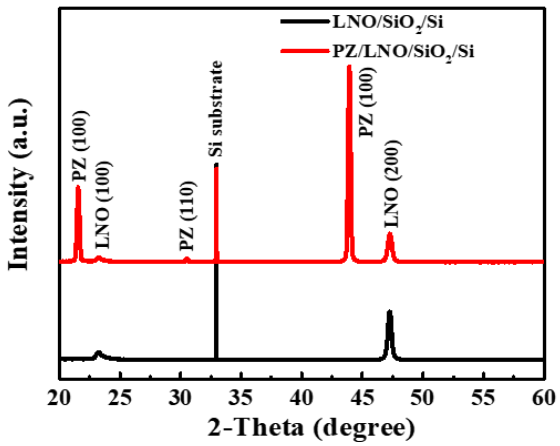

Figure 8.2 The XRD patterns of PZ films on LNO/SiO_2/Si substrates.

The Pt electrodes with good conductivity were deposited on PZ with a thickness of 80nm by DC magnetron sputtering. The masks were used in the deposition to constrain the diameter of Pt electrodes (450 μm), as illustrated in Fig. 8.3.

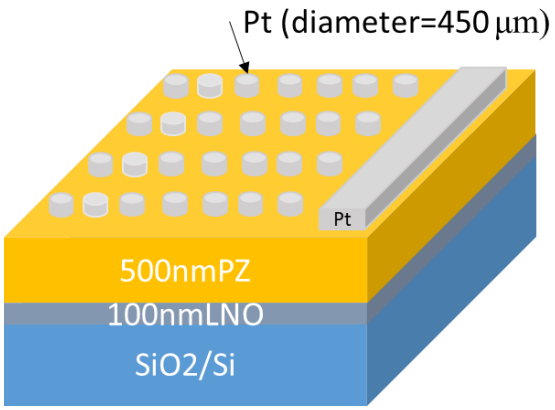

Figure 8.3 Schematic of Pt/PZ/LNO/SiO_2/Si heterostructure.

With the electrodes, the electrical properties of Pt/PZ/LNO/SiO_2/Si heterostructure can be drawn out. In Fig. 8.4 (a), the PZ film presents typical double *P-E* loops with a switching field of 380 kV/cm. Figure 8.4 (b) illustrates four dielectric constant (ε_r) peaks, as well as four *tanδ* peaks, which are the typical characteristics of AFE materials.

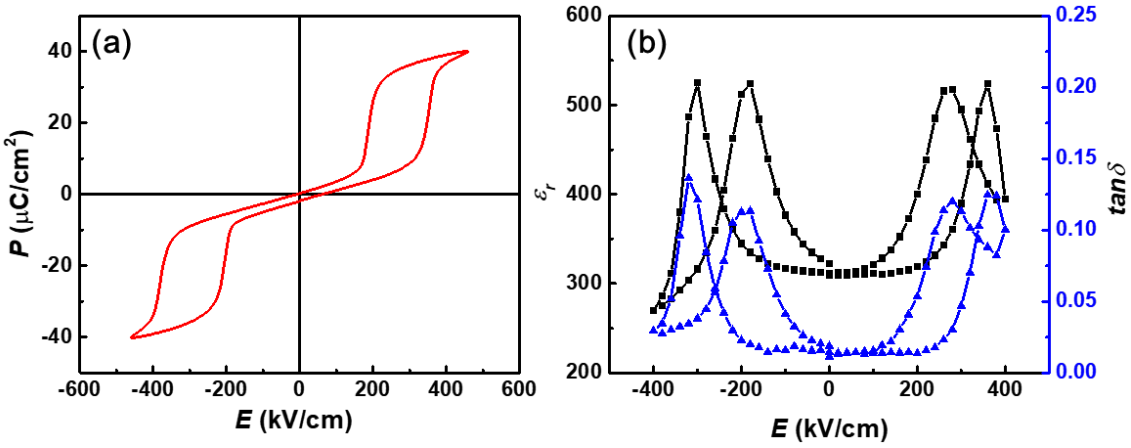

Figure 8.4 (a) The *P-E* loops and (b) ε_r-*E* and *tanδ*-*E* curves of Pt/PZ/LNO/SiO_2/Si heterostructure.

8.1.3 Preparation of Pt/PZT/LNO/SiO_2/Si ME Heterostructures

The PZT film with a thickness of 500 nm was prepared by using an "Addax" RF sputtering system with a powder target in a composition of $PbZr_{0.53}Ti_{0.47}O_3$. The target was fabricated with an excess of 20% Pb to compensate for the deficient of Pb during the deposition and annealing process. The sputtering condition and the annealing

process of PZT films have been explored in the group.[143,147,148] The details of the sputtering condition are given in Table 8.3.

Table 8.3 Sputtering parameters of PZT films

Sputtering Condition	PZT
Vacuum (Pa)	$< 3 \times 10^{-4}$
Power (W)	100
Temperature (℃)	RT
Atmosphere	Ar
Pressure (Pa)	1

After the deposition, the samples were annealed in a furnace to be crystallized. The annealing process is given in Table 8.4. Usually, the annealing temperature of PZT films is 650°C. In this work, we have used 750°C for the simple reason that the YIG films must be annealing at 750°C. We have systematically verified that the structure of PZT is not affected by this high annealing temperature, and in particular no second phase (lead deficient) appears, as given in Figure 8.5.

Table 8.4 Annealing parameters of PZT films

Annealing Condition	PZT
Heating Rate (℃/min)	2
Annealing (℃)	750
Duration (min)	30
Cooling Rate (℃/min)	3
Atmosphere	Air

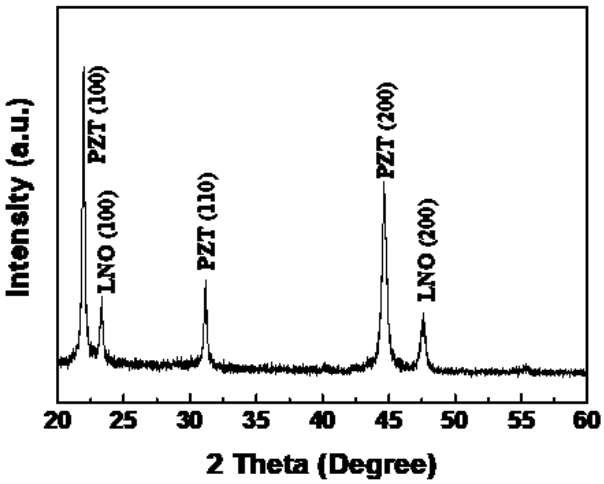

Figure 8.5 The XRD patterns of PZT films on LNO/SiO_2/Si substrates.

The Pt top electrodes were also deposited on PZT/LNO/SiO_2/Si with a diameter of 450 μm, as given in Fig. 8.6.

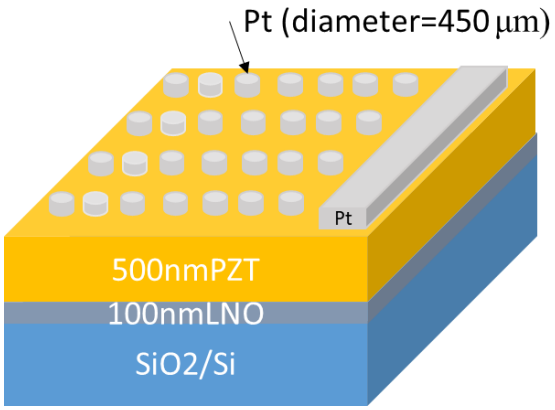

Figure 8.6 Schematic of Pt/PZT/LNO/SiO_2/Si heterostructure.

Figure 8.7 shows the electrical properties of Pt/PZT/LNO/SiO_2/Si heterostructure. The typical ferroelectric hysteresis *P-E* loop is well observed in Fig. 8.7 (a), indicating the ferroelectricity of PZT films. The ε_r-*E* and *tanδ-E* curves of Pt/PZT/LNO/SiO_2/Si heterostructure are also demonstrated the ferroelectric properties of PZT films.

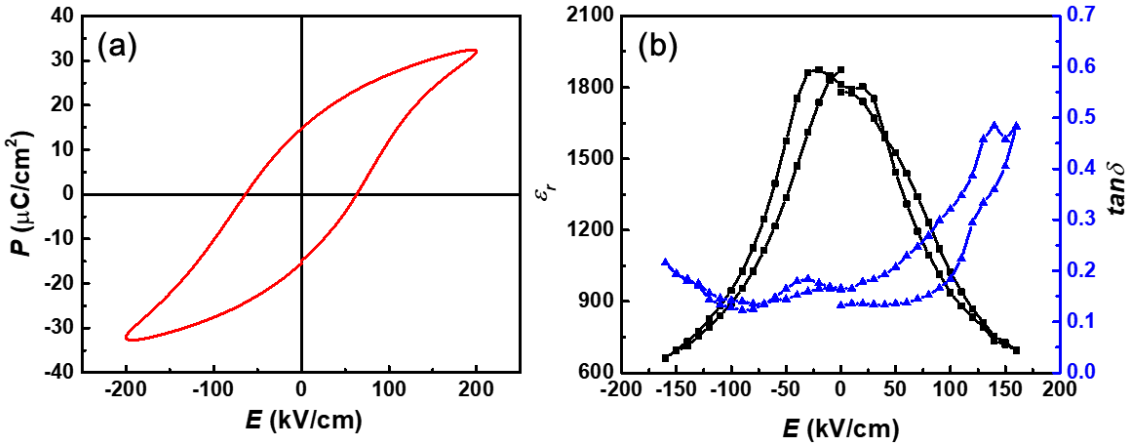

Figure 8.7 (a) The *P*-*E* loops and (b) ε_r-*E* and *tanδ*-*E* curves of Pt/PZT/LNO/SiO_2/Si heterostructure.

8.1.4 Preparation of YIG/Pt/PZ (PZT)/LNO/SiO_2/Si ME Heterostructures

As the Pt/PZ/LNO/SiO_2/Si and Pt/PZT/LNO/SiO_2/Si heterostructures were well prepared and presented good antiferroelectricity or ferroelectricity, the YIG films were deposited on Pt/PZ/LNO/SiO_2/Si and Pt/PZT/LNO/SiO_2/Si heterostructures by the same process given in Chapter 6. The masks were also used during the deposition to constrain the diameter of YIG films in 250 μm. The design of the masks can make the YIG films are precisely on the top of Pt electrodes. The final composite heterostructure is illustrated in Fig. 8.8. The thickness of the YIG film is 400 nm.

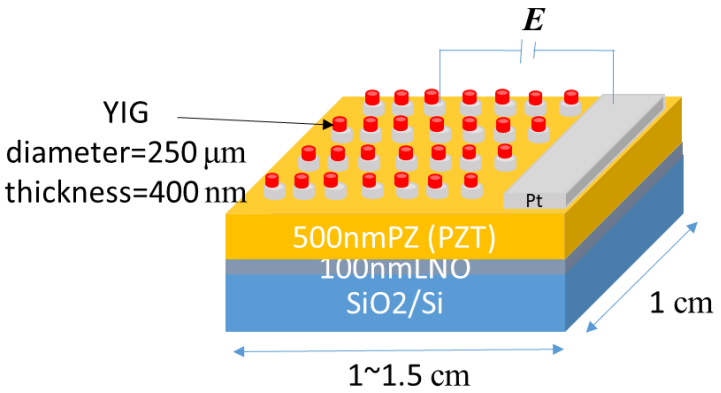

Figure 8.8 Schematic of Pt/PZ/LNO/SiO_2/Si heterostructure.

The phase structure and crystallization of YIG/Pt/PZ/LNO and YIG/Pt/PZ/LNO multilayers were confirmed by X-ray diffractio. Figure 8.9 depicts the XRD patterns of

YIG/Pt/PZ/LNO/SiO_2/Si and YIG/Pt/PZ/LNO/SiO2/Si heterostructures. The XRD analysis confirms the expected phase structures for all the materials. The origin of the various peaks is as labeled. The YIG film is on the top but with a low quantity, so the diffraction peaks of YIG thin films are of much lower intensity when compared to the peaks of Pt and PZ or PZT films.

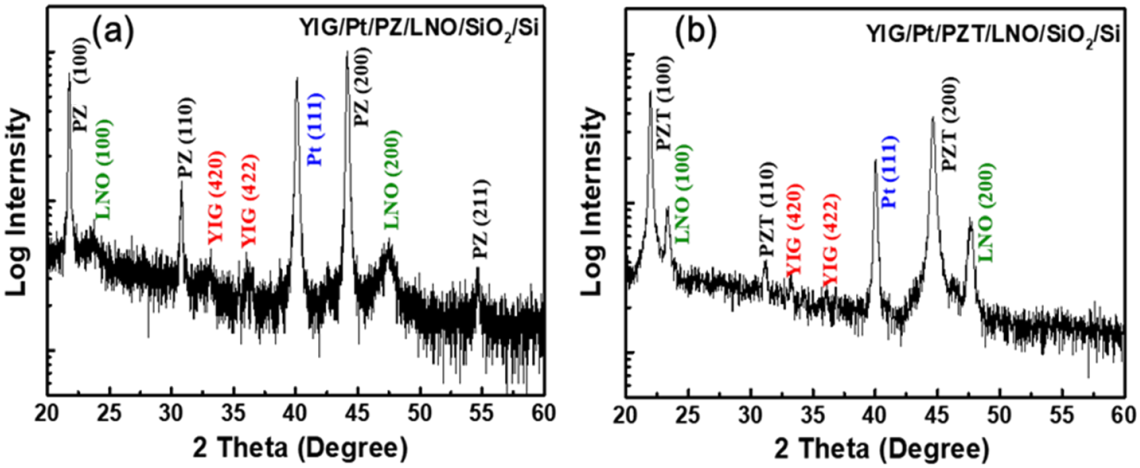

Figure 8.9 XRD patterns of (a) YIG/Pt/PZ/LNO/SiO_2/Si and (b) YIG/Pt/PZT/LNO/SiO_2/Si heterostructures.

8.2 Results and Discussions

8.2.1 YIG/Pt/PZ/LNO/SiO_2/Si Heterostructure

(1) Macroscopic Magnetic Properties

The in-plane *M-H* loops of YIG films on SiO_2/Si substrate and on Pt/PZ/LNO/SiO_2/Si heterostructure are given in Fig. 8.10 as a comparison. It can be seen that the YIG films on Pt/PZ/LNO/SiO_2/Si heterostructure also present good magnetic properties when compared with YIG film on SiO_2/Si substrate. The magnetic parameters are given in Table 8.5. The coercive field of YIG films on different substrates are similar, but the remnant magnetization and saturated magnetization of YIG film on Pt/PZ/LNO/SiO_2/Si heterostructure are lower than YIG film on SiO_2/Si substrate.

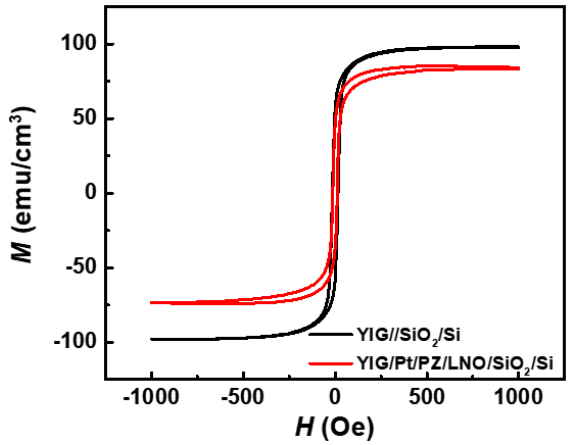

Figure 8.10 In-plane *M-H* loops of YIG/SiO_2/Si and YIG/Pt/PZ/LNO/SiO_2/Si heterostructures.

Table 8.5 Magnetic parameters of YIG films on SiO_2/Si substrate and on Pt/PZ/LNO/SiO_2/Si heterostructure

	H_C (Oe)	Mr (emu/cm^3)	M_S (emu/cm^3)
YIG/SiO_2/Si	15.0	58.1	98
YIG/Pt/PZ/LNO/SiO_2/Si	13.6	41.5	84

(2) Microscopic Magnetic Properties

Magnetic domain pattern of YIG films was characterized by means of the lift-mode of the magnetic force microscopy (MFM) technique working under environmental conditions with a commercial microscope (MultiMode, Bruker, UCCS group Univ. Artois). A Co-coated tip (Nanosensors PPPMFMR probe, coercivity of ~300 Oe) with magnetization direction along its axis and normal to the film surface was used as the nanometric probe. An external voltage supply was equipped with MFM system to apply voltage to the sample. The schematic of the measurement system is given in Fig. 8.11 (a). Another two probes (Suss Microtec Cascade PH110) were attached to the Pt electrodes, as illustrated in Fig. 8.11 (b), and then connected to the voltage supply. In this way, the magnetic domain patterns of YIG films can be measured

with an electric field applied to PZ or PZT films at the same time. Thus, we can characterize the magnetic domain movements mediated by electric-field-induced strain.

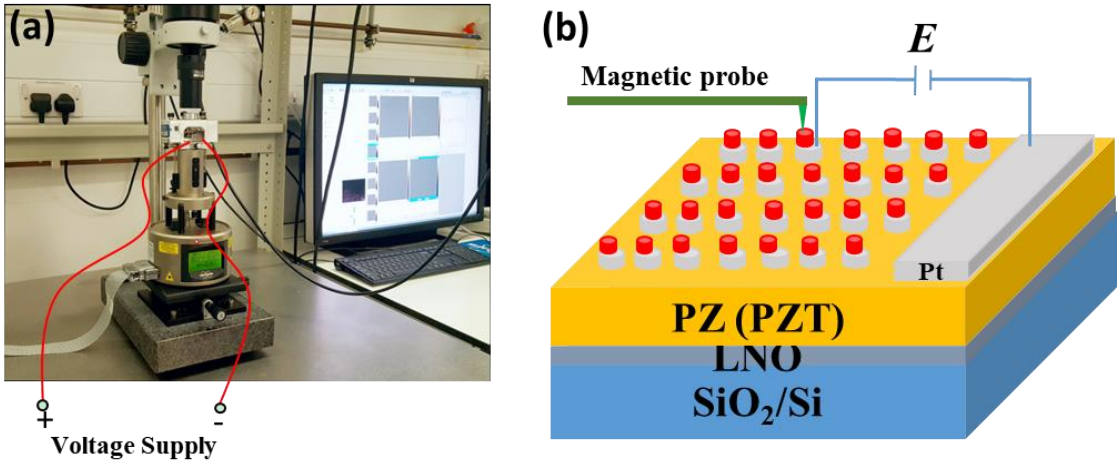

Figure 8.11 (a) The MFM system, and (b) schematic of the YIG/Pt/PZ/LNO/SiO_2/Si heterostructure with probes.

The AFM surface morphology of YIG films on SiO_2/Si substrate in Figure 8.12 (a). A dense granular-like surface was observed. The magnetic domains of YIG films on SiO_2/Si substrate were also locally probed by MFM technique. As shown in Figure 8.12 (b), where a maze shape is obtained for domains, with yellow/clear and blue/dark contrasts corresponding to upward (repulsive interaction) and downward (attractive interaction) OOP magnetization, respectively. Such complex irregular domain pattern was already explained by the similar magnetic anisotropy and magnetostatic energies in the film.[34,149,150] Besides, no-correlation is observed between AFM and MFM images confirming the contrasts seen on MFM image are exclusively due to the magnetic interaction.

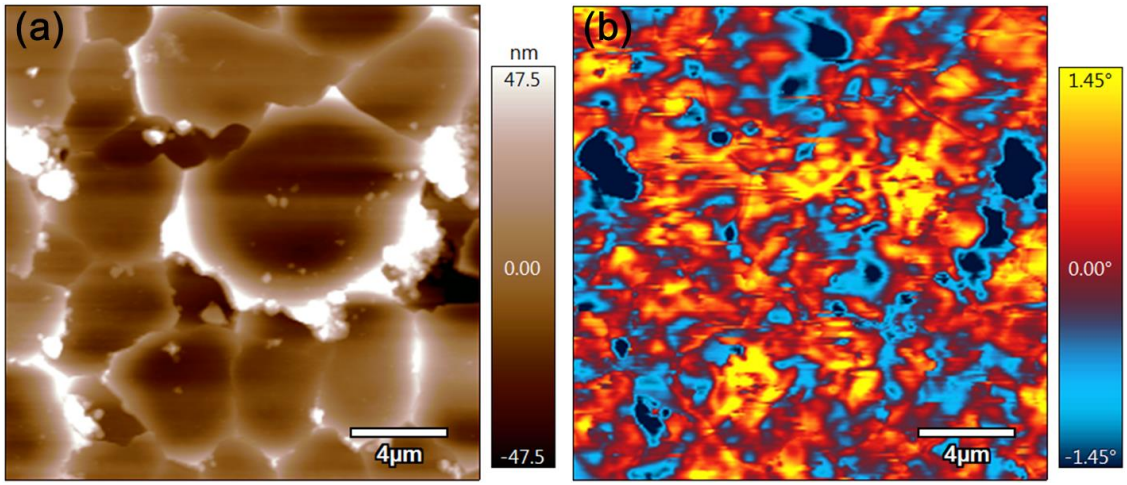

Figure 8.12 (a) AFM surface morphology and (b) MFM image of YIG films on SiO_2/Si substrate.

But when we try to characterize the MFM images of YIG films on Pt/PZ/LNO/SiO_2/Si heterostructure, it didn't succeed. It may be due to the following reasons:

1). The OOP magnetic response of YIG films are too weak to be detected by MFM system. As we have demonstrated in Chapter 6, the polycrystalline YIG films present an "easy plane" in the plane, and the OOP magnetization can reach the saturation under the application of a very high magnetic field. In Chapter 6.2, the in-plane saturation magnetic field of YIG films is 200 Oe, while the OOP saturation magnetic field is 1500 Oe. Thus, the magnetic response of YIG film is too weak along OOP direction.

2). During the MFM measurements, a proper distance between the MFM tip and the surface of YIG films is necessary to reach a good resolution of AFM image and MFM image. Since the OOP magnetic response of YIG films is weak, a very low distance is needed to obtain the magnetic response. However, if the MFM tip is too close to the surface of YIG films, the morphology signal would be strong enough to cover up the magnetic signal. A low distance of 15 nm and 10 nm has been tried, but we couldn't obtain distinct magnetic responses.

3). The quality of PZ films has an influence on the quality of YIG films. The multi-step preparation process may lead to some side effect, especially the multiple annealing process have an effect on PZ film. The Pb is a volatile constituent, and the volatilization

happens at high temperature. The volatilization process not only lead to Pb loss in PZ film, but also cause some Pb diffusion into other layers, even though it is not detected by XRD system.

Even with the application of electric field, the variations of magnetic response is still a challenge. As it has been presented in Chapter 6, the *E*-field induced magnetization is very weak along OOP direction.

8.2.2 YIG/Pt/PZT/LNO/SiO_2/Si Heterostructure

The characterization of MFM image in YIG/Pt/PZT/LNO/SiO_2/Si heterostructure has also met the same challenge as YIG/Pt/PZ/LNO/SiO_2/Si.

8.3 Conclusions

The ME composites in thin-film form were fabricated in this part - YIG/Pt/PZ/LNO/SiO_2/Si and YIG/Pt/PZT/LNO/SiO_2/Si heterostructures. The PZ and PZT films have shown good electrical properties, but the MFM image cannot be successfully characterized in this case. The in-plane anisotropy field of YIG films has constrained the detectable magnetic signal through MFM system along OOP direction. The multiple annealing process of PZ and PZT films may also has a side effect because of Pb volatilization. In addition, the CME coupling effect of polycrystalline YIG is weak along OOP direction, which would also be a challenge for future measurements.

Therefore, this part of work has pointed out the way to fabricate CME composites in thin-film form. A good choice of ferromagnetic phases should be the films with a strong magnetic response along OOP direction and low annealing temperature or no annealing process needed, such as 3d-transition metals (Fe, Co, and Ni) and alloys (Terfenol-D, Galfenol).

9 Summary and Future Work

9.1 Summary

This dissertation reports the results of the voltage control of magnetism that occurred between different ferro-/ferri-magnetic and antiferro-/ferro-electric components through interface elastic strain transformation.

First, the PMN-PZT FE and PLZST AFE ceramic substrates have been prepared, and the detailed characterizations have been performed. The well-polished substrates can reach a low average roughness (< 20 nm) despite the inevitable defects in ceramics. The E_C of PMN-PZT ceramics is as low as 4.2 kV/cm, while the *E*-induced in-plane and out-of-plane strain can reach -0.27% and 0.08% at E_C, respectively. The AFE-FE switching field of PLZST is 5 kV/mm with a maximum strain of 0.2 %.

Second, the formation of NMG/PLZST heterostructure has been performed, and the *E*-field controlled magnetization switching in an AFE-based multiferroic composite has been firstly reported. The evolution of ($\Delta M/M_0$) as a function of *E* is in good agreement with the ceramic strain evolution and secondly that the maximum $\Delta M/M_0$ variation, which attains a maximum value of 15%, is reached at 0 Oe. Even the CME coefficient is small due to the bad quality of NMG film on PLZST ceramic, and these results reveal the great potential of AFE materials in the CME coupling effect for the first time.

Third, we investigated the *E*-field control of magnetism in YIG/Pt/PLZST/Pt, and YIG/Pt/PMN-PZT/Pt heterostructures, wherein the in-plane and out-of-plane CME coupling effects were explored. In these two heterostructures, the *E*-field induced strain is transferred to YIG film and leads to a magnetic anisotropy transformation, which results in the manipulation of magnetism. Because of the different strain evolution of PLZST and PMN-PZT substrates under the electric field, the CME coupling effect in YIG/Pt/PLZST/Pt and YIG/Pt/PMN-PZT/Pt heterostructures shows some differences. The considerable *E*-induced phase transition strain in PLZST substrate leads to maximum in-plane α_{CME} (11.6×10^{-8} s/m) at 0 Oe and a maximum of in-plane $\Delta\chi/\chi_0$ (33%) with a low magnetic field of 10 Oe in YIG/Pt/PLZST/Pt heterostructure. The in-

plane CME coefficient in YIG/Pt/PMN-PZT/Pt heterostructure can reach 16.95 × 10^{-8} s/m in the absence of bias magnetic field at E_C of PMN-PZT ceramic, and the maximum of in-plane CME coefficient (18.15 × 10^{-8} s/m) is observed under the magnetic field of 25 Oe. When the application of electric field amplitude is close E_C of PMN-PZT, the voltage-impulse reversible magnetization switching and the linear *E*-tunable susceptibility change can be realized in YIG/Pt/PMN-PZT/Pt heterostructures.

Forth, the CME coupling effect of the rare-earth Tb modified 3d-transition alloys ($TbCo_2$)/(FeCo) coupled with PLZST and PMN-PZT ceramic substrates has also been revealed. The $[(TbCo_2)/(FeCo)]_{20}$/PLZST/Au and $[(TbCo_2)/(FeCo)]_{20}$/PMN-PZT/Au heterostructures have been fabricated, and the CME coupling effect along different directions have been discussed. The *E*-induced magnetization variation is suppressed along the easy axis of TCFC film by the highly intrinsic crystallographic orientation with the magnetic field. Along the hard axis, a reverse process of *M*-*E* curves appears with the bias magnetic field increasing. The appearances of the inverse transition of *M*-*E* curves may be due to the uneven distribution of TCFC film on a ceramic substrate with inevitable holes. In TCFC/PLZST/Au, the maximum of $\Delta M/M_0$ can reach -9.8% with an absence of the magnetic field, and the α_{CME} is at the negative maximum of -10.3×10^{-8} s/m at the same time. The positive maximum of α_{CME} is at 500 Oe with a value of 12.7×10^{-8} s/m. In TCFC/PMN-PZT/Au, the maximum of α_{CME} can reach a significant value of 136.6 ×10^{-8} s/m with a bias magnetic field of 300 Oe. Along OOP direction, the *E*-field induced magnetism is not visible in TCFC/PLZST/Au heterostructure, which can be attributed to that the energy of *E*-field induced strain in PLZST is not enough to deflect the magnetic moment from in-plane to OOP direction. However, in TCFC/PMN-PZT/Au heterostructure, clear evidence of *E*-field induced magnetic anisotropy transformation has been observed, i.e., the slope shifts of *M*-*H* loops with the electric field. The curve of the slope versus electric field agrees with the strain evolution of PMN-PZT ceramic under the electric field.

Finally, we have explored the YIG/AFE and YIG/FE multiferroic heterostructure in thin-film form. The results indicate that a ferromagnetic phase with a strong magnetic response along OOP direction is needed for the MFM characterization to evaluate the ME performance of these structures.

9.2 Future Work

Despite the progress made in this dissertation, further work is needed to understand the AFE- and FE-based multiferroic heterostructures fully.

The following future work has been proposed:

1. A deeper study of TCFC/PLZST and TCFC/PMN-PZT heterostructures is needed. The theoretical simulation and local characterizations of magnetic response under certain magnetic and electric fields are necessary for us to understand the inverse of *M*-*E* curves.

2. In this thesis, the *E*-field induced magnetization switching and *E*-field tunable magnetic susceptibility have been demonstrated in different heterostructures. However, the *E*-field induced FMR shifts have not been done to compare the differences of CME coupling effect in AFE- and FE-based multiferroic heterostructures at high frequency.

3. In YIG/AFE and YIG/FE heterostructures, a follow-up study should investigate the influence of the thickness of the Pt electrode in the CME coupling effect. We have only shown the CME coupling effect in YIG/Pt/AFE/Pt and YIG/Pt/FE/Pt heterostructures, where the thickness of the Pt layer is 80 nm. A more detailed study of the interlayer thickness in the CME coupling effects and more widely, the interface effects should be carried out.

4. A subsequent study involving the fabrication of FM-AFE and FM-FE multiferroic films should be conducted and compared. The AFE- and FE-based multiferroic heterostructures in a thin-film form with differently-oriented AFE and FE films should be investigated, and therefore the CME coupling effect can be explored, which is showing potential in a variety of practical applications.

In closing, the current work suggests a variety of research scenarios—both in AFE- and FE-based multiferroic heterostructures and in the characterization of E-field controlled magnetic properties at static state. Based on the specific characteristics of each component, we can study the electrical, magnetic, and magnetoelectric properties of the self-assembled heterostructures, and more importantly, the comparison of AFE-

and FE-based CME coupling effects are given, which may hold promise for different multifunctional applications.

References

[1] J.M. Rondinelli, M. Stengel, N.A. Spaldin, Carrier-mediated magnetoelectricity in complex oxide heterostructures, Nature Nanotechnology. 3 (2008) 46–50. doi:10.1038/nnano.2007.412.

[2] S. Fusil, V. Garcia, A. Barthélémy, M. Bibes, Magnetoelectric devices for spintronics, Annual Review of Materials Research. 44 (2014) 91–116. doi:10.1146/annurev-matsci-070813-113315.

[3] M. Staruch, D.B. Gopman, Y.L. Iunin, R.D. Shull, S.F. Cheng, K. Bussmann, P. Finkel, Reversible strain control of magnetic anisotropy in magnetoelectric heterostructures at room temperature, Scientific Reports. 6 (2016). doi:10.1038/srep37429.

[4] W. Eerenstein, N.D. Mathur, J.F. Scott, Multiferroic and magnetoelectric materials, Nature. 442 (2006) 759–765. doi:10.1038/nature05023.

[5] A.B. Ustinov, G. Srinivasan, B.A. Kalinikos, Ferrite-ferroelectric hybrid wave phase shifters, Applied Physics Letters. 90 (2007) 031913. doi:10.1063/1.2432953.

[6] Y.K. Fetisov, G. Srinivasan, Electrically tunable ferrite-ferroelectric microwave delay lines, Applied Physics Letters. 87 (2005) 103502. doi:10.1063/1.2037860.

[7] M.M. Vopson, Fundamentals of multiferroic materials and their possible applications, Critical Reviews in Solid State and Materials Sciences. 40 (2015) 223–250. doi:10.1080/10408436.2014.992584.

[8] S. Priya, R. Islam, S. Dong, D. Viehland, Recent advancements in magnetoelectric particulate and laminate composites, Journal of Electroceramics. 19 (2007) 149–166. doi:10.1007/s10832-007-9042-5.

[9] J. Das, Y.-Y. Song, N. Mo, P. Krivosik, C.E. Patton, Electric-field-tunable low loss multiferroic ferrimagnetic-ferroelectric heterostructures, Advanced Materials. 21 (2009) 2045–2049. doi:10.1002/adma.200803376.

[10] C. Israel, N.D. Mathur, J.F. Scott, A one-cent room-temperature magnetoelectric sensor, Nature Materials. 7 (2008) 93–94. doi:10.1038/nmat2106.

[11] C. Ederer, N.A. Spaldin, Weak ferromagnetism and magnetoelectric coupling in bismuth ferrite, Phys. Rev. B. 71 (2005) 060401. doi:10.1103/PhysRevB.71.060401.

[12] G. Lawes, G. Srinivasan, Introduction to magnetoelectric coupling and multiferroic films, J. Phys. D: Appl. Phys. 44 (2011) 243001. doi:10.1088/0022-3727/44/24/243001.

[13] G. Catalan, J.F. Scott, Physics and applications of bismuth ferrite, Advanced Materials. 21 (2018) 2463–2485. doi:10.1002/adma.200802849.

[14] G. Srinivasan, Magnetoelectric composites, Annual Review of Materials Research. 40 (2010) 153–178. doi:10.1146/annurev-matsci-070909-104459.

[15] C.A.F. Vaz, J. Hoffman, C.H. Ahn, R. Ramesh, Magnetoelectric coupling effects in multiferroic complex oxide composite structures, Advanced Materials. 22 (2010) 2900–2918. doi:10.1002/adma.200904326.

[16] R.A. Islam, S. Priya, Effect of piezoelectric grain size on magnetoelectric coefficient of Pb(Zr0.52Ti0.48)O3–Ni0.8Zn0.2Fe2O4 particulate composites, J Mater Sci. 43 (2008) 3560–3568. doi:10.1007/s10853-008-2562-9.

[17] Z. Fang, S.G. Lu, F. Li, S. Datta, Q.M. Zhang, M. El Tahchi, Enhancing the magnetoelectric response of Metglas/polyvinylidene fluoride laminates by exploiting the flux concentration effect, Appl. Phys. Lett. 95 (2009) 112903. doi:10.1063/1.3231614.

[18] M.M. Vopson, Fundamentals of Multiferroic Materials and Their Possible Applications, Critical Reviews in Solid State and Materials Sciences. 40 (2015) 223–250. doi:10.1080/10408436.2014.992584.

[19] D. Erdem, N.S. Bingham, F.J. Heiligtag, N. Pilet, P. Warnicke, C.A.F. Vaz, Y. Shi, M. Buzzi, J.L.M. Rupp, L.J. Heyderman, M. Niederberger, Nanoparticle-Based Magnetoelectric $BaTiO_3$ –$CoFe_2O_4$ Thin Film Heterostructures for Voltage Control of Magnetism, ACS Nano. 10 (2016) 9840–9851. doi:10.1021/acsnano.6b05469.

[20] M. Liu, Z. Zhou, T. Nan, B.M. Howe, G.J. Brown, N.X. Sun, Voltage tuning of ferromagnetic resonance with bistable magnetization switching in energy-efficient magnetoelectric composites, Advanced Materials. 25 (2013) 1435–1439. doi:10.1002/adma.201203792.

[21] H. Wu, L. Li, L.-Z. Liang, S. Liang, Y.-Y. Zhu, X.-H. Zhu, Recent progress on the structural characterizations of domain structures in ferroic and multiferroic perovskite oxides: A review, Journal of the European Ceramic Society. 35 (2015) 411–441. doi:10.1016/j.jeurceramsoc.2014.09.037.

[22] M.S. Mirshekarloo, K. Yao, T. Sritharan, Ferroelastic strain induced antiferroelectric-ferroelectric phase transformation in multilayer thin film structures, Advanced Functional Materials. 22 (2012) 4159–4164. doi:10.1002/adfm.201200832.

[23] S. Lepadatu, M. Vopson, S. Lepadatu, M.M. Vopson, Heat-assisted multiferroic solid-state memory, Materials. 10 (2017) 991. doi:10.3390/ma10090991.

[24] X. Hao, J. Zhai, L.B. Kong, Z. Xu, A comprehensive review on the progress of lead zirconate-based antiferroelectric materials, Progress in Materials Science. 63 (2014) 1–57. doi:10.1016/j.pmatsci.2014.01.002.

[25] Z. Zhou, Q. Yang, M. Liu, Z. Zhang, X. Zhang, D. Sun, T. Nan, N. Sun, X. Chen, Antiferroelectric materials, applications and recent progress on multiferroic heterostructures, SPIN. 05 (2015) 1530001. doi:10.1142/S2010324715300017.

[26] Z. Zhou, X.Y. Zhang, T.F. Xie, T.X. Nan, Y. Gao, X. Yang, X.J. Wang, X.Y. He, P.S. Qiu, N.X. Sun, D.Z. Sun, Strong non-volatile voltage control of magnetism in magnetic/antiferroelectric magnetoelectric heterostructures, Applied Physics Letters. 104 (2014) 012905. doi:10.1063/1.4861462.

[27] J.-P. Zhou, X.-Z. Chen, L. Lv, C. Liu, P. Liu, Magnetoelectric coupling in antiferroelectric and magnetic laminate composites, Applied Physics A. 104 (2011) 461–464. doi:10.1007/s00339-011-6261-z.

[28] V.M. Petrov, M.I. Bichurin, G. Srinivasan, J. Zhai, D. Viehland, Dispersion characteristics for low-frequency magnetoelectric coefficients in bulk ferrite-piezoelectric composites, Solid State Communications. 142 (2007) 515–518. doi:10.1016/j.ssc.2007.03.043.

[29] F. Bai, H. Zhang, J. Li, D. Viehland, Magnetic and magnetoelectric properties of as-deposited and annealed BaTiO3–CoFe2O4 nanocomposite thin films, Journal of Physics D: Applied Physics. 43 (2010) 285002. doi:10.1088/0022-3727/43/28/285002.

[30] Y. Zhang, C. Deng, J. Ma, Y. Lin, C.-W. Nan, Enhancement in magnetoelectric response in CoFe2O4–BaTiO3 heterostructure, Applied Physics Letters. 92 (2008) 062911. doi:10.1063/1.2841048.

[31] M. Li, Z. Zhou, M. Liu, J. Lou, D.E. Oates, G.F. Dionne, M.L. Wang, N.X. Sun, Novel NiZnAl-ferrites and strong magnetoelectric coupling in NiZnAl-

ferrite/PZT multiferroic heterostructures, Journal of Physics D: Applied Physics. 46 (2013) 275001. doi:10.1088/0022-3727/46/27/275001.

[32] Y.P. Yao, Y. Hou, S.N. Dong, X.G. Li, Giant magnetodielectric effect in Terfenol-D/PZT magnetoelectric laminate composite, Journal of Applied Physics. 110 (2011) 014508. doi:10.1063/1.3603042.

[33] Y. Shen, J. Gao, Y. Wang, J. Li, D. Viehland, High non-linear magnetoelectric coefficient in Metglas/PMN-PT laminate composites under zero direct current magnetic bias, Journal of Applied Physics. 115 (2014) 094102. doi:10.1063/1.4867516.

[34] J. More-Chevalier, A. Ferri, C. Cibert, G. Poullain, R. Desfeux, R. Bouregba, Reversible control of magnetic domains in a Tb0.3Dy0.7Fe2/Pt/PbZr0.56Ti0.44O3 thin film heterostructure deposited on Pt/TiO2/SiO2/Si substrate, Journal of Applied Physics. 115 (2014) 214102. doi:10.1063/1.4880736.

[35] Y. Dusch, N. Tiercelin, A. Klimov, S. Giordano, V. Preobrazhensky, P. Pernod, Stress-mediated magnetoelectric memory effect with uni-axial TbCo2/FeCo multilayer on 011-cut PMN-PT ferroelectric relaxor, Journal of Applied Physics. 113 (2013) 17C719. doi:10.1063/1.4795440.

[36] J.G. Wan, J.-M. Liu, G.H. Wang, C.W. Nan, Electric-field-induced magnetization in Pb(Zr,Ti)O3/Terfenol-D composite structures, Applied Physics Letters. 88 (2006) 182502. doi:10.1063/1.2199967.

[37] C. Wang, X. Fang, A. Zhang, M. Zeng, Z. Fan, D. Chen, X. Gao, X. Lu, Coupling of ferroelastic strain and ferroelectric phase transition in NiMnGa/Pb0.97La0.02(Zr0.95Ti0.05)O3 bilayered films, Ceramics International. 44 (2018) 17199–17203. doi:10.1016/j.ceramint.2018.06.176.

[38] N. Tiercelin, V. Preobrazhensky, P. Pernod, A. Ostaschenko, Enhanced magnetoelectric effect in nanostructured magnetostrictive thin film resonant actuator with field induced spin reorientation transition, Applied Physics Letters. 92 (2008) 062904. doi:10.1063/1.2841656.

[39] A. Klimov, N. Tiercelin, Y. Dusch, S. Giordano, T. Mathurin, P. Pernod, V. Preobrazhensky, A. Churbanov, S. Nikitov, Magnetoelectric write and read operations in a stress-mediated multiferroic memory cell, Applied Physics Letters. 110 (2017) 222401. doi:10.1063/1.4983717.

[40] G. Li, Y. Liu, Stress-induced change of magnetization in a Ni–Mn–Ga single crystal under magnetomechanical training, Applied Physics Letters. 88 (2006) 232504. doi:10.1063/1.2210793.

[41] K. Aizu, Possible species of ferromagnetic, ferroelectric, and ferroelastic crystals, Physical Review B. 2 (1970) 754–772. doi:10.1103/PhysRevB.2.754.

[42] H. Schmid, Some symmetry aspects of ferroics and single phase multiferroics*, Journal of Physics: Condensed Matter. 20 (2008) 434201. doi:10.1088/0953-8984/20/43/434201.

[43] J. Valasek, Piezo-electric and allied phenomena in rochelle salt, Phys. Rev. 17 (1921) 475–481. doi:10.1103/PhysRev.17.475.

[44] C. Kittel, Theory of antiferroelectric crystals, Physical Review. 82 (1951) 729.

[45] G.H. Haertling, Ferroelectric ceramics: history and technology, Journal of the American Ceramic Society. 82 (1999) 797–818. doi:10.1111/j.1151-2916.1999.tb01840.x.

[46] B. Xu, Y. Ye, L.E. Cross, Dielectric properties and field-induced phase switching of lead zirconate titanate stannate antiferroelectric thick films on silicon substrates, Journal of Applied Physics. 87 (2000) 2507–2515. doi:10.1063/1.372211.

[47] Y. Tian, L. Jin, Y. Feng, Y. Zhuang, Z. Xu, X. Wei, Progress of antiferroelectric pervoskite oxides, (2017). doi:10.13725/j.cnki.pip.2017.05.001.

[48] Y. Zhao, X. Hao, Q. Zhang, Energy-Storage Properties and Electrocaloric Effect of Pb(1–3x/2)LaxZr0.85Ti0.15O3 Antiferroelectric Thick Films, ACS Appl. Mater. Interfaces. 6 (2014) 11633–11639. doi:10.1021/am502415z.

[49] C.W. Ahn, G. Amarsanaa, S.S. Won, S.A. Chae, D.S. Lee, I.W. Kim, Antiferroelectric Thin-Film Capacitors with High Energy-Storage Densities, Low Energy Losses, and Fast Discharge Times, ACS Appl. Mater. Interfaces. 7 (2015) 26381–26386. doi:10.1021/acsami.5b08786.

[50] J. Li, S. Tan, S. Ding, H. Li, L. Yang, Z. Zhang, High-field antiferroelectric behaviour and minimized energy loss in poly(vinylidene-co-trifluoroethylene)-graft-poly(ethyl methacrylate) for energy storage application, J. Mater. Chem. 22 (2012) 23468–23476. doi:10.1039/C2JM35532A.

[51] A. Chauhan, S. Patel, R. Vaish, C.R. Bowen, Anti-Ferroelectric Ceramics for High Energy Density Capacitors, Materials. 8 (2015) 8009–8031. doi:10.3390/ma8125439.

[52] B.D. Cullity, C.D. Graham, Introduction to magnetic materials, John Wiley & Sons, 2011.

[53] N.A. Spaldin, Magnetic materials: fundamentals and applications, Cambridge University Press, 2010.

[54] A.H. Morrish, The physical principles of magnetism, 2001. http://adsabs.harvard.edu/abs/2001ppm..book.....M (accessed June 18, 2019).

[55] A. Hubert, R. Schäfer, Magnetic domains: the analysis of magnetic microstructures, Springer Science & Business Media, 2008.

[56] H. Palneedi, V. Annapureddy, S. Priya, J. Ryu, Status and perspectives of multiferroic magnetoelectric composite materials and applications, Actuators. 5 (2016) 9. doi:10.3390/act5010009.

[57] N.A. Hill, Why are there so few magnetic ferroelectrics?, The Journal of Physical Chemistry B. 104 (2000) 6694–6709. doi:10.1021/jp000114x.

[58] D.N. Astrov, The magnetoelectric effect in antiferromagnetics, Sov. Phys. JETP. 11 (1960) 708–709.

[59] V.J. Folen, G.T. Rado, E.W. Stalder, Anisotropy of the magnetoelectric effect in Cr2O3, Physical Review Letters. 6 (1961) 607–608. doi:10.1103/PhysRevLett.6.607.

[60] T. Zhao, A. Scholl, F. Zavaliche, K. Lee, M. Barry, A. Doran, M.P. Cruz, Y.H. Chu, C. Ederer, N.A. Spaldin, R.R. Das, D.M. Kim, S.H. Baek, C.B. Eom, R. Ramesh, Electrical control of antiferromagnetic domains in multiferroic $BiFeO_3$ films at room temperature, Nature Materials. 5 (2006) 823–829. doi:10.1038/nmat1731.

[61] C.-W. Nan, M.I. Bichurin, S. Dong, D. Viehland, G. Srinivasan, Multiferroic magnetoelectric composites: Historical perspective, status, and future directions, Journal of Applied Physics. 103 (2008) 031101. doi:10.1063/1.2836410.

[62] Van Suchtelen J, Product properties: A new application of composite materials, Philips Research Reports. 27 (1972) 28–37.

[63] R.S. Devan, S.A. Lokare, D.R. Patil, S.S. Chougule, Y.D. Kolekar, B.K. Chougule, Electrical conduction and magnetoelectric effect of (x) BaTiO3 + (1−x) Ni0.92Co0.03Cu0.05Fe2O4 composites in ferroelectric rich region, Journal of Physics and Chemistry of Solids. 67 (2006) 1524–1530. doi:10.1016/j.jpcs.2006.02.005.

[64] J. Zhou, H. He, Z. Shi, G. Liu, C.-W. Nan, Dielectric, magnetic, and magnetoelectric properties of laminated PbZr0.52Ti0.48O3/CoFe2O4 composite ceramics, Journal of Applied Physics. 100 (2006) 094106. doi:10.1063/1.2358191.

[65] R.S. Devan, S.B. Deshpande, B.K. Chougule, Ferroelectric and ferromagnetic properties of (x)BaTiO3 -(1-x)Ni0.94Co0.01Cu0.05Fe2O4 composite, Journal of Physics D: Applied Physics. 40 (2007) 1864–1868. doi:10.1088/0022-3727/40/7/004.

[66] P. Li, Y. Wen, L. Bian, Enhanced magnetoelectric effects in composite of piezoelectric ceramics, rare-earth iron alloys, and ultrasonic horn, Applied Physics Letters. 90 (2007) 022503. doi:10.1063/1.2431469.

[67] F. Zavaliche, H. Zheng, L. Mohaddes-Ardabili, S.Y. Yang, Q. Zhan, P. Shafer, E. Reilly, R. Chopdekar, Y. Jia, P. Wright, D.G. Schlom, Y. Suzuki, R. Ramesh, Electric field-induced magnetization switching in epitaxial columnar nanostructures, Nano Letters. 5 (2005) 1793–1796. doi:10.1021/nl051406i.

[68] N. Lei, T. Devolder, G. Agnus, P. Aubert, L. Daniel, J.-V. Kim, W. Zhao, T. Trypiniotis, R.P. Cowburn, C. Chappert, D. Ravelosona, P. Lecoeur, Strain-controlled magnetic domain wall propagation in hybrid piezoelectric/ferromagnetic structures, Nature Communications. 4 (2013) 1378. doi:10.1038/ncomms2386.

[69] N. Lei, T. Devolder, G. Agnus, P. Aubert, L. Daniel, J.-V. Kim, W. Zhao, C. Chappert, D. Ravelosona, P. Lecoeur, Electric field control of domain wall logic in piezoelec-tric/ferromagnetic nanodevices, ArXiv:1201.4939 [Cond-Mat]. (2012). http://arxiv.org/abs/1201.4939 (accessed July 1, 2019).

[70] R.E. Newnham, D.P. Skinner, L.E. Cross, Connectivity and piezoelectric-pyroelectric composites, Materials Research Bulletin. 13 (1978) 525–536. doi:10.1016/0025-5408(78)90161-7.

[71] H.J.A. Molegraaf, J. Hoffman, C.A.F. Vaz, S. Gariglio, D. van der Marel, C.H. Ahn, J.-M. Triscone, Magnetoelectric effects in complex oxides with competing ground states, Advanced Materials. 21 (2009) 3470–3474. doi:10.1002/adma.200900278.

[72] C.-G. Duan, J.P. Velev, R.F. Sabirianov, Z. Zhu, J. Chu, S.S. Jaswal, E.Y. Tsymbal, Surface magnetoelectric effect in ferromagnetic metal films, Physical Review Letters. 101 (2008) 137201. doi:10.1103/PhysRevLett.101.137201.

[73] V. Garcia, M. Bibes, L. Bocher, S. Valencia, F. Kronast, A. Crassous, X. Moya, S. Enouz-Vedrenne, A. Gloter, D. Imhoff, C. Deranlot, N.D. Mathur, S. Fusil, K. Bouzehouane, A. Barthélémy, Ferroelectric control of spin polarization, Science. 327 (2010) 1106–1110. doi:10.1126/science.1184028.

[74] Y.-H. Chu, L.W. Martin, M.B. Holcomb, M. Gajek, S.-J. Han, Q. He, N. Balke, C.-H. Yang, D. Lee, W. Hu, Q. Zhan, P.-L. Yang, A. Fraile-Rodríguez, A. Scholl, S.X. Wang, R. Ramesh, Electric-field control of local ferromagnetism using a magnetoelectric multiferroic, Nature Materials. 7 (2008) 478–482. doi:10.1038/nmat2184.

[75] P. Yu, J.-S. Lee, S. Okamoto, M.D. Rossell, M. Huijben, C.-H. Yang, Q. He, J.X. Zhang, S.Y. Yang, M.J. Lee, Q.M. Ramasse, R. Erni, Y.-H. Chu, D.A. Arena, C.-C. Kao, L.W. Martin, R. Ramesh, Interface ferromagnetism and orbital reconstruction in BiFeO3-La0.7Sr0.3MnO3 heterostructures, Physical Review Letters. 105 (2010) 027201. doi:10.1103/PhysRevLett.105.027201.

[76] F. Zavaliche, T. Zhao, H. Zheng, F. Straub, M.P. Cruz, P.-L. Yang, D. Hao, R. Ramesh, Electrically assisted magnetic recording in multiferroic nanostructures, Nano Letters. 7 (2007) 1586–1590. doi:10.1021/nl070465o.

[77] J. More-Chevalier, U. Lüders, C. Cibert, A. Nosov, B. Domengès, R. Bouregba, G. Poullain, Magnetoelectric coupling in Pb(Zr,Ti)O3—Galfenol thin film heterostructures, Applied Physics Letters. 107 (2015) 252903. doi:10.1063/1.4938218.

[78] Y. Wang, J. Hu, Y. Lin, C.-W. Nan, Multiferroic magnetoelectric composite nanostructures, NPG Asia Materials. 2 (2010) 61–68. doi:10.1038/asiamat.2010.32.

[79] G. Liu, C.-W. Nan, N. Cai, Y. Lin, Dependence of giant magnetoelectric effect on interfacial bonding for multiferroic laminated composites of rare-earth-iron alloys and lead–zirconate–titanate, Journal of Applied Physics. 95 (2004) 2660–2664. doi:10.1063/1.1645648.

[80] C.-W. Nan, G. Liu, Y. Lin, Influence of interfacial bonding on giant magnetoelectric response of multiferroic laminated composites of Tb1−xDyxFe2 and PbZrxTi1−xO3, Applied Physics Letters. 83 (2003) 4366–4368. doi:10.1063/1.1630157.

[81] K. Zhou, Y.-D. Li, S.-L. Liu, Effects of the volume fraction of piezoelectric particles in the magneto-electro-elastic interfacial region on the fracture behavior of a laminate multiferroic plate, Physical Review Letters. 228 (2017) 1229–1248. doi:10.1007/s00707-016-1763-6.

[82] W.Q. Chen, Y.Y. Zhou, C.F. Lü, H.J. Ding, Bending of multiferroic laminated rectangular plates with imperfect interlaminar bonding, European Journal of Mechanics - A/Solids. 28 (2009) 720–727. doi:10.1016/j.euromechsol.2009.02.008.

[83] Y. Zhang, G. Liu, M. Li, J. Li, Y. Zhu, Enhanced converse magnetoelectric effect in Pb(Zr,Ti)O3-bimorph/Metglas laminated composite, Journal of Alloys and Compounds. 641 (2015) 188–191. doi:10.1016/j.jallcom.2015.04.036.

[84] M.M. Vopson, Y.K. Fetisov, G. Caruntu, G. Srinivasan, Measurement techniques of the magneto-electric coupling in multiferroics, Materials. 10 (2017) 963. doi:10.3390/ma10080963.

[85] J. Ma, J. Hu, Z. Li, C.-W. Nan, Recent progress in multiferroic magnetoelectric composites: from bulk to thin films, Advanced Materials. 23 (2011) 1062–1087. doi:10.1002/adma.201003636.

[86] M. Avellaneda, G. Harshé, Magnetoelectric effect in piezoelectric/magnetostrictive multilayer (2-2) composites, Journal of Intelligent Material Systems and Structures. 5 (1994) 501–513. doi:10.1177/1045389X9400500406.

[87] N.A. Spaldin, M. Fiebig, The renaissance of magnetoelectric multiferroics, Science. 309 (2005) 391–392. doi:10.1126/science.1113357.

[88] J. Zhai, Z. Xing, S. Dong, J. Li, D. Viehland, Magnetoelectric laminate composites: an overview, Journal of the American Ceramic Society. 91 (2008) 351–358. doi:10.1111/j.1551-2916.2008.02259.x.

[89] N.A. Spaldin, Multiferroics: Past, present, and future, MRS Bulletin. 42 (2017) 385–390. doi:10.1557/mrs.2017.86.

[90] G. Lawes, G. Srinivasan, Introduction to magnetoelectric coupling and multiferroic films, Journal of Physics D: Applied Physics. 44 (2011) 243001. doi:10.1088/0022-3727/44/24/243001.

[91] G. Sreenivasulu, H. Qu, G. Srinivasan, Multiferroic oxide composites: synthesis, characterisation and applications, Materials Science and Technology. 30 (2014) 1625–1632. doi:10.1179/1743284714Y.0000000537.

[92] G. Srinivasan, S. Priya, N. Sun, Composite magnetoelectrics: materials, structures, and applications, Elsevier, 2015.

[93] C. Cibert, J. Zhu, G. Poullain, R. Bouregba, J. More-Chevalier, A. Pautrat, Magnetoelectric coupling in Tb0.3Dy0.7Fe2/Pt/PbZr0.56Ti0.44O3 thin films deposited on Pt/TiO2/SiO2/Si substrate, Applied Physics Letters. 102 (2013) 022906. doi:10.1063/1.4775764.

[94] W. Pan, Q. Zhang, A. Bhalla, L.E. Cross, Field-forced antiferroelectric-to-ferroelectric switching in modified lead zirconate titanate stannate ceramics, J American Ceramic Society. 72 (1989) 571–578. doi:10.1111/j.1151-2916.1989.tb06177.x.

[95] M. Sharifzadeh Mirshekarloo, K. Yao, T. Sritharan, Large strain and high energy storage density in orthorhombic perovskite (Pb0.97La0.02)(Zr1−x−ySnxTiy)O3 antiferroelectric thin films, Applied Physics Letters. 97 (2010) 142902. doi:10.1063/1.3497193.

[96] W.Y. Pan, C.Q. Dam, Q.M. Zhang, L.E. Cross, Large displacement transducers based on electric field forced phase transitions in the tetragonal ($Pb_{0.97}La_{0.02}$)(Ti,Zr,Sn)O_3 family of ceramics, Journal of Applied Physics. 66 (1989) 6014–6023. doi:10.1063/1.343578.

[97] J.-M. Liu, K.F. Wang, Y. Wang, Q.C. Li, X.S. Gao, Magnetoelectric coupling in ferroelectromagnets with antiferroelectric and antiferromagnetic orders, Computational Materials Science. 30 (2004) 389–396. doi:10.1016/j.commatsci.2004.02.028.

[98] A. Sosa, N.S. Almodovar, J. Portelles, J. Heiras, J.M. Siqueiros, A study of the dielectric and magnetic properties of multiferroic materials using the Monte Carlo method, AIP Advances. 2 (2012) 012122. doi:10.1063/1.3681189.

[99] M.S. Mirshekarloo, N. Yakovlev, M.F. Wong, K. Yao, T. Sritharan, C.S. Bhatia, Magneto-optical Kerr effect investigation on magnetoelectric coupling in ferromagnetic/antiferroelectric multilayer thin film structures, Applied Physics Letters. 101 (2012) 172905. doi:10.1063/1.4764023.

[100] Harsha, K. S. Sree, Principles of vapor deposition of thin films, Elsevier, 2005.

[101] M. Ohring, Materials science of thin films, Elsevier, 2001.

[102] K. Kawabata, T. Tanaka, A. Kitabatake, K. Yamada, Y. Mikami, H. Kajioka, K. Toiyama, High rate sputtering for Ni films by an rf-dc coupled magnetron sputtering system with multipolar magnetic plasma confinement, Journal of Vacuum Science & Technology A. 19 (2001) 1438–1441. doi:10.1116/1.1351796.

[103] R. Bosco, J. van den Beucken, S. Leeuwenburgh, J. Jansen, Surface engineering for bone implants: a trend from passive to active surfaces, Coatings. 2 (2012) 95–119. doi:10.3390/coatings2030095.

[104] A. Niazi, P. Poddar, A.K. Rastogi, A precision, low-cost vibrating sample magnetometer, CURRENT SCIENCE. 79 (2000) 11.

[105] J. Hlinka, P. Ondrejkovic, M. Kempa, E. Borissenko, M. Krisch, X. Long, Z.-G. Ye, Soft antiferroelectric fluctuations in morphotropic PbZr1-xTixO3 single crystals as evidenced by inelastic x-ray scattering, Physical Review B. 83 (2011) 140101. doi:10.1103/PhysRevB.83.140101.

[106] Y. Li, W. Cao, Q. Li, Q. Yan, J. Gao, F. Zhuo, X. Xi, Y. Zhang, X. Chu, Electric field induced metastable ferroelectric phase and its behavior in (Pb, La)(Zr, Sn, Ti)O3 antiferroelectric single crystal near morphotropic phase boundary, Applied Physics Letters. 104 (2014) 052912. doi:10.1063/1.4864317.

[107] N. Luo, Y. Li, Z. Xia, Q. Li, Progress in lead-based ferroelectric and antiferroelectric single crystals: composition modification, crystal growth and properties, CrystEngComm. 14 (2012) 4547–4556. doi:10.1039/C2CE06430H.

[108] X. Yang, Y. Gao, J. Wu, Z. Zhou, S. Beguhn, T. Nan, N.X. Sun, Voltage tunable multiferroic phase shifter with YIG/PMN-PT heterostructure, IEEE Microwave and Wireless Components Letters. 24 (2014) 191–193. doi:10.1109/LMWC.2013.2292924.

[109] A.S. Tatarenko, V. Gheevarughese, G. Srinivasan, O.V. Antonenkov, M.I. Bichurin, Microwave magnetoelectric effects in ferrite—piezoelectric composites and dual electric and magnetic field tunable filters, Journal of Electroceramics. 24 (2010) 5–9. doi:10.1007/s10832-007-9382-1.

[110] C. Pettiford, S. Dasgupta, Jin Lou, S.D. Yoon, N.X. Sun, Bias field effects on microwave frequency behavior of PZT/YIG magnetoelectric bilayer, IEEE Transactions on Magnetics. 43 (2007) 3343–3345. doi:10.1109/TMAG.2007.893790.

[111] C. Thiele, K. Dörr, O. Bilani, J. Rödel, L. Schultz, Influence of strain on the magnetization and magnetoelectric effect in La0.7A0.3MnO3/PMN−PT (001) (A =Sr, Ca), Physical Review B. 75 (2007). doi:10.1103/PhysRevB.75.054408.

[112] V. Koval, Effect of PMN modification on structure and electrical response of xPMN–(1−x)PZT ceramic systems, Journal of the European Ceramic Society. 23 (2003) 1157–1166. doi:10.1016/S0955-2219(02)00281-9.

[113] R. Yimnirun, S. Ananta, E. Meechoowas, S. Wongsaenmai, Effects of uniaxial stress on dielectric properties lead magnesium niobate–lead zirconate titanate ceramics, Journal of Physics D: Applied Physics. 36 (2003) 1615–1619. doi:10.1088/0022-3727/36/13/329.

[114] H. Ouchi, K. Nagano, S. Hayakawa, Piezoelectric properties of Pb(Mg1/3Nb2/3)O3-PbTiO3-PbZrO3 solid solution ceramics, Journal of the American Ceramic Society. 48 (1965) 630–635. doi:10.1111/j.1151-2916.1965.tb14694.x.

[115] L. Wang, R. Liang, C. Mao, G. Du, G. Wang, X. Dong, Effect of PMN content on the phase structure and electrical properties of PMN–PZT ceramics, Ceramics International. 39 (2013) 8571–8574. doi:10.1016/j.ceramint.2013.04.023.

[116] L. Simon-Seveyrat, A. Hajjaji, Y. Emziane, B. Guiffard, D. Guyomar, Re-investigation of synthesis of BaTiO3 by conventional solid-state reaction and oxalate coprecipitation route for piezoelectric applications, Ceramics International. 33 (2007) 35–40. doi:10.1016/j.ceramint.2005.07.019.

[117] U. Anselmi-Tamburini, M.T. Buscaglia, M. Viviani, M. Bassoli, C. Bottino, V. Buscaglia, P. Nanni, Z.A. Munir, Solid-state synthesis and spark plasma sintering of submicron BaYxZr1−xO3−x/2 (x=0, 0.08 and 0.16) ceramics, Journal of the European Ceramic Society. 26 (2006) 2313–2318. doi:10.1016/j.jeurceramsoc.2005.04.022.

[118] C. Galassi, E. Roncari, C. Capiani, A. Costa, Influence of processing parameters on the properties of PZT materials, in: C. Galassi, M. Dinescu, K. Uchino, M. Sayer (Eds.), Piezoelectric Materials: Advances in Science, Technology and Applications, Springer Netherlands, Dordrecht, 2000: pp. 75–86. doi:10.1007/978-94-011-4094-2_9.

[119] T. Lu, A.J. Studer, L. Noren, W. Hu, D. Yu, B. McBride, Y. Feng, R.L. Withers, H. Chen, Z. Xu, Y. Liu, Electric-field-induced AFE-FE transitions and associated

strain/preferred orientation in antiferroelectric PLZST, Scientific Reports. 6 (2016) 23659. doi:10.1038/srep23659.

[120] C.T. Blue, J.C. Hicks, S. -E. Park, S. Yoshikawa, L.E. Cross, In situ x-ray diffraction study of the antiferroelectric–ferroelectric phase transition in PLSnZT, Applied Physics Letters. 68 (1996) 2942–2944. doi:10.1063/1.116362.

[121] M. Chen, X. Yao, L. Zhang, Preparation of (Pb, La)(Zr, Sn, Ti)O3 antiferroelectric ceramics using colloidal processing and the field induced strain properties, Journal of the European Ceramic Society. 21 (2001) 1159–1164. doi:10.1016/S0955-2219(00)00336-8.

[122] Y. Guo, Y. Liu, R.L. Withers, F. Brink, H. Chen, Large Electric Field-Induced Strain and Antiferroelectric Behavior in (1- x)(Na $_{0.5}$ Bi $_{0.5}$)TiO $_3$ - x BaTiO $_3$ Ceramics, Chemistry of Materials. 23 (2011) 219–228. doi:10.1021/cm102719k.

[123] F. Figueiras, E. Rauwel, V.S. Amaral, N. Vyshatko, A.L. Kholkin, C. Soyer, D. Remiens, V.V. Shvartsman, P. Borisov, W. Kleemann, Study of Ni2–Mn–Ga phase formation by magnetron sputtering film deposition at low temperature onto Si substrates and LaNiO3⁄Pb(Ti,Zr)O3 buffer, Journal of Vacuum Science & Technology A. 28 (2009) 6–10. doi:10.1116/1.3256200.

[124] S. Priya, R. Islam, S. Dong, D. Viehland, Recent advancements in magnetoelectric particulate and laminate composites, Journal of Electroceramics. 19 (2007) 149–166. doi:10.1007/s10832-007-9042-5.

[125] J.M. Rondinelli, M. Stengel, N.A. Spaldin, Carrier-mediated magnetoelectricity in complex oxide heterostructures, Nature Nanotechnology. 3 (2008) 46–50. doi:10.1038/nnano.2007.412.

[126] J. Lian, F. Ponchel, N. Tiercelin, Y. Chen, D. Rémiens, T. Lasri, G. Wang, P. Pernod, W. Zhang, X. Dong, Electric field tuning of magnetism in heterostructure of yttrium iron garnet film/lead magnesium niobate-lead zirconate titanate ceramic, Applied Physics Letters. 112 (2018) 162904. doi:10.1063/1.5023885.

[127] J. Lian, Y. Chen, Z. Liu, M. Zhu, G. Wang, W. Zhang, X. Dong, Annealing effects on the microstructure and magnetic properties of Y3Fe5O12 films deposited on Si/SiO2 substrates by RF magnetron sputtering, Ceramics International. 43 (2017) 7477–7481. doi:10.1016/j.ceramint.2017.03.023.

[128] Y.-M. Kang, S.-H. Wee, S.-I. Baik, S.-G. Min, S.-C. Yu, S.-H. Moon, Y.-W. Kim, S.-I. Yoo, Magnetic properties of YIG (Y3Fe5O12) thin films prepared by

the post annealing of amorphous films deposited by rf-magnetron sputtering, Journal of Applied Physics. 97 (2005) 10A319. doi:10.1063/1.1855460.

[129] A.I. Stognij, L.V. Lutsev, V.E. Bursian, N.N. Novitskii, Growth and spin-wave properties of thin Y3Fe5O12 films on Si substrates, Journal of Applied Physics. 118 (2015) 023905. doi:10.1063/1.4926475.

[130] J. Lian, F. Ponchel, N. Tiercelin, L. Han, Y. Chen, D. Rémiens, T. Lasri, G. Wang, P. Pernod, W. Zhang, X. Dong, Influence of the magnetic state on the voltage-controlled magnetoelectric effect in a multiferroic artificial heterostructure YIG/PMN-PZT, Journal of Applied Physics. 124 (2018) 064101. doi:10.1063/1.5037057.

[131] J.J. Yang, Y.G. Zhao, H.F. Tian, L.B. Luo, H.Y. Zhang, Y.J. He, H.S. Luo, Electric field manipulation of magnetization at room temperature in multiferroic CoFe2O4/Pb(Mg1/3Nb2/3)0.7Ti0.3O3 heterostructures, Applied Physics Letters. 94 (2009) 212504. doi:10.1063/1.3143622.

[132] S. Zhang, Y.G. Zhao, P.S. Li, J.J. Yang, S. Rizwan, J.X. Zhang, J. Seidel, T.L. Qu, Y.J. Yang, Z.L. Luo, Q. He, T. Zou, Q.P. Chen, J.W. Wang, L.F. Yang, Y. Sun, Y.Z. Wu, X. Xiao, X.F. Jin, J. Huang, C. Gao, X.F. Han, R. Ramesh, Electric-field control of nonvolatile magnetization in Co40Fe40B20/Pb(Mg1/3Nb2/3)0.7Ti0.3O3 structure at room temperature, Physical Review Letters. 108 (2012). doi:10.1103/PhysRevLett.108.137203.

[133] R.C. Hall, Magnetic anisotropy and magnetostriction of ordered and disordered cobalt-iron alloys, Journal of Applied Physics. 31 (1960) S157–S158. doi:10.1063/1.1984643.

[134] H.S. Jung, W.D. Doyle, J.E. Wittig, J.F. Al-Sharab, J. Bentley, Soft anisotropic high magnetization Cu/FeCo films, Applied Physics Letters. 81 (2002) 2415–2417. doi:10.1063/1.1510163.

[135] M.T. Rahman, Xiaoxi Liu, M. Matsumoto, A. Morisako, Compositional dependence of magnetoresistance in TbFeCo amorphous film, IEEE Trans. Magn. 41 (2005) 2568–2570. doi:10.1109/TMAG.2005.854664.

[136] N. Tiercelin, A. Talbi, V. Preobrazhensky, P. Pernod, V. Mortet, K. Haenen, A. Soltani, Magnetoelectric effect near spin reorientation transition in giant magnetostrictive-aluminum nitride thin film structure, Applied Physics Letters. 93 (2008) 162902. doi:10.1063/1.3001601.

[137] J.-M. Hu, T. Nan, N.X. Sun, L.-Q. Chen, Multiferroic magnetoelectric nanostructures for novel device applications, MRS Bulletin. 40 (2015) 728–735. doi:10.1557/mrs.2015.195.

[138] L.W. Martin, S.P. Crane, Y.-H. Chu, M.B. Holcomb, M. Gajek, M. Huijben, C.-H. Yang, N. Balke, R. Ramesh, Multiferroics and magnetoelectrics: thin films and nanostructures, Journal of Physics: Condensed Matter. 20 (2008) 434220. doi:10.1088/0953-8984/20/43/434220.

[139] N. Ortega, A. Kumar, J.F. Scott, R.S. Katiyar, Multifunctional magnetoelectric materials for device applications, Journal of Physics: Condensed Matter. 27 (2015) 504002. doi:10.1088/0953-8984/27/50/504002.

[140] C. Deng, Y. Zhang, J. Ma, Y. Lin, C.-W. Nan, Magnetoelectric effect in multiferroic heteroepitaxial BaTiO3–NiFe2O4 composite thin films, Acta Materialia. 56 (2008) 405–412. doi:10.1016/j.actamat.2007.10.004.

[141] J.G. Wan, X.W. Wang, Y.J. Wu, M. Zeng, Y. Wang, H. Jiang, W.Q. Zhou, G.H. Wang, J.-M. Liu, Magnetoelectric CoFe2O4–Pb(Zr,Ti)O3 composite thin films derived by a sol-gel process, Applied Physics Letters. 86 (2005) 122501. doi:10.1063/1.1889237.

[142] T. Li, G. Wang, K. Li, N. Sama, D. Remiens, X. Dong, Influence of LNO top electrodes on electrical properties of KNN/LNO thin films prepared by RF magnetron sputtering, Journal of the American Ceramic Society. 96 (2013) 787–790. doi:10.1111/jace.12047.

[143] N. Sama, R. Herdier, D. Jenkins, C. Soyer, D. Remiens, M. Detalle, R. Bouregba, On the influence of the top and bottom electrodes—A comparative study between Pt and LNO electrodes for PZT thin films, Journal of Crystal Growth. 310 (2008) 3299–3302. doi:10.1016/j.jcrysgro.2008.04.025.

[144] J. Ge, G. Pan, D. Remiens, Y. Chen, F. Cao, X. Dong, G. Wang, Effect of electrode materials on the scaling behavior of energy density in Pb(Zr0.96Ti0.03)Nb0.01O3 antiferroelectric films, Applied Physics Letters. 101 (2012) 112905. doi:10.1063/1.4752726.

[145] T. Li, G. Wang, D. Remiens, X. Dong, Characteristics of highly (001) oriented (K,Na)NbO3 films grown on LaNiO3 bottom electrodes by RF magnetron sputtering, Ceramics International. 39 (2013) 1359–1363. doi:10.1016/j.ceramint.2012.07.074.

[146] L. Yang, G. Wang, C. Mao, Y. Zhang, R. Liang, C. Soyer, D. Rémiens, X. Dong, Orientation control of LaNiO3 thin films by RF magnetron sputtering with different oxygen partial pressure, Journal of Crystal Growth. 311 (2009) 4241–4246. doi:10.1016/j.jcrysgro.2009.05.025.

[147] R. Herdier, D. Jenkins, D. Remiens, M. Dupont, D. Osmont, A silicon cantilever beam structure for the evaluation of d31, d33 and e31 piezoelectric coefficients of PZT thin films, in: 2007 Sixteenth IEEE International Symposium on the Applications of Ferroelectrics, 2007: pp. 725–727. doi:10.1109/ISAF.2007.4393383.

[148] N. Sama, C. Soyer, D. Remiens, C. Verrue, R. Bouregba, Bottom and top electrodes nature and PZT film thickness influence on electrical properties, Sensors and Actuators A: Physical. 158 (2010) 99–105. doi:10.1016/j.sna.2009.11.032.

[149] C. Mudivarthi, S.-M. Na, R. Schaefer, M. Laver, M. Wuttig, A.B. Flatau, Magnetic domain observations in Fe–Ga alloys, Journal of Magnetism and Magnetic Materials. 322 (2010) 2023–2026. doi:10.1016/j.jmmm.2010.01.027.

[150] J. Wang, M. Zhang, X. Gao, S. Zhou, R. Wang, The correlation between the first magnetocrystalline anisotropy constant K1 and the composition of giant magnetostrictive alloy Tb–Dy–Fe, Journal of Alloys and Compounds. 429 (2007) 56–59. doi:10.1016/j.jallcom.2006.04.012.

Publications

[1]. **Liuyang Han**, Freddy Ponchel, Nicolas Tiercelin, Denis Rémiens, Tuami Lasri, Philippe Pernod, Genshui Wang. Electric field tuning of magnetization in an antiferroelectric based heterostructure-example of NMG/PLZST/NMG[J]. ***Journal of the American Ceramic Society, 2019, 102: 3809–3813.***

[2]. **Liuyang Han**, Freddy Ponchel, Denis Rémiens, Tuami Lasri, Nicolas Tiercelin, Genshui Wang, Philippe Pernod. *E*-tunable magnetic susceptibility and reversible magnetization switching in YIG/Pt/PMN-PZT/Pt heterostructure by low electric and magnetic fields. ***Journal of Applied Physics, 2019,126(16):164104.***

[3]. **Liuyang Han**, Freddy Ponchel, Denis Rémiens, Tuami Lasri, Nicolas Tiercelin, Philippe Pernod, Genshui Wang. E-field control of magnetization and susceptibility of AFE-based YIG/PLZST heterostructure. ***Materials Research Bulletin, 2020, 122: 110666.***

[4]. **Liuyang Han**, Shaobo Guo, Shiguang Yan, Denis Rémiens, Genshui Wang, Xianlin Dong. Electrocaloric effect in $Pb_{0.3}Ca_xSr_{0.7-x}TiO_3$ ceramics near room temperature. ***Journal of Inorganic Materials*, *2019, 34 (9): 1011-1014.***

[5]. Jianyun Lian, Freddy Ponchel, Nicolas Tiercelin, **Liuyang Han**, Ying Chen, Denis Rémiens, Tuami Lasri, Genshui Wang, Philippe Pernod, Wenbin Zhang,Xianlin Dong. Influence of the magnetic state on the voltage-controlled magnetoelectric effect in a multiferroic artificial heterostructure YIG/PMN-PZT[J]. ***Journal of Applied Physics***, 2018, 124(6): 064101.

Conferences

1. International Symposium on Applications of Ferroelectrics (ISAF) 2019, Lausanne, Switzerland, 14-19 July, 2019, Oral presentation.

2. GDR Oxydes fonctionnels: des matériaux aux dispositifs (OXYFUN) Journées Nationales 2018, Piriac-Sur-Mer, 20-23 March, 2018, Oral presentation.